

**Alma Mater Studiorum – Università di Bologna**

**DOTTORATO DI RICERCA IN**

**Chimica**

**Chimica Industriale: Chimica e Tecnologia dei Prodotti  
e dei Materiali Polimerici e Ceramiche**

**Ciclo XXVIII**

**Settore Concorsuale di afferenza: 03/C2**

**Settore Scientifico disciplinare: CHIM/04**

**GEOPOLYMERS WITH TAILORED POROSITY**

**Presentata da: Elettra Papa**

**Coordinatore Dottorato**

**Prof. Aldo Roda**

**Relatore**

**Prof. Angelo Vaccari**

**Correlatori**

**Dr. Valentina Medri  
Dr. Elena Landi**

**Esame finale anno 2016**



## **Abstract**

Geopolymers are synthetic materials formed by alkali-activation of aluminosilicate particles. They have attracted increasing attention as sustainable materials, being obtained from different raw materials, including industrial by-products, and by production processes at low temperature. Thanks to the good properties showed by these materials (thermal stability, fire-resistance, etc.), and the intrinsic mesoporosity, geopolymers have been studied as new materials for applications in many industrially relevant fields. To achieve full advantage of their porous structure, it is necessary to control its formation. The geopolymer production process in aqueous medium allows to tailor the porosity from nanometric to millimetric range since water acts as pore former. Moreover, ultra-macroporosity may be induced in the materials exploiting different techniques, commonly used for the production of porous ceramics, determining the possibility to obtain materials with different architectures, pore size and shape, etc. Hierarchical pore systems, where the mesopores of the geopolymer skeletal materials are directly connected to macro- and finally to ultra-macropores, may be constructed in this way. The main goal of this research project was to investigate the use of different process techniques applied to geopolymer matrices to generate porous structures characterized by peculiar porosities able to determine specific properties and functionalize the materials. In detail, the porosity was induced by direct foaming or addition of lightweight aggregates. Furthermore, geopolymers with main unidirectional anisotropic macropores were produced, for the first time, using a freeze-casting technique. All the materials produced were deeply investigated to optimize the production processes and evaluate the final properties, many of which arising from the intrinsic and induced porosity generated, in order to address the materials for potential applications as, for example, thermal insulating panels or heat transfer devices.

## **Acknowledgements**

My acknowledgements go to many people from the Institute of Science and Technology for Ceramic Materials, ISTECCNR of Faenza RA (Italy), where I developed my research project, and the Department of Industrial Chemistry “Toso Montanari” of the ALMA MATER STUDIORUM - University of Bologna, who have devoted time and knowledge in this project. I am extremely fortunate and very grateful to have met so many wonderful people in the course of my studies who have helped me in different ways.

First and foremost, I would like to express my sincere gratitude to my supervisors Dr. Valentina Medri, Dr. Elena Landi and Prof. Angelo Vaccari, for their invaluable guidance and advice, remarkable encouragement and continuous support throughout my PhD project, and for their tireless efforts in reading and correcting my Thesis; without them the goal would not have been achieved.

I would also like to thank many other people who have generously contributed their time and resources to this project with theoretical discussions, measurements or other aspects of the project. I would like to thank, in no particular order, Dr. Annalisa Natali Murri, Andreana Piancastelli, Guia Guarini, Cesare Melandri, Claudio Capiati, Dr. Patricia Benito Martin and all the ISTECCNR Staff for assistance and for offering me a pleasant research environment to complete this research work.

I would also like to thank Riccardo, Federico, Giulio, Natalia and all my colleagues, for their friendship and support shown every day during my PhD.

I would like to acknowledge the EU Marco Polo grant for giving me the opportunity to spend 3-months at the “Laboratoire Science des Procédés Céramiques et de Traitements de Surface UMR-CNRS 7315” of the University of Limoges, under the estimated guidance of Prof. Sylvie Rossignol, that I would like to thank, together with all the SPCTS Staff, for the help and the kindness.

I would like to thank the evaluators of my Thesis Dr. Arnaud Poulesquen and Dr. Ana Fernández Jiménez for the efforts in reading and correcting my Thesis.

Thanks are also due to Prof. Sylvie Rossignol and Prof. Cristina Leonelli for the honor to have accepted to be members of the final evaluation committee, devoting time and efforts to allow to me to reach this key objective.

I'm also extremely grateful to my beloved family members and all my friends for their love and support and, in particular, I would like to thank my boyfriend Gabriele for his understanding and patience.

**Thank you all!!!**

## Publications

- E. Papa, V. Medri, P. Benito, A. Vaccari, S. Bugani, J. Jaroszewicz, E. Landi, Insights into the macroporosity of freeze-cast hierarchical geopolymers, *RSC Advances* 6 (2016) 24635-24644.
- V. Medri, E. Papa, M. Mazzocchi, L. Laghi, M. Morganti, J. Francisconi, E. Landi, Production and characterization of lightweight vermiculite/geopolymer-based panels, *Materials and Design* 85 (2015) 266-274.
- E. Papa, V. Medri, P. Benito, A. Vaccari, S. Bugani, J. Jaroszewicz, W. Swieszkowski, E. Landi, Synthesis of porous hierarchical geopolymer monoliths by ice-templating, *Microporous and Mesoporous Materials* 215 (2015) 206-214.
- Natali Murri, V. Medri, A. Ruffini, E. Papa, E. Landi, Study of the chemical activation of hydroxyapatite rich ashes as raw materials for geopolymers, *Ceramics International* 41(2015) 9734–9744.
- E. Papa, V. Medri, E. Landi, B. Ballarin, F. Miccio, Production and characterization of geopolymers based on mixed compositions of metakaolin and coal ashes, *Materials and Design* 56 (2014) 409-415.
- Natali Murri, E. Papa, V. Medri, E. Landi, Design of wool-geopolymer pots, Proceedings of 38<sup>th</sup> International conference and exposition on advanced ceramics & composites, *ICACC* 2014.
- F. Miccio, V. Medri, E. Papa, A. Natali Murri, E. Landi, Geopolymerization as effective measure for reducing risks during coal ashes handling, storage and disposal, *Chemical Engineering transactions*, 2014, vol. 36.
- V. Medri, E. Papa, E. Landi, Behaviour of alkali bonded silicon carbide foams in modified synthetic body fluid, *Materials Letter* 106 (2013) 377-380.
- V. Medri, E. Landi, E. Papa, J. Dedecek, P. Klein, P. Benito, A. Vaccari, Effect of metallic Si addition on polymerization degree of in situ foamed alkali- aluminosilicates, *Ceramic International* 39 (2013) 7657-7668.

- E. Landi, V. Medri, E. Papa, J. Dedeczek, P. Klein, P. Benito, A. Vaccari, Alkali-bonded ceramics with hierarchical tailored porosity, *Applied Clay Science*, 73 (2013) 56–64.

### **Submitted paper**

- M. Minelli, V. Medri, E. Papa, F. Miccio, E. Landi, F. Doghieri, Geopolymers as solid adsorbent for CO<sub>2</sub> capture, submitted to *Chemical Engineering Science*, January 2016.

### **Co-relator of master thesis**

- F. Servadei, Production of porous geopolymers by freeze-casting, Course of Chemistry and Technologies for the Environment and Materials, class L-27 Chemistry, University of Bologna, Faenza headquarters, March 2015.
- F. Valorosi, Production and characterization of geopolymers from combustion ashes, Course in Industrial Chemistry, class L-27 Chemical Sciences and Technologies, University of Bologna, July 2013.

### **Presentation at national and international conferences**

- E. Papa (presenting author: oral), V. Medri, P. Benito, A. Vaccari, E. Landi, Insights into freeze casting of geopolymers, XIX Congresso Nazionale Divisione di Chimica Industriale della Società Chimica Italiana, Salerno, 14-16 settembre 2015.
- E. Papa (presenting author: oral), V. Medri, P. Benito, A. Vaccari, E. Landi, Freeze casting of alkali bonded ceramics, 14th International Conference of the European Ceramic Society, 21-25 June, 2015, Toledo, Spain.
- E. Papa (presenting author: poster), V. Medri, P. Benito, A. Vaccari, E. Landi, “Hierarchical geopolymers by ice-templating”, Workshop - How to exploit the porosity of geopolymers?, 2<sup>nd</sup> October 2014, Faenza, Italy.
- V. Latini, A. Urbani, V. Medri, E. Landi, E. Papa (presenting author: poster), A. Natali Murri, “Realization and testing of a loop heat pipe evaporator”, Workshop - How to exploit the porosity of geopolymers?, 2<sup>nd</sup> October 2014, Faenza, Italy.

- E. Papa (presenting author: oral), E. Landi, P. Benito, A. Vaccari, V. Medri, “Tailoring of the porosity in geopolymers”, XXV Congresso Nazionale della Società Chimica Italiana, Arcavacata di Rende 7-12 settembre 2014.
- E. Papa (presenting author: invited oral), V. Medri, A. Vaccari, P. Benito, E. Landi, “Tailoring of the porosity in geopolymers”, 38<sup>th</sup> ICACC, Daytona Beach, Florida, 26-31 Gennaio 2014.
- A. Natali Murri, E. Papa (presenting author: poster), V. Medri, E. Landi, “Design of wool-geopolymer pots”, 38<sup>th</sup> ICACC, Daytona Beach, Florida, 26-31 Gennaio 2014.
- E. Landi, F. Valentini, E. Papa (presenting author: poster), V. Medri, “Exploiting Sr ion in the development of bioceramics”, 1<sup>st</sup> edition MiMe, 8-11 ottobre 2013, Faenza, Italy.
- E. Papa (presenting author: oral), E. Landi, P. Benito, A. Vaccari, V. Medri, “Porosity tailoring in synthetic alumino-silicate materials”, XVII National Congress of Catalysis GIC 2013 and XI National Congress of Zeolites Science and Technology, Riccione 15-18 settembre 2013.
- E. Papa (presenting author: oral), E. Landi, A. Vaccari, P. Benito, V. Medri, “In situ inorganic foaming of ceramics”, 13<sup>th</sup> Conference of the European Ceramic Society, ECERS XIII, Limoges, France, June 23-27, 2013.

## ***Table of contents***

Abstract .....	I
Acknowledgements.....	II
Publications.....	IV
<i>Table of contents</i> .....	VII
1. Introduction .....	1
1.1 Research objectives.....	1
1.2 Content of the thesis.....	2
2. Literature overview .....	5
2.1 Porous materials.....	5
2.2 Geopolymers .....	7
2.3 Geopolymer precursors .....	8
2.3.1 Alluminosilicate powders.....	9
2.3.2 Alkali activating solution .....	11
2.3.3 Fillers .....	12
2.4 Geopolymer synthesis.....	14
2.5 Geopolymer structure.....	16
2.6 Geopolymer microstructure and porosity .....	18
2.7 Processing techniques for macroporous geopolymers .....	21
2.7.1 Sacrificial template method .....	21
2.7.1.1 Freeze casting.....	25
2.7.2 Direct foaming method .....	27
2.7.3 Solid free-form fabrication.....	31
2.7.4 Addition of fillers to generate porosity .....	32
2.7.3.1 Inert fillers.....	33
2.7.3.2 Reactive fillers .....	33
References.....	34
3. Experimental procedures.....	45
3.1 General preparation of the geopolymer slurries.....	45
3.2 Characterization techniques .....	46
3.2.1 Viscosity measurement.....	46
3.2.2 Macrostructure characterization.....	46
3.2.3 Micro Computed Tomography ( $\mu$ -CT).....	46
3.2.4 Microstructure characterization .....	47

3.2.5 True density .....	47
3.2.6 Bulk density.....	47
3.2.7 Total porosity.....	47
3.2.8 Mercury Intrusion Porosimetry (MIP) .....	47
3.2.9 N <sub>2</sub> adsorption/desorption analysis .....	48
3.2.10 Specific surface area.....	48
3.2.11 Stability in water .....	48
3.2.12 Linear Shrinkage Measurement.....	48
3.2.13 Attenuated Total Reflection - Fourier Transform Infrared Spectroscopy (ATR-FTIR).....	49
3.2.14 X-Ray Diffraction (XRD) .....	49
3.2.15 X-Ray Fluorescence (XRF).....	49
3.2.16 Flexural strength.....	50
3.2.17 Compressive strength .....	50
3.2.18 Dilatometric analysis.....	50
3.2.19 Thermal conductivity .....	50
References .....	51
4. Ice-templating of geopolymers .....	54
4.1 Introduction .....	54
4.2 Samples preparation .....	57
4.3 Effect of water addition on slurry G13.....	58
4.3.1 Macro- and microstructures of the ice-templated G13 geopolymers .....	59
4.3.2 Intrinsic and induced porosity of the freeze-cast geopolymers .....	61
4.3.3 Chemical composition of the ice-templated samples (XRF analysis).....	64
4.4 Production and characterization of G13-50 monoliths.....	66
4.4.1 Analysis by $\mu$ -Computed Tomography of the G13-50 monolith.....	66
4.5 Effect of water addition and different maturation steps on slurry G23 .....	68
4.5.1 Macro-structure of the freeze-cast samples.....	69
4.5.2 Rheology of the starting slurries .....	71
4.5.3 Microstructure of the freeze-cast samples.....	73
4.5.4 Chemical composition (XRF analysis).....	76
4.5.5 Analysis of the porosity.....	77
4.5.5.1 Accessible porosity through Hg intrusion porosimetry and N <sub>2</sub> adsorption/desorption analysis .....	77
4.5.5.2 Lamellar macroporosity .....	81

4.5.6 $\mu$ -Computed Tomography of the G23 ice-templated monoliths .....	82
4.6 Scale-up on the freeze-cast G23-T2-50 sample preparation .....	85
4.8 Conclusions .....	87
References .....	89
5. Production of porous geopolymer wicks for a loop heat pipe (LHP) prototype	93
5.1 Introduction .....	93
5.1.1 LHP description .....	93
5.1.2 Aim of the work .....	94
5.2 Experimental procedure .....	95
5.2.1 Production of the primary wick .....	95
5.2.2 Production of secondary wick .....	96
5.2.3 Production of the LHP prototype .....	96
5.3 Optimization of the production process of the wicks .....	97
5.3.1 Primary wick .....	97
5.3.2 Secondary wick .....	98
5.4 Characterization .....	100
5.4.1 Rheology of the starting composite slurries .....	100
5.4.2 Macro and microstructural characterization of the wicks .....	101
5.4.3 Analysis of the porosity of the wicks .....	103
5.4.4 Thermal behavior of the wicks .....	105
5.5 LHP prototype .....	106
5.6 Conclusions .....	108
References .....	109
6. Addition of fillers to generate a macroporosity .....	112
6.1 Addition of inert filler: lightweight geopolymer-vermiculite composites. ....	112
6.1.1 Introduction .....	112
6.1.2 Experimental procedure .....	113
6.1.2.1 Production of the composites .....	113
6.1.2.2 Scale-up of the production process .....	115
6.1.3 Characterization of the composite panels .....	117
6.1.3.1 Macro and microstructural characterization .....	117
6.1.3.2 Stability in water .....	119
6.1.3.3 Porosity .....	120
6.1.3.4 Thermal properties .....	121
6.1.3.5 Mechanical properties .....	128

6.2 Addition of reactive filler: silica-fume based foams .....	132
6.2.1 Introduction .....	132
6.2.2 Experimental procedure .....	133
6.2.2.1 Foam preparation.....	133
6.2.2.2 Selection of the best foams.....	134
6.2.3 Characterization of the selected foams.....	136
6.2.3.1 Infrared spectroscopy (FTIR-ATR).....	136
6.2.3.2 Macro- and microstructures of the foams.....	140
6.2.3.3 Analysis of the porosity.....	143
6.2.3.4 Thermal conductivity .....	146
6.3 Conclusions .....	148
References .....	149
7. Conclusions .....	154

# 1. Introduction

## 1.1 Research objectives

Geopolymers are synthetic materials formed by alkali-activation of solid aluminosilicate particles. They have attracted attention as sustainable materials being obtained from different starting raw materials, including industrial by-products, and with production processes at low temperature. Currently, the research has been focused on the study of geopolymers as a possible replacement for Portland cement; however, thanks to the good properties showed by these materials (high compressive strength, acid resistance, thermal stability, fire-resistance, waste confinement properties of the matrix, etc.), geopolymers have been studied as potential new materials for applications in many industrially relevant fields.

Since porous materials are of special interest because of their structural and functional properties, the porosity of the geopolymers plays an important role. In order to take full advantage of the porous structure, it is necessary to control the pore morphology, feature size and the amount of porosity. Geopolymers are intrinsically mesoporous and the production process in aqueous medium allows to tailor the porosity from nanometric to millimetric range. The water content, present in the starting mixtures, affects the intrinsic mesoporosity of the geopolymer matrix, since water acts as pore former during the polycondensation stage. Moreover, ultra-macroporosity may be induced in the materials exploiting different techniques, commonly used for the production of porous ceramics. In the last decades several processing routes have been developed determining the possibility to obtain materials with different architectures, pore size distribution, interconnectivity, etc. Methods reported in literature for ceramics materials may be adapted for the production of geopolymers with some advantages. Porous ceramics are usually treated at high temperature to burnout the additives or templates and for the final consolidation (sintering), that confers the specific mechanical and functional properties, while geopolymers are consolidated by means of a chemical reaction occurring at low temperature.

It is important to highlight that, although the geopolymer skeletal material is originally mesoporous, a hierarchical pore system, in which mesopores are

directly connected to macro- and finally to ultra-macropores, may be constructed. The artificially addition of macroporosity to the geopolymer matrices enables the achievement of hierarchical porous structures, with a total porosity up to 90 %, with pore size dimensions from few tenth of nanometers to some millimeters.

The possibility to tailor the porosity of the geopolymers results useful to fulfil the requirements for many scientific and industrial applications (biomaterials, catalysis, filtration, thermal insulation, etc.). Therefore, the main theme of this research project was to applied different process techniques to geopolymer matrices in order to generate hierarchical porous structures characterized by different dimension, shape, distribution of the pores and to functionalize the materials. In detail, the porosity was induced by direct foaming or addition of lightweight aggregates. Furthermore, geopolymers with porous architectures with main unidirectional anisotropic macropores were produced, for the first time, using a freeze-casting technique, where ice crystals act as pore network templates. Differently from the literature, the process was applied to reactive geopolymer water-based sol-gel systems, without addition of any organic dispersant or binder. All the materials produced in the course of this research were deeply investigated to optimize the production processes and evaluate the final properties, many of which arising from the intrinsic and induced porosity generated, in order to address the materials for the potential applications.

## **1.2 Content of the thesis**

This Thesis is divided into seven chapters, that may be read and understood independently without reference to other sections with the exception of some experiment procedures and characterization methods commonly used.

Chapter 2 consists of a deep literature review on the fundamental chemistry and processes occurring during geopolymer synthesis and on the structural properties shown by geopolymers. Current fabrication methods, commonly used for the production of porous ceramics, are described and related examples of the techniques applied to the geopolymers reported.

Chapter 3 reports the general raw materials and the production process for the synthesis of the geopolymer slurries, with the description of the measurements and analysis methods for the investigation of the materials.

The following chapters are addressed to the production, process optimization and characterization of porous geopolymers obtained through the exploitation of different techniques. Chapter 4 deals with the ice-templating of geopolymer systems to obtain unidirectional lamellar porosity. Geopolymerization was triggered by maturation steps to combine the simultaneous formation of the intrinsic mesoporosity of the material and the lamellar macroporosity obtained by the process. Multiple parameters, that can be interdependent, as starting formulations, maturation treatments and mold shape, dictated the ordering and the structural properties of the lamellar monoliths obtained. Therefore, a systematic study on the effects of these parameters on the mesoporosity and macroporosity of the final ice-templated samples was done.

In the chapter 5 the geopolymer porosity was tailored to fulfil the requirements for the production of a loop heat pipe (LHP) evaporator prototype, consisting in a metallic container with two internal geopolymer capillary structures (primary and secondary wick), coaxially inserted one inside the other. Geopolymer porous wicks were studied as an innovative solution, in order to decrease the cost and facilitate the preparation of the final LHP device. The tailoring of the porosity was obtained combining an *in situ* foaming technique with the addition of filler.

The good thermal exchange performances, obtained in preliminary tests, revealed as this innovative use of geopolymer wicks, with tailored porosity, was a promising technology for the production of LHP. The work was developed in the frame of the Italian Project PON01\_00375 “PANDION- Study of innovative functional Space-subsystems” and in collaboration with SAB Aerospace S.r.l. laboratories.

In the chapter 6 the use of fillers in the geopolymer composition was investigated to give specific properties and increase the porosity of the material. Exfoliated vermiculite, used as inert lightweight aggregate, resulted ideal for the production of lightweight composites with good thermal and fire-resistance properties.

Big panels were produced through a scale-up process and the good thermal and mechanical properties, obtained from the analysis, suggested a possible utilization as pre-cast high-temperature insulating panels, suitable to be mechanically anchored to a load-bearing structure.

The work was developed in the frame of the Project “MATEC — New materials

and new technologies for internal combustion co-generator prototype”, funded by the Italian Ministry of Economic Development (MISE, Roma I).

The use of a reactive filler, such as silica fume that contains silicon impurities able to generate H<sub>2</sub> that cause the foaming of the geopolymer slurry, resulted a good method to produce lightweight, low-cost material for possible insulating applications. The work was developed during a 3-months stage at the “Laboratoire Science des Procédés Céramiques et de Traitements de Surface UMR-CNRS 7315” of the University of Limoges (F), thanks to a Marco Polo grant.

Finally, the conclusions of this Thesis and recommendations are covered in chapter 7. I hope that the readers may appreciate this PhD Thesis; their opinion will be the best reward to the time spent and the efforts done.

## **2. Literature overview**

### **2.1 Porous materials**

Porous materials widely exist around us and can be applied in different fields as energy management, vibration suppression, heat insulation, sound absorption and fluid filtration. These materials are used mainly functionally than structurally and many integrative applications were developed to take full advantage from them [1]. Porous materials are made of a continuously solid phase that forms the basic porous frame and a fluid phase, gaseous or liquid, that forms the pores in the solid. Commonly, porous materials must have two essential characteristics: contain a lot of pores and have pores designed specifically to achieve the performances required by the material. Therefore, the porous phase of the materials may be thought as a functional phase that supplies an optimizing action for the performance of the material.

Making a dense material porous endows it with brand-new and useful properties suitable for many applications.

There are different types of porous materials, but all of them have some common characteristics that include low relative density, large specific surface area, high specific strength, small thermal conductivity, permeability and good energy absorption, compared to the dense version of the same materials [1]. Low-density porous materials may be used to design lightweight rigid components and large portable structural frames. Low-thermal-conductivity products can be applied to simple and convenient forms of heat insulation. Low rigidity foamed bodies may be used as perfect material for mechanical damping. Furthermore, the large compressive strain of these materials make them quite attractive for energy absorption applications [1].

These properties can be tailored in order to satisfy the final application of the material by controlling the composition and the microstructure of the porous materials. For every mentioned application is necessary to control the amount, dimension and distribution of the pores (shape, morphology, orientation, surface properties, open or closed porosity), that are highly influenced by the processing routes applied to obtain the final porous materials. Indeed, as reported in Table 2.1, there is a relationship between the porosity and the properties of the final

materials [2].

**Table 2.1** Influence of porosity on the properties [2].

Porosity dependence		Examples of properties
No dependence on porosity		Lattice parameter, unit cell volume, thermal expansion, heat capacity per unit weight, density
Dependence only on the amount of porosity		Apparent density, dielectric constant, heat capacity per unit volume
Dependence both the amount and character of porosity	Flux or stress dominant in the solid phase	Mechanical properties, electrical and thermal conductivity at low to moderate temperature and porosity
	All flux in the pore phase and filtration	Surface area and tortuosity, e.g. for catalysis
	Flux in both pore and solid phase	Thermal conductivity, with larger and more open pores at higher temperature

The complex connection between the function expression and pore properties (pore size, porosity, pore shape) does necessary to have a method to carefully catalogue the pores from the standpoint of material design. There is no unanimous classification criterion for porous materials, since each sector of application has its own classification principles and norms. However, pores can be classified using the IUPAC (Union of Pure and Applied Chemistry) method, which is internationally recognized and based on the results of nitrogen adsorption experiments [3].

In Table 2.2 the relative pore size is reported to define the pore classification. Furthermore, the classification is based on the function expression, the phenomena that occur in the pores and considering the synthesis methods to obtain the porous materials [4]. Porous ceramics, for example, have a pore size that mostly ranges between the nanometer and millimeter levels, the porosity usually spans from 20 % to 95 %, and the serving temperature varies from room temperature to 1600 °C [5]. Because of their unique structures and characteristics, such as high temperature and environmental stability, low thermal conductivity, low thermal mass, low dielectric constant, low density, high thermal shock resistance, high wear resistance, high specific strength, high permeability for gases and liquids, they result indispensable for a wide range of engineering applications as, for example, heat insulation of buildings and aircraft, filtration of liquids, hot gases, liquid metals and alloys, catalyst carriers in various chemical

processes, membranes for separation and purification of gas and liquids, artificial scaffolds for osseous tissue regeneration, etc. [6].

**Table 2.2** Classification of the porous materials [4].

Category		Pore radius range	Origin of pore	State of atoms or molecules in pore	Characterization methods
Atom and molecule pore	Micropore	< 2 nm	Space among atoms or ions, crystal lattice, trace of solvent molecules after drying	Microporefilling, atom, ion, molecule	Gas adsorption, TEM, XRD
Aggregate molecules pore	Mesopore I	2 – 10 nm	Micelle or liquid crystal templating	Intermediate state of microporefilling and condensation, molecules interact with pore wall	Gas adsorption, TEM, XRD
Liquid phase pore	Mesopore II	2 – 50 nm	Phase separation, space among particles	Capillary condensation, liquid phase	Gas adsorption, TEM, SEM
Spatial pore	Macropore	> 50 nm	Bubble, cavity, space among particles, particle templating	The same on a flat surface, pore is just a space	Porosimetry, SEM

Geopolymers are porous materials showing a lot of properties suitable to be used in different applications. They are intrinsically nanoporous materials, moreover their macroporosity may be tailored through the use of different techniques able to artificially create porosity to functionalize the final material.

For example, the geopolymer thermal stability combined with a sufficiently porous structure allows to use them for insulation [7], as catalyst support and filters [8], for the production of panels for acoustic insulation [9] and as autoclaved aerated concretes [10-11].

In the following chapters the geopolymer nature and the processing techniques applicable to obtain macroporous materials are thoroughly described.

## 2.2 Geopolymers

The term ‘geopolymer’ was first applied by Davidovits, in the year 1979 [12], to X-ray amorphous aluminosilicate binders formed through an hydrothermal synthesis between aluminosilicates and a concentrated alkaline or alkaline silicate solutions. Davidovits coined the word ‘geopolymer’ in order to emphasize the main aspects of these new materials: ‘geo’ referring to the inorganic nature and the mimicking of natural materials, and ‘polymer’ to infer a structure analogous to that of organic polymers. The term ‘geopolymer’ is the generally accepted name

for this type of materials even if researchers have been published using different terminology including ‘low-temperature aluminosilicate glass’ [13], ‘alkali-activated cement’ [14] and ‘hydroceramic’ [15]. Geopolymers are also considered as alkali bonded ceramics and belong to the class of chemically bonded materials produced at low temperature using chemical reactions [16].

The final structure is formed mainly by Si-O-Al and Si-O-Si tetrahedral bonds arranged in a solid amorphous or semi-crystalline network. Unreacted materials and small amounts of other newly formed phases are typically present in the material, trapped in the network. Geopolymers are principally known for their high compressive strength, acid resistance and the ability to withstand elevated temperatures and fire. The inorganic framework have excellent thermal stability [17] and waste confinement properties [18].

Geopolymers are often referred as “green cements” because of the use of industrial waste products as fly ashes and slags, making them an environmentally friendly replacement for “Ordinary Portland Cement” (OPC). Furthermore, the CO<sub>2</sub> emission for the production of these materials are 10 times lower than for OPC, representing significant environmental benefits [19]. They may be cost-competitive with OPC and exhibit superior chemical and mechanical properties [20].

However, geopolymers have a wide range of potential applications including: fire resistant materials, decorative stone artifacts, thermal insulating, low energy ceramic tiles, refractory items, thermal shock refractories, foundry applications, composites for infrastructure repair and strengthening, high-tech composites for aircraft interior and automobile, high-tech resin systems, filters, catalyst supports, etc. [21].

### **2.3 Geopolymer precursors**

Geopolymer synthesis typically requires three fundamental starting materials, carefully selected in view of the final applications:

- The aluminosilicate starting powder, reactive in the geopolymerization process
- The activating alkali aqueous solution
- Fillers

### 2.3.1 Alluminosilicate powders

Theoretically, any aluminosilicate material may undergo geopolymerization under certain conditions. The presence of large amounts of silicon and aluminium in minerals, clays, industrial wastes and ashes makes these materials common for use as starting powders in geopolymerization. Literature reports examples of the formation of geopolymers from natural minerals [22-24], calcined clays [25-26], industrial by-products [27-29] or a combination of them [30-34].

The leaching ability of Al and Si, in the starting raw powders, follows the descending order: Metakaolin > Zeolite > Slag > Fly Ash > Pozzolana > Kaolin [35]. Calcinated raw materials are more reactive in the geopolymerization process because of the presence of amorphous phase formed after the thermal activation and easily leached during the alkaline hydrolysis [30].

The selection of the starting raw powders is done in view of the final application of the geopolymer material. The Si/Al molar ratio and the consequent geopolymer final structure change in function of the powder used. In particular, depending on the raw powder used, Si/Al ratio may be in the range [21]:

- $1 < \text{Si/Al} < 3$  for alluminosilicate powders rich in aluminum as metakaolins and fly ash.
- $1 < \text{Si/Al} < 5$  for rock forming minerals (feldspar, mica, kaolin, smectite, chlorite,..) activated in highly alkaline conditions because poorly reactive.
- $5 < \text{Si/Al} < 25$  for powders rich in silicon as rice husk and fumed silica.

The possible applications, as a function of the Si/Al molar ratio, are reported in figure 2.1. The geopolymer network may be bi- or tri-dimensional as a function of the Si and Al content.

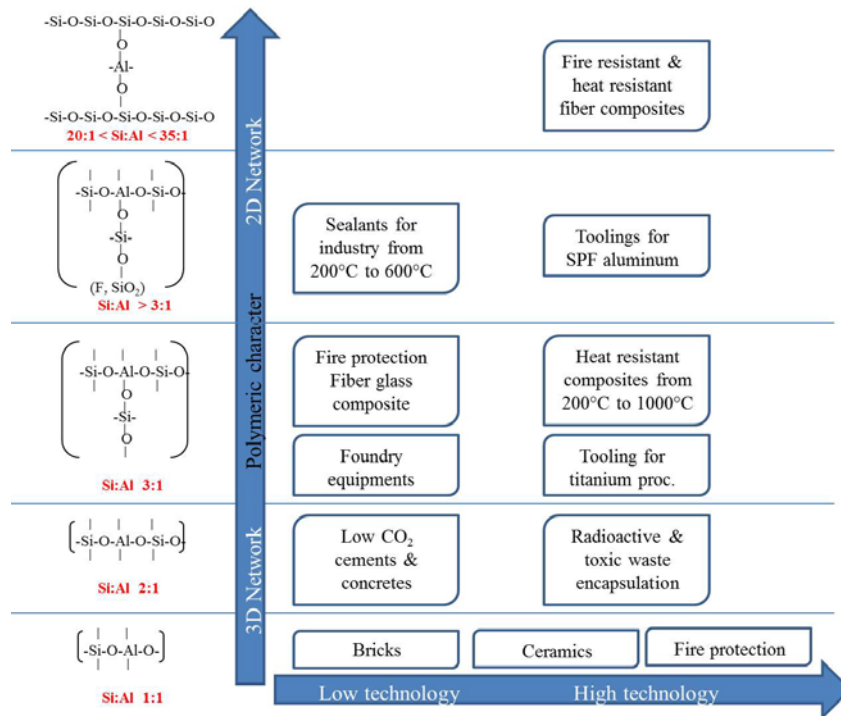


**Figure 2.1** Possible geopolymer applications as a function of the Si:Al molar ratio (adapted from [www.geopolymer.org](http://www.geopolymer.org)).

Metakaolins are the most reactive raw powders because of the thermal activation, the prevalent amorphous phase, the high specific surface area and the cationic coordination. Their reactivity depends on the intrinsic properties of the starting kaolinite clays (morphology and chemical composition) and the dehydroxylation degree, specific surface area and agglomeration, that depend on the process formation (kiln type and calcination temperature) [36].

Kaolin dehydroxylation may occur in two ways as represented in figure 2.2 [21]:

- Intra-dehydroxylation leads to the formation of a metakaolin with aluminum mainly in V-fold coordination, that result to be the most reactive during the geopolymerization.
- Inter-dehydroxylation leads to the formation of a metakaolin with aluminum mainly in IV-fold coordination. The inter-dehydroxylation may be incomplete and hydroxyls remain linked to aluminum in VI-fold coordination.

The desired Al (V) coordination is obtained by calcination temperatures between 700 °C and 800 °C, using rigid (vertical) kiln with a low water vapor pressure during the roasting process [21].

Despite the higher price of metakaolin powders, the produced geopolymers resulted easier to analyze, being the particle morphology more uniform and similar to the plate structure of the starting kaolin and avoiding complexities introduced by the use of fly ashes or slags as raw materials [37]. The use of metakaolin allows to obtain highly reacted and reproducible samples with a more well understood chemical content, essential for high-tech applications. For the mentioned reasons, the process techniques reported in this thesis are mainly applied to metakaolin-based geopolymers.

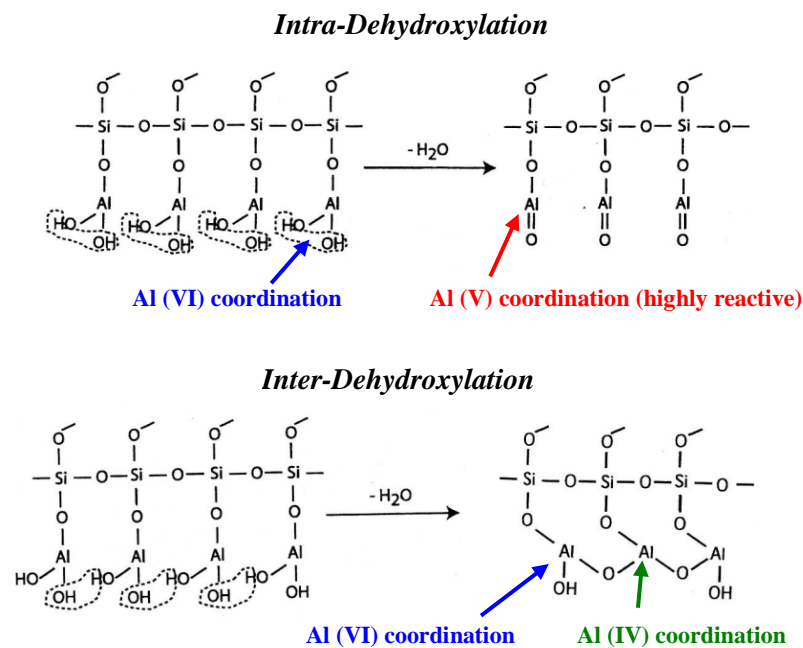


**Figure 2.2** Dehydroxylation mechanisms of kaolin (adapted from Davidovits [21]).

### 2.3.2 Alkali activating solution

Commonly, hydroxides (NaOH, KOH), sulfates (Na<sub>2</sub>SO<sub>4</sub>, K<sub>2</sub>SO<sub>4</sub>), carbonates (Na<sub>2</sub>CO<sub>3</sub>, K<sub>2</sub>CO<sub>3</sub>) and alkaline silicates (K<sub>2</sub>SiO<sub>3</sub>, Na<sub>2</sub>SiO<sub>3</sub>) are used as alkali activators [38]. Sodium and potassium aqueous silicate solutions are the most used. Hydroxide and fumed silica can be added to modify the SiO<sub>2</sub>/M<sub>2</sub>O molar ratio in function of the starting raw materials and the desired final geopolymer structure.

Commercial alkali silicate solutions have high pH in the range 10.9-13.5, deriving

by the  $M_2O$  concentration, and high buffer capacity, showing small pH changes only after neutralization. The pH is a very important parameter that determines the stability of the solution and the tendency to coagulate and form a gel, indeed the stability of the silicate increases with the increase of pH [21]. The pH influences also the time required for the consolidation; an increase of the pH value causes a decrease of the consolidation time [39]. The slurry is viscous as a cement at low pH values while at higher pH values the viscosity decreases and the workability improves [40]. Potassium based silicates have a ten times lower viscosity than sodium based silicates and an higher pH, considering silicates with the same molar ratio and concentration in solution [21].

The low viscosity of the potassium silicate enables to obtain slurries with a good workability through the addition of little water. Since an excess of water may be detrimental for the mechanical properties, the use of potassium silicate is preferred to obtain more mechanically resistant geopolymers [41].

The cations present in the alkali activating solutions influence the alkali hydrolysis and the polymerization during the geopolymerization process. Small cations, with a high charge density, favor the aluminosilicate powder dissolution, while the polymerization and consolidation are enhanced by the presence of bigger cations [22].

The final geopolymer microstructure is affected by the alkali activator, as a matter of fact, potassium-silicate solutions react more readily than sodium solutions forming microstructures with finer precipitate size [42]. This discrepancy is probably caused by the different dissolution kinetics of Al and Si by the activator [43] or the different cation radii of hydration [44].

### **2.3.3 Fillers**

The use of fillers in the geopolymer compositions is useful to give a specific functionality to the material depending on the final application. Fillers may improve the mechanical properties, prevent the shrinkage due to the elimination of water during the consolidation and confer a certain degree of porosity.

The nanoprecipitates formed during the geopolymerization act as glue for the fillers and an accurate choice of the nature and shape of the fillers should be required in order to optimize the final properties. The thermal compatibility with

the geopolymer matrix is the most important aspect of the fillers, in order to avoid thermal stresses during the consolidation of the materials. If the geopolymer matrix tends to contract, fillers have to possess small thermal expansion to prevent the formation and propagation of cracks [45]. Mineral fillers as sand, quartz, corundum, mullite, zircon, alumina etc. are employed to maintain the dimensional stability of the geopolymer composite during the consolidation, thanks to the buffering effect on the linear shrinkage [46].

Furthermore, fillers have to be fully or partially inert during the geopolymerization. The presence of metallic impurities can generate, in alkaline conditions, redox reactions with evolution of gas and subsequent foaming of the slurry [46].

The filler shape affects the final mechanical properties while the chemical composition influences the thermal and physical-chemical properties. Metallic, organic, inorganic, synthetic or natural fillers may be employed for the production of composite geopolymers. Geopolymers, for example, suffer from brittle failure like most ceramics and to overcome this limitation fiber reinforcement is often used to increase the mechanical resistance. The most common fiber reinforcements are based on steel [47-48], carbon [49-50], polypropylene (PP) [51] or polyvinyl alcohol (PVA) [52-53], such as shown in figure 2.3.

Lately, for a more sustainable approach, linked to environment and climate changes, natural fibers often replaced synthetic fibers. Investigations on natural animal or vegetal fibers have revealed desirable effects on the mechanical and thermal properties. Geopolymer resin was reinforced with natural wool fibers showing an approximately 40% improvement in flexural strength compared with the original geopolymer [54]. Similarly, Teixeira-Pinto et al. [55] have found that jute fibers are also effective in the improvement of the mechanical properties of geopolymer composites.

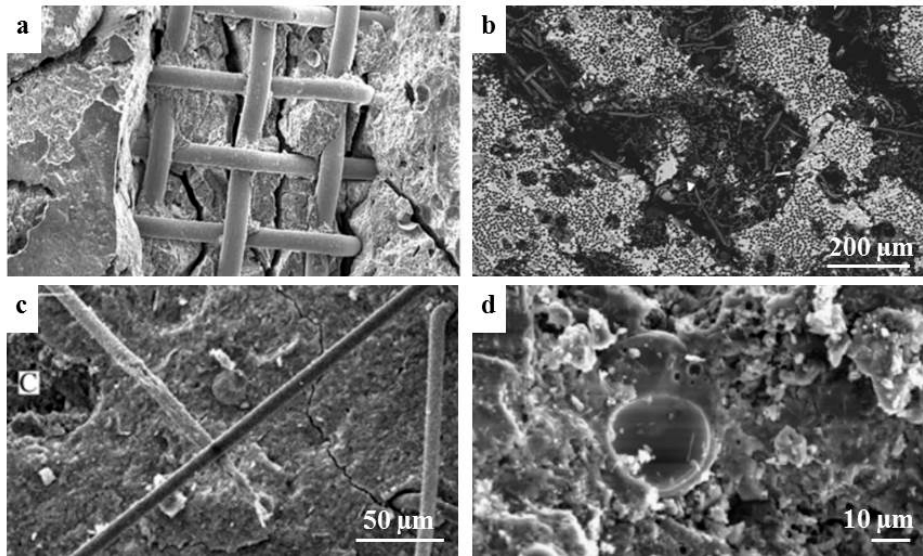


**Figure 2.3** Examples of geopolymer composites with different fiber reinforcements: stainless steel meshes [48] (a), carbon fibers [50] (b), polypropylene fibers [51] (c) and short polyvinyl alcohol fibers [52] (d).

## 2.4 Geopolymer synthesis

Geopolymerization is considered as the analogue of the synthesis of zeolites [56-57]. The chemistry involved is similar, although the final products are different in composition and structure. In fact, zeolites possess a defined stoichiometric composition and crystalline structure, while geopolymers are mixtures of amorphous to semi-crystalline structures.

Geopolymerization is a geosynthesis (i.e, reaction that chemically integrates minerals) that involves naturally occurring silicoaluminates [58]. The reaction involved in geopolymerization may be divided in three main steps: i) the dissolution of the aluminosilicate source material, ii) the polycondensation of aluminosilicate oligomers into precipitate nucleation sites, and iii) the precipitation of individual geopolymer particles. The steps involved in the reaction are simplified in figure 2.4.

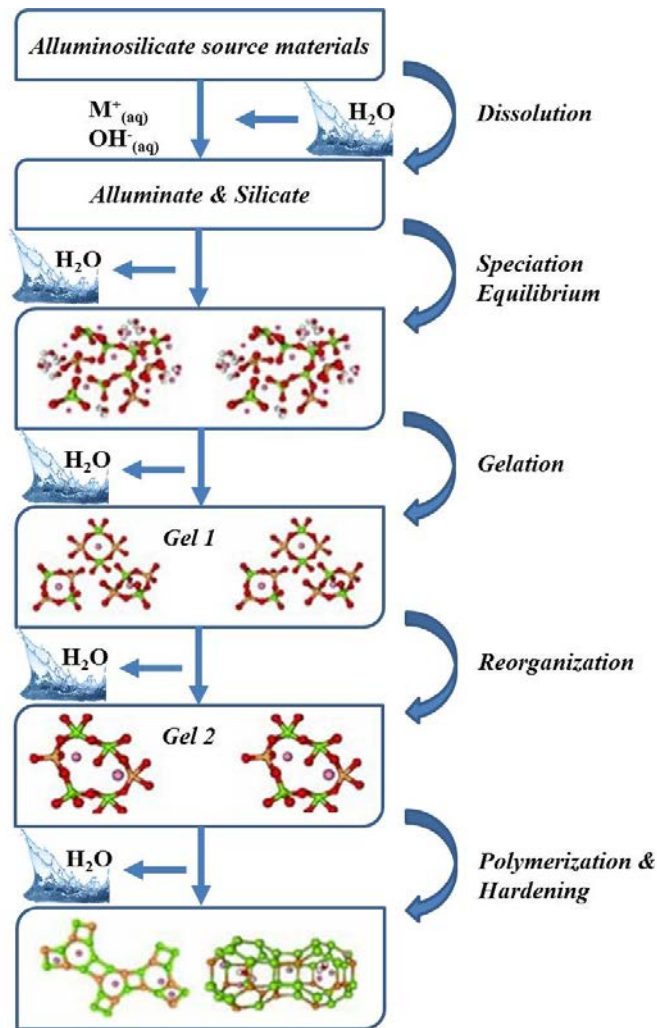


**Figure 2.4** Geopolymer synthesis scheme (adapted from Duxson [59])

Dissolution of the solid aluminosilicate source by alkaline hydrolysis (consuming water) produces monomeric aluminate and silicate species. The species in solution are incorporated into the aqueous phase, which may already contain silicates present in the activating solution; a complex mixture of silicate, aluminate and aluminosilicate species is formed with a speciation equilibria present in solution [59]. The hydrolysis is rapid at high pH and a supersaturated aluminosilicate solution is quickly created with the formation of a gel constituted by the oligomers that form large networks by condensation in the aqueous phase. This process releases the water that was nominally consumed during dissolution.

It is important to underline the role of the water acting as the reaction medium and residing within pores in the gel. The time required for the formation of the gel varies as a function of the raw materials used, the processing conditions and



Davidovits was poly-sialates, an abbreviation for silicon-oxo-aluminate used to describe the bonding of silicon and aluminium by bridging oxygen. Poly-sialates have the empirical formula:



where: n is the degree of polycondensation, z is either 1, 2 or 3 and w describes the water content of the composite. The poly-sialate oligomers are described as chain and ring polymers ranging from amorphous to semi-crystalline [56]. The oligomeric building units are depicted in figure 2.6:

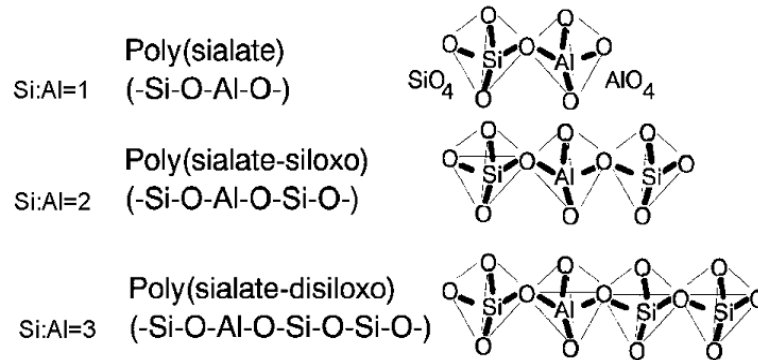


**Figure 2.6** Geopolymer oligomeric building units as a function of the Si:Al ratio [65].

Apart from poly-sialates, poly-sialate-siloxos and poly-sialate-disiloxos, other structural geopolymeric units are possible when the amount of silicate reactants increases in the reaction system.

On an atomic length scale geopolymers are comprised of metal cations of  $\text{Si}^{4+}$  and  $\text{Al}^{3+}$  linked together by oxygen anions,  $\text{O}^{2-}$ . Clusters of these atoms are linked together with a short-range ordering limited to the two or three next-nearest-neighbours of the atom under consideration [3]. The short-range order can be described from merely atomic connectivity to bond lengths, angles and correlation distances between non-covalently linked neighbouring atoms [37]. A basic conceptual view of geopolymer short-range ordering, incorporating only atomic connectivity is illustrated in figure 2.7.

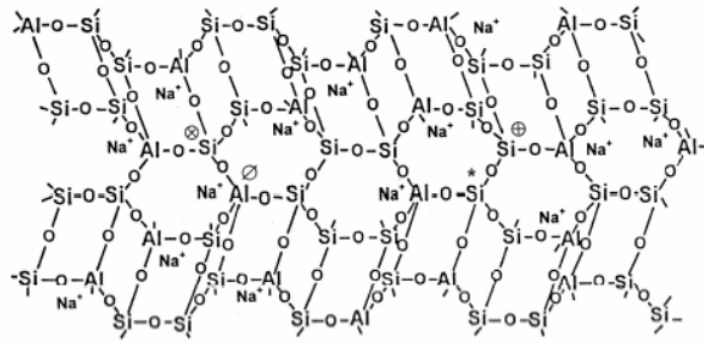


**Figure 2.7** A conceptual view of geopolymer short-range ordering [66].

## 2.6 Geopolymer microstructure and porosity

Gelation from hydrolysis–polycondensation of Al- and Si-containing species, results in a complex network swollen by water trapped in the pores. The final microstructure of a geopolymer is composed of nanoprecipitates in the range 0.01–0.1  $\mu\text{m}$ , which are densely packed according to the hydrolysis–polycondensation rate and the water content [67], commonly investigated using microscopic techniques, such as Scanning Electron Microscopy (SEM) and Transmission Electron Microscopy (TEM).

As mentioned before, the structural reorganization of network occurs by continued reaction and expulsion of the water into larger pores. The water distribution within the gel depends on the Si/Al ratio and the alkali cation used, whilst the total volume of pores depends on the nominal content of water [68]. Since water does not enter into the geopolymer framework [21], it acts as a pore forming agent during its removal in the consolidation step [69–70]. The extensive presence of pores in the length scale of 0.005–0.02  $\mu\text{m}$ , which are considered to be spaces between individual precipitates, was identified by TEM [65] and gas adsorption porosimetry [71].

Geopolymers have shown to have a microporous framework, with the characteristic pore size being determined by the nature of the alkali cation or mixture of cations used in activation; furthermore, the Si/Al ratio affects the microstructure. It is known that for Na-containing geopolymers, synthesized from metakaolin, as the ratio increases in the range from 1.15–2.15, the geopolymer shows a more homogenous structure with some porosity in the  $\mu\text{m}$  length scale. Specimens with  $\text{Si/Al} \leq 1.40$  exhibit a microstructure comprising large

interconnected pores, loosely structured precipitates and unreacted material. Geopolymers with Si/Al ratio  $\geq 1.65$  present a largely homogeneous binder, containing unreacted particles and some smaller isolated pores with dimension of few microns [62].

The nominal content of water affects the total volume of pores and the pore size diameters. It was found that metakaolin-based geopolymers, obtained by the use of increasingly diluted potassium silicate solutions, shown an increase of the total porosity percentages. Total porosity resulted 29, 36, 56 % for samples obtained from potassium di-silicate with dilution  $H_2O/K_2O$  equal to 10.0, 13.5 and 23.0, respectively [72]. The pore size distribution obtained by Hg intrusion porosimetry (Fig. 2.8) resulted affected by the dilution of the starting mixture and the average pore diameter increase from 0.01  $\mu m$  for sample with  $H_2O/K_2O = 10.0$  to 0.54  $\mu m$  for sample with  $H_2O/K_2O = 23.0$ .

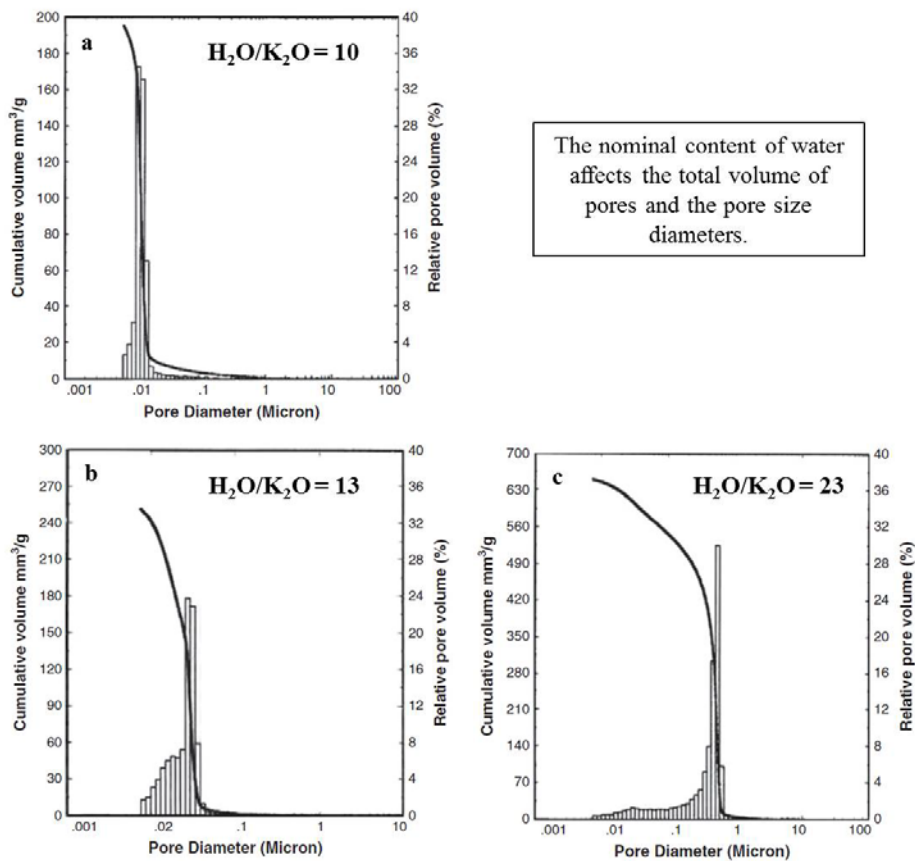


**Figure 2.8** Pore size distribution by Hg mercury intrusion of geopolymers obtained using increasingly diluted potassium silicate solution a)  $H_2O/K_2O=10.0$  b)  $H_2O/K_2O=13.5$  and c)  $H_2O/K_2O=23.0$  [72].

The pores formed are so small to be considered as part of the structural network of the geopolymers, decreasing the final density and forming the “intrinsic” mesoporosity of the material. The geopolymer matrix porosity may be changed, up to cover a range of 0.01-1.00  $\mu\text{m}$ , acting on the Si/Al ratio, using different cations in the activating alkali solution, but especially changing the dilution of the starting mixture. Furthermore, it is possible to artificially add a certain degree of macroporosity to this “intrinsic” geopolymer porosity, in order to achieve hierarchical porous structures with total porosity up to 90 % and pore size dimensions from few tenth of nanometers to some millimeters. The hierarchical porosity achieved by these materials may be useful for different possible applications as schematically depicted in figure 2.9. The porosity of the geopolymers can be modified exploiting different process techniques, that will be described in detail in the following chapters.

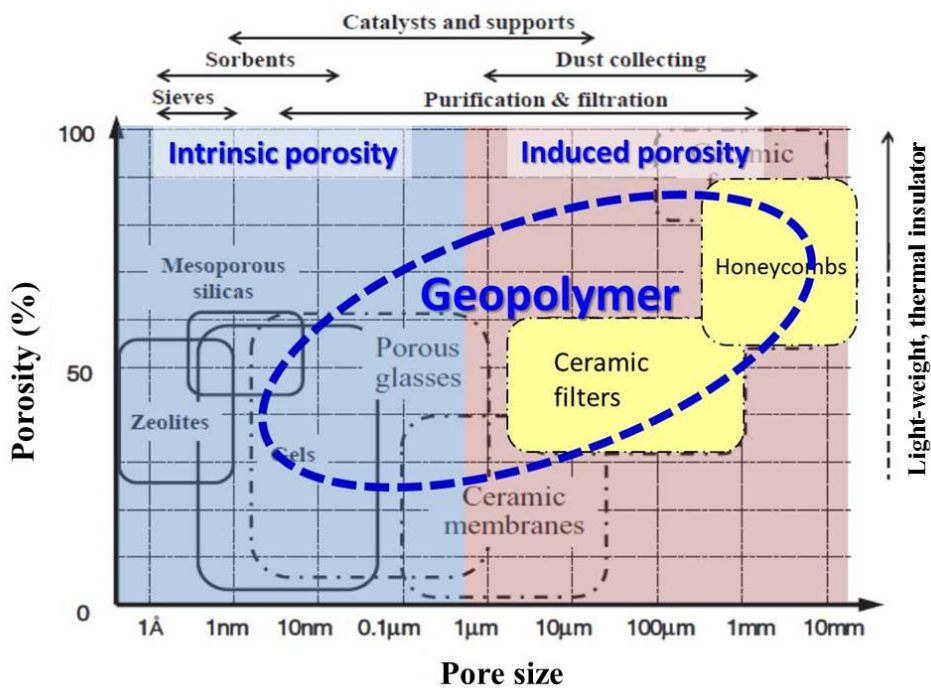


**Figure 2.9** Intrinsic and induced geopolymer porosity and possible applications in function of the pore size dimension and total porosity achieved (adapted from Okada [73]).

## **2.7 Processing techniques for macroporous geopolymers**

Geopolymers are often compared with ceramics for their similar final properties arising from the inorganic structure. The main difference, referring to the process formation of these porous materials, is that ceramic foams are usually treated at high temperature for the burnout of additives or templates and the final consolidation (sintering) that confer the specific mechanical and functional properties. On the other hand, geopolymers have the advantage to be consolidated through a chemical reaction that occurs at low temperature. The geopolymerization process and the final chemical consolidation must be taken into account when a particular technique is chosen, to do not interfere on the reaction synthesis of the material.

In the last decades several processing routes have been developed, determining the possibility to obtain materials with different architectures, pore size distribution, interconnectivity and so on, in order to satisfy the requirements of different specific applications. Methods reported in literature for ceramics materials may be adapted for the production of geopolymers; indirect foaming techniques include the sacrificial template method while the addition of foaming agents leads to a direct foaming of the geopolymer slurry. Rapid prototyping is another technique largely used for ceramic materials and recently applied to geopolymers to produce complex porous structures. Lastly, the use of inert or partially reactive fillers results effective in the production of highly macroporous geopolymer materials.

The description, advantages and drawbacks of each processing route are reported in the following sections.

### **2.7.1 Sacrificial template method**

The sacrificial template method is based on the preparation of a biphasic composite made of a continuous matrix of ceramic particles and a dispersed sacrificial phase. The sacrificial phase is homogeneously dispersed in the matrix and is ultimately extracted to generate the final porous structure. This method leads to a material that possesses a negative replica of the original sacrificial template [74]. A scheme of the technique is reported in figure 2.10.

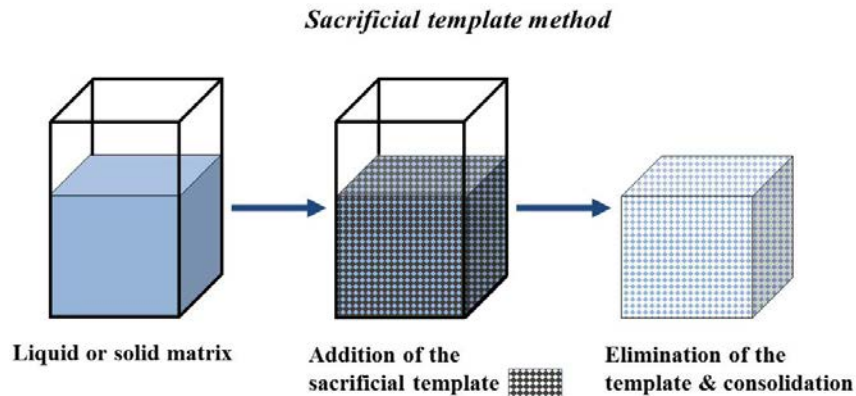


**Figure 2.10** Scheme of the sacrificial template method used to obtain macroporous ceramic materials.

A variety of different materials have been used as sacrificial templates for the production of ceramic materials: natural [75-78] and synthetic organics [79-81], liquids [82-83], salts [75], metals [84] and ceramic compounds [81, 85].

The advantage of the sacrificial template technique is that it is very flexible and is possible to tailor the porosity, pore morphology, pore size distribution of the final ceramic by the choice of the right template. The main drawbacks of this technique are the long period required to complete the removal of the template and the possibility to encounter a mismatch in the thermal expansion coefficient between the matrix and the template, generating cracks within the structure.

In the literature, examples of porous geopolymers obtained through the application of the sacrificial template method are reported. A simple reactive emulsion templating with triglyceride vegetable oil was used with geopolymers to produce hierarchically porous structures without modifying the conventional geopolymer synthesis process [86]. An highly alkaline geopolymer resin was mixed with canola oil forming droplets of oil, that remain embedded in the geopolymer matrix as shown in figure 2.11a. During the process the oil in the alkaline emulsion undergoes a saponification reaction that continues during the curing of the material within the embedded droplets, generating soap and glyceride molecules easy removed during the subsequent hot water extraction.

The material exhibits a macroporous structure of spherical pores with diameter in the range from 5 to 40  $\mu\text{m}$  and a pore wall formed by a finer mesoporous matrix of nanoparticles of about 20 nm (Fig. 2.11 b-c). This simple synthesis shown that

the pore size and volume can be controlled by changing the type of oil used and the water and alkali contents in the precursor solution [86].

Metakaolin geopolymer with porosity of 70 vol % or more and tailored pore size containing small pores (10-200  $\mu\text{m}$ ) was synthesized using another emulsion technique. Alkylalkoxysilanes were used as hydrophobic template to form a film on pore interiors during synthesis and drying, allowing the drainage without pore collapse. The pore volume and pore size resulted to be potentially tuned by manipulating initial water content, quantity of hydrophobic phase, drying humidity and emulsion stability [87].

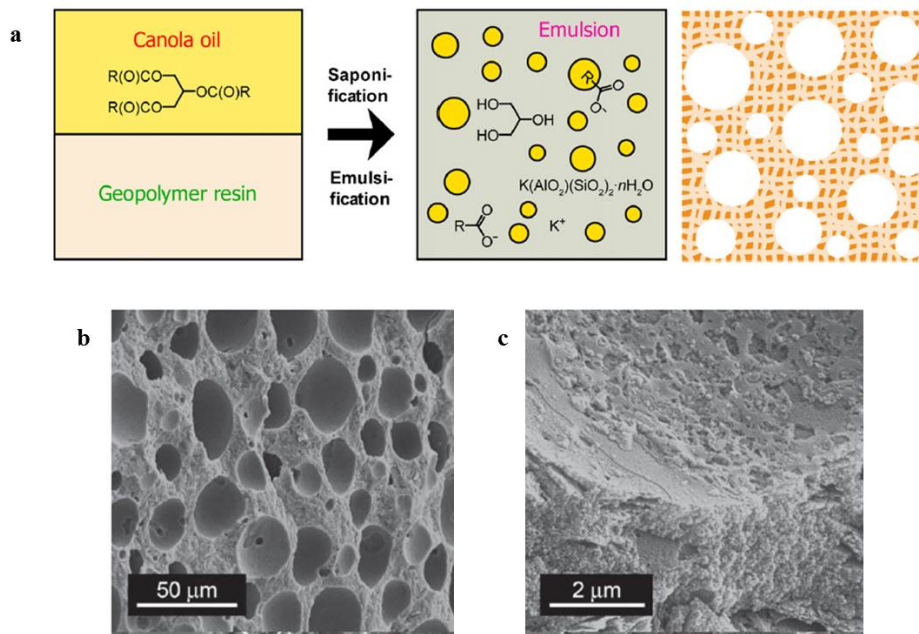


**Figure 2.11** Scheme of the reactive emulsion templating of geopolymer with canola oil (a). SEM images of the macroporous structure (b) and the pore wall microstructure (c) obtained [86].

Geopolymer components with controlled porosity were produced exploiting PLA (poly-lactic acid) sacrificial structures, with different pattern obtained by 3-dimensional printing [88]. The preform was impregnated in vacuum with a geopolymer slurry and, after the chemical consolidation by geopolymerization, the template was removed in a combined chemical and thermal treatment. The 3-dimensional printed templates reproduced the computationally designed porosity obtained in the final geopolymer, in terms of total porosity, average pore size and pore architecture (Fig. 2.12 ). The final total porosity of the different samples, due

to the designed geometrical macroporosity and to the intrinsic micro- and mesoporosity of the geopolymer (~ 30 vol.%), was around 66-71 vol.%. The macroscopic open channels resulted suitable for the permeability of liquid or gas, while the solid struts may be used for the interaction with a fluid when used for filtration or catalytic support [88].

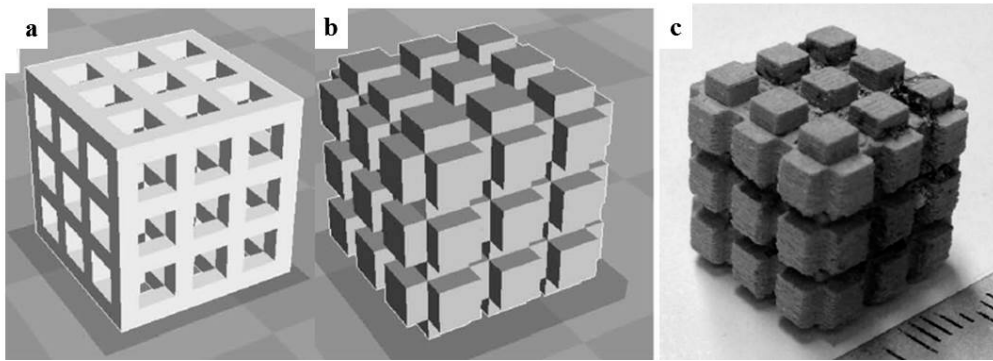


**Figure 2.12** 3-dimensional rendering of the sacrificial template: template used for the geopolymer impregnation (a) and inverse lattice (b). Inverse replica of the lattice after complete PLA degradation (c) [88].

Finally, porous geopolymers were obtained using PLA fibers as pore formers. The fibers were added to the geopolymer slurry and the resulting paste was extruded. The PLA fibers in the composites were removed by alkali treatment and/or heating, generating controlled pore size, aspect ratio and orientation in the final materials (Fig. 2.13). The investigation on the capillary rise revealed that the rates increased by increasing fiber volume and thicker fiber diameter. The highest capillary rise was achieved in geopolymer added with the 28 vol.% of fibers with 29  $\mu\text{m}$  dimension [89].

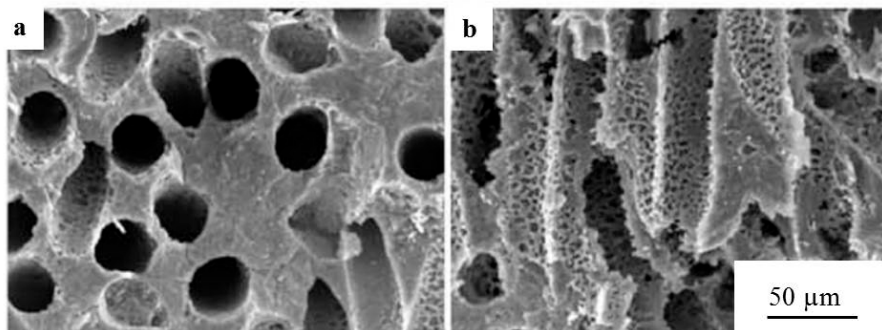


**Figure 2.13** SEM micrographs of fractured surface perpendicular (a) and parallel (b) to the extrusion direction of geopolymer with 28 vol.% of fibers having 29  $\mu\text{m}$  size [89].

### 2.7.1.1 Freeze casting

Freeze casting is a technique that implies the use of liquid sacrificial materials, determining an easy sublimation of the template without the generation of toxic gases and reducing stresses deriving by the pore former removal. This technique is based on the freezing of a liquid suspension (aqueous or not), previously prepared, followed by the sublimation under reduced pressure of the solid phase formed during the freezing. The consolidation and densification of the final porous ceramic is generally obtained by sintering [90]. The four basic freeze casting process procedures are schematically illustrated in figure 2.14. When a unidirectional freezing is applied a porous structure with unidirectional oriented channels pores is obtained, where the pores are the replica of the solvent crystals.

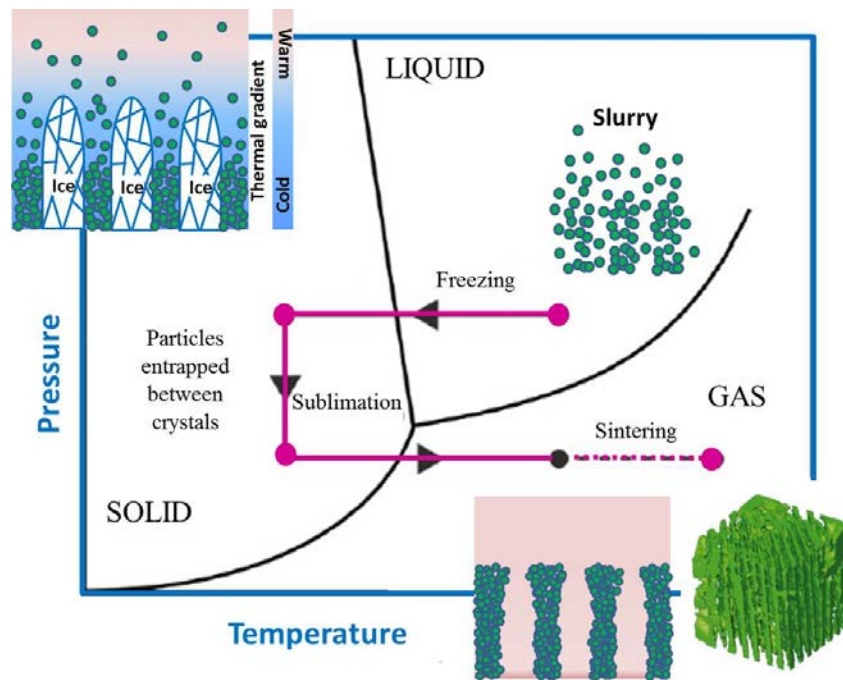


**Figure 2.14** The four process steps of freeze-casting: slurry preparation, solidification, sublimation and sintering (adapted from Deville [90]).

For the preparation of ceramic slurries the ceramic powders has to be well dispersed in the liquid solvent, thus appropriate dispersants are commonly used. In order to obtain the desired porosity, moderate solid loadings are used and the stability of the suspension must be controlled to avoid sedimentation and segregation phenomena that lead to gradients of density and porosity in the final material. The solvent plays the role of structural agent, binder and pores former,

even if at the end is sublimated, so the use of binders and additional additives is fundamental to prevent the possible collapse of the green body [90].

The second step, concerning the controlled solidification of the slurry, is the most critical because the final pore morphology and pore size are formed during this stage. Particles in the slurry are rejected from the advancing solidification front and concentrated between the growing solvent crystals. The solidification conditions are governed by the solvent type. When water is chosen as solvent the physics of ice is the basic theory for the ice-templating technique.

During the freezing, the growing ice crystals expel the ceramic particles, creating a lamellar microstructure oriented in a direction parallel to the moving freezing front. For highly concentrated slurries, the interactions between particles become critical: a small fraction of particles is entrapped within the ice crystals by tip-splitting and subsequent healing, leading to the formation of inorganic arms between adjacent walls (Fig. 2.15) [91].

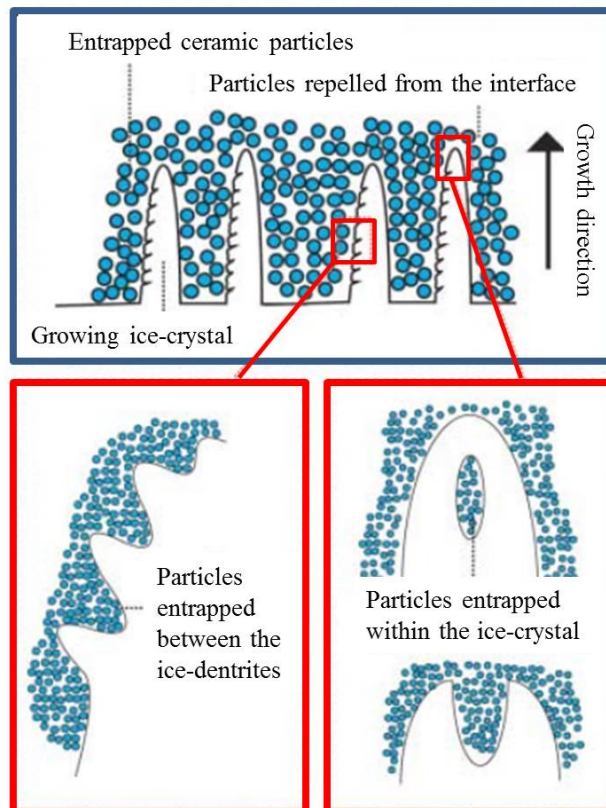


**Figure 2.15** Freezing process: the growing ice crystals expel the ceramic particles in different ways (adapted from Deville [91]).

After solidification, the solvent crystals need to be sublimated at low temperature and reduced pressure in conditions determined by the type of the initial solvent. A green body, with a porosity consisting in a direct replica of the solidified solvent structure, is formed. Finally, to increase the strength of the freeze-cast material, a final sintering step is commonly required [90].

The ice templating method has been applied to a wide variety of materials such as alumina [92-93], hydroxyapatite [94-95], polymeric materials [96], zirconium diborides ultra-high-temperature ceramics [97], zeolite monoliths [98], a.s.o.

While the literature reports ice-templating of colloidal inert ceramic suspensions, in this thesis for the first time (chapter 4) the technique was applied to a water-based sol-gel system able to produce metakaolin-based geopolymers. Geopolymer slurries are based on a sol/gel reactive system without the addition of any organic dispersant or binder, while the consolidation is of chemical type, thus avoiding any high temperature thermal treatment.

The goal of the work, reported later in detail, was to promote the simultaneous formation of geopolymer intrinsic mesoporosity and lamellar macroporosity by unidirectional ice growth, together with a final chemical consolidation.

### 2.7.2 Direct foaming method

Porous materials are obtained by incorporating air into a suspension that afterwards set in order to maintain the structure generated by the bubbles. Usually the consolidated foams are subsequently sintered at high temperature to generate a high mechanical resistance in the ceramic material [74]. The schematic principle of the technique is illustrated in figure 2.16.

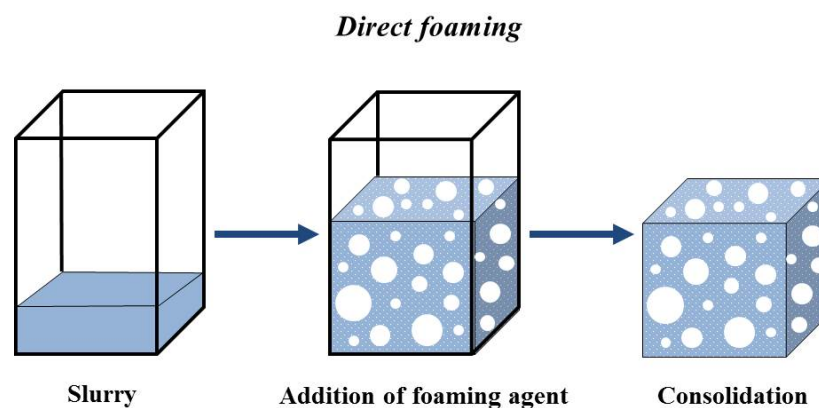


**Figure 2.16** Scheme of the direct foaming method.

The amount of gas, that may be entrapped in the suspension or liquid medium, affects the total porosity of the foamed ceramic, instead the pore size is determined by the stability of the wet foam before the setting. The most important parameter to take into account, during the direct foaming process, is the stabilization of the air bubbles incorporated in the suspension. Two main methods are employed for wet foam stabilization: i) stabilization with surfactants, and ii) stabilization with particles.

The direct foaming method usually leads to dense flawless struts after sintering, determining a higher mechanical strength. The technique is cheap, simple and environmentally friendly and it is possible to obtain final ceramics with various porosity levels and pore size ranges for many different chemical compositions [74].

The direct foaming technique was largely used to obtain geopolymer foams. Some examples on the use of pores agents able to produce porous macrostructures without to require thermal treatments for their elimination are shown below.

As a rule, an increase of the foaming agent amount gives rise to an increase of the total porosity and of the pore size with generation of lightweight consolidate geopolymers [99-101]. The dimension, shape and volume % of the pores depend on the foaming agent and the formation process used. Furthermore, the use of molds with different geometries affects the expansion and the formation of the pores (dimension, shape). Indeed, the foam volume expansion results affected by the ratio between the surface of the foam exposed to the air and the initial volume of the mixture ( $A/V$ ) (Fig. 2.17). This ratio defines the linear expansion ( $L$ ) of the foam that occurs preferentially along the  $z$  axis and represents the distance between the exposed surface before ( $A'$ ) and after ( $A$ ) the expansion (Fig. 2.17) [102].

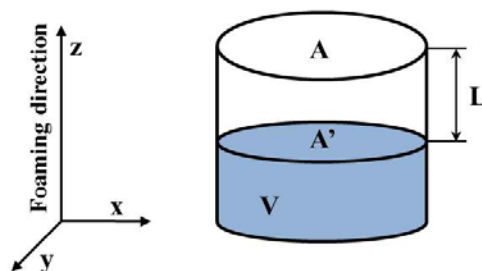
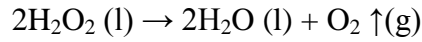


**Figure 2.17** Geometrical parameters that affect the foaming process. Foam preferentially expands along the  $z$  axis.

Different foaming agents can be used with geopolymer slurries, among them hydrogen peroxide  $\text{H}_2\text{O}_2$  is a well-known blowing agent that through an exothermic redox reaction generates water and oxygen [99, 103]:



The geopolymer slurry is directly blown up by the evolution of oxygen, therefore  $\text{H}_2\text{O}_2$  must be added before the casting, to expand before the complete consolidation of the geopolymer. As mentioned before, an increase of the foaming agent content causes an increase of the total porosity and the pore size, as shown in figure 2.18.

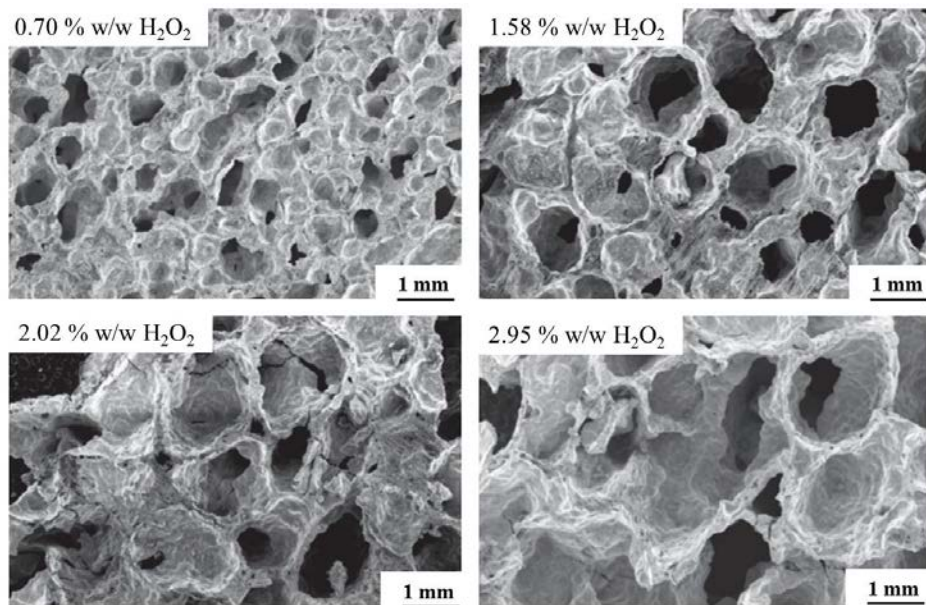
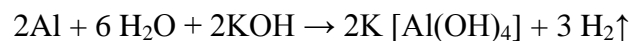


**Figure 2.18** SEM images of foamed geopolymers prepared with different wt.%  $\text{H}_2\text{O}_2$  used as foaming agent (adapted from Vaou [99]).

Metallic powders can be used to generate macroporosity by direct or indirect addition. The direct addition of Al powder in a geopolymer slurry causes the evolution of hydrogen with consequent foaming of the geopolymer slurry:



Also in this case, an increase of the foaming agent leads to an increase of the porosity and pore dimensions, as shown in figure 2.19. Nevertheless, the quantity and dimension of the Al particles and the curing time have to be optimized to consume all the Al before the geopolymer consolidation [104].

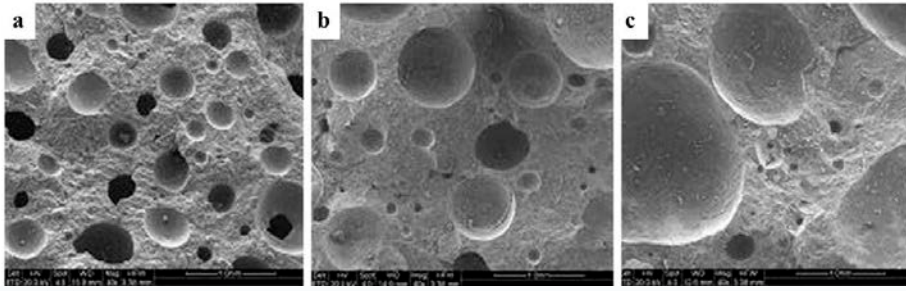


**Figure 2.19** Geopolymer foams obtained using metallic Al powder as foaming agent. An increase of the foaming agent leads to an increase of the porosity and pore size (Al concentration:  $a < b < c$ ) [105].

Similarly, the addition of Si metal powder in the reactive geopolymer slurry causes the formation of geopolymer foams. In alkaline conditions the exothermic redox reaction of Si is always favored [106] and the macroporosity of the foam is generated by the evolution of hydrogen:



In this Thesis will be discussed the use of metallic Si powder to obtain foamed structures with complex shapes (chapter 5). The optimization of the process was based on previous works where the addition of increasing quantities of Si (from 0.03 to 2.60 wt.%) was studied on metakaolin-based geopolymers [72, 107].

The increase of the blowing agent and the use of different curing temperatures lead to structures highly expanded as reported in figure 2.20. A balance between the Si redox reaction and the geopolymerization was necessary to obtain well foamed and fully reacted foams.

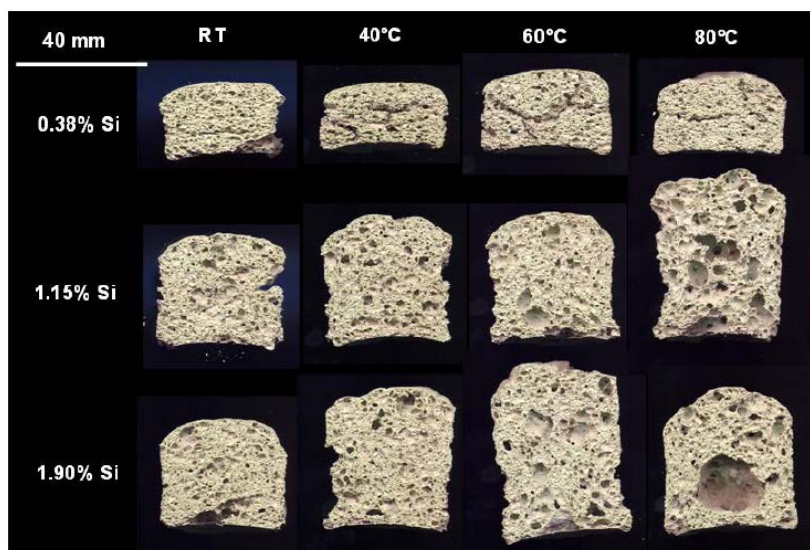


**Figure 2.20** Vertical cross sections of the geopolymer foams obtained changing the wt.% amount of Si, used as blowing agent, and the curing temperature [102].

Excluding the direct addition to aqueous geopolymer slurries of components able to generate in situ the evolution of gas, little work was done on the production of porous geopolymers by alternative ways. One of them was the use of the gel-casting process [108], that belongs to the direct foaming techniques and consists in the stabilization of wet foam, generated by vigorously stirring of a slurry, through surfactants. Geopolymer foams were prepared by stirring an activated blend of metakaolin and fly ash with K-based silicate solution and non-ionic surfactants with hydrophilic groups without electric charges. Foams with a total pore volume of ~ 80 vol.% and an open porosity as high as ~ 60 vol.% (Fig. 2.21), were produced by using this approach, that resulted to be affected by the type of surfactants used and by the process parameters.

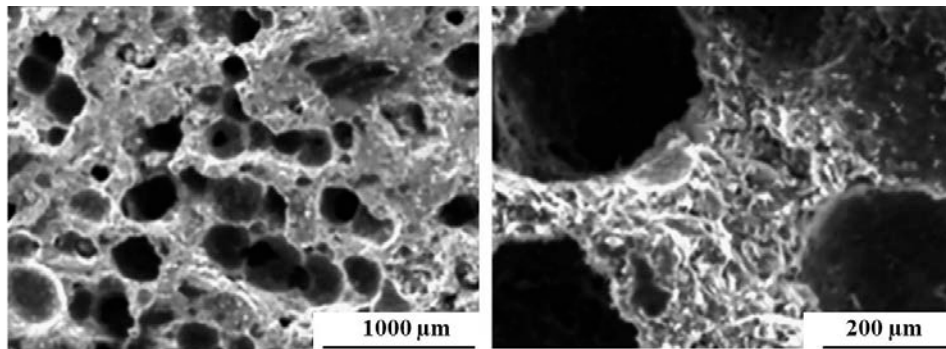


**Figure 2.21** SEM micrographs of the microstructure of the geopolymer foam obtained by gel casting (adapted from Cilla [108]).

### 2.7.3 Solid free-form fabrication

Solid free-form fabrication, also called rapid prototyping technique, has been emerged as a process able to produce prototypes with complex 3-dimensional structures by layered manufacturing.

The production of ceramic involves different solid free-form fabrications: stereolithography of ceramic suspensions, selective laser sintering of packed beds of binder/powder mixtures, selective ink jet printing of binders on a powder bed, ink jet printing of slurries to form freestanding parts, laminated object manufacturing of ceramic green tapes, and computer controlled extrusion [109].

Generally, a CAD representation of the desired part is computationally sliced to produce a series of parallel outlines, then the selected process is used to serially produce thin contoured sheets that correspond to each outline; the contours are assembled and fused to produce a solid finished component (Fig. 2.22) [109].

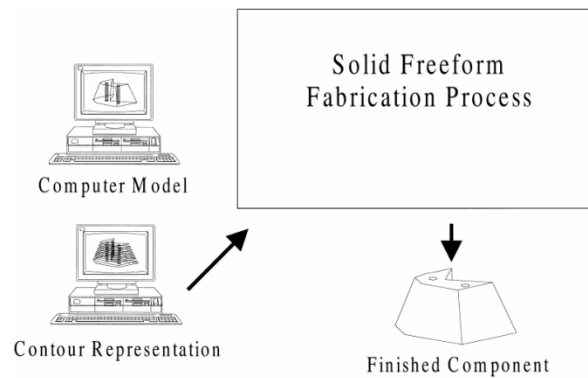


**Figure 2.22** General scheme of the solid freeform fabrication process [109].

Recently, Colombo [110] used for the first time direct and indirect 3-dimensional printing with geopolymer materials. Geopolymer mixtures with suitable rheology were developed for direct ink writing, enabling the fabrication of highly porous scaffolds. Moreover, a binder mixture with suitable reactivity and rheology was sprayed on a bed of ceramic powders, by indirect powder-based 3-dimensional printing, resulting in large scale parts [110].

#### 2.7.4 Addition of fillers to generate porosity

The use of fillers in the geopolymer composition is useful to give a specific functionality to the material as reported in paragraph 2.3.3. Fillers may be inert or reactive in the geopolymer reaction system as a function of their nature, generating a certain degree of macroporosity in the final material as depicted in figure 2.23.

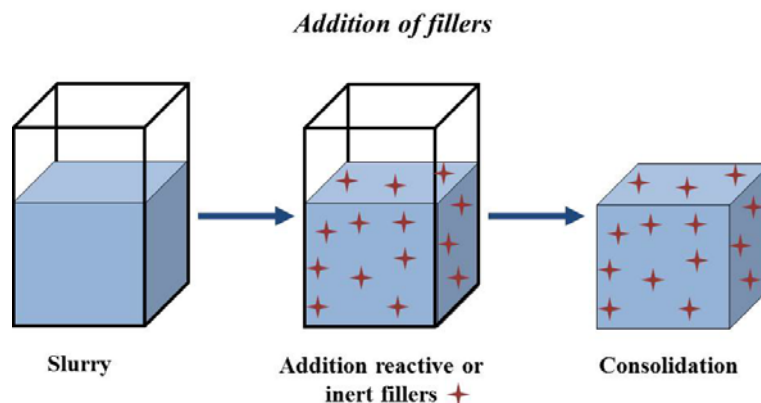


**Figure 2.23** Addition of fillers to generate porosity in the geopolymer slurry.

### 2.7.3.1 Inert fillers

The use of lightweight (expanded) aggregates [111], vermiculite [112], perlite [113], pumice, rice husk and diatomaceous earth [114], etc. together with geopolymers, allows the production of composite masonry blocks, walls and panels with reduced apparent density (due to the introduction of a certain degree of macroporosity into the geopolymer matrix), good mechanical performances and improved thermal properties (insulation, refractoriness and fire resistance).

In this Thesis, an example of the use of expanded vermiculite with a geopolymer binder suitable to generate lightweight panel for insulation applications is reported in chapter 6.1.

### 2.7.3.2 Reactive fillers

The presence of metal impurities, in powders used as starting material source or filler, may be exploited for the production of foamed geopolymer composites. Metallic impurities, in alkaline medium, follow the reaction reported in paragraph 2.7.2, generating the foaming of the geopolymer slurry.

Lately, SiC-based geopolymer foams were produced exploiting the foaming process induced by the presence of metallic Si impurities in the SiC powder (~2%), together with the chemical consolidation caused by the geopolymer binder. Foamed geopolymer, with an high concentration of SiC particles (90 wt.%), were produced with a total porosity of 70-85 vol.% where the geopolymer matrix substantially acts as a binder for the SiC particles (Fig. 2.23) [115-116].

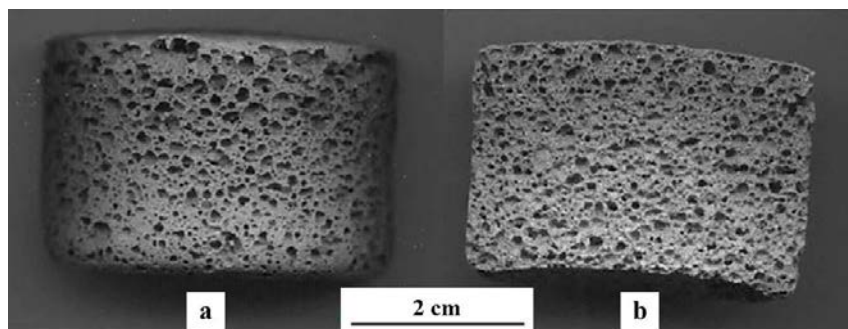


**Figure 2.24** SiC-based geopolymer foam: lateral surface (a) and vertical cross section (b) [102].

Similarly, the presence of small amounts of free metal Si (~ 0.7 wt.%) in silica fume powders allows to obtain macroporous geopolymers. Geopolymer foams were produced adding silica fume to different clays as kaolin, metakaolin, illite, montmorillonite and using potassium based silicate solutions (Fig. 2.24) [100]. A preliminary study based on silica fume based foams is reported in this Thesis in chapter 6.2.

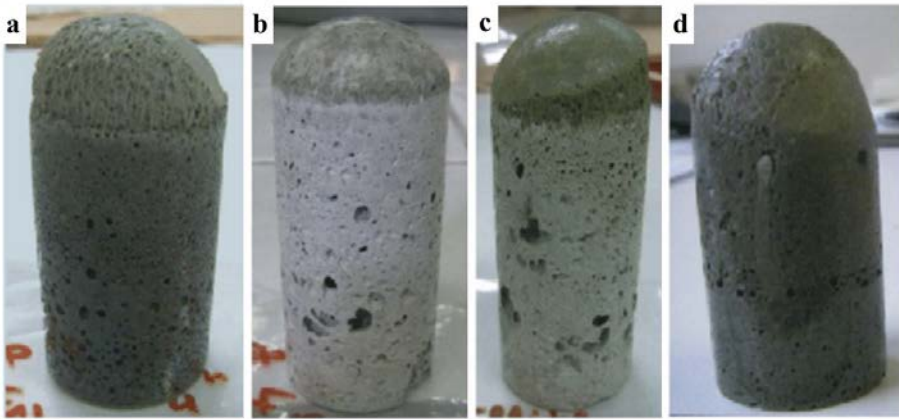


**Figure 2.25** Geopolymer foams obtained from potassium silicate solution, silica fume and metakaolin (a), kaolin (b), illite (c) and montmorillonite (d) [100].

## References

- [1] P.S. Liu, G.F. Chen, Porous materials, processing and applications, Butterworth-Heinemann, 2014.
- [2] R.W. Rice, Porosity of ceramics: properties and applications, CRC Press, 1998.
- [3] K.S.W. Sing, Reporting physisorption data for gas/solid systems with special reference to the determination of surface area and porosity (Recommendations 1984), *Pure Appl. Chem.* 57 (1985) 603-619.
- [4] M. Takahashi, M. Fuji, Synthesis and fabrication of inorganic porous materials: from nanometer to millimeter sizes, *Kona Powder Part. J.* 20 (2002) 84-97.
- [5] M. Scheffler, P. Colombo, Cellular ceramics, Weinheim: Wiley-VCH, 2005.
- [6] I.Y. Guzman, Certain principles of formation of porous ceramic structures. Properties and applications (a review), *Glass Ceram.* 60 (2003) 280-283.

- [7] B.E. Laney, F.T. Williams, R.L. Rutherford, D.T. Bailey, Advanced Geopolymer Composites, US Patent 5244726 (1993).
- [8] F. Frizon, C.J. Dubien, Method of preparing a controlled porosity geopolymer, the resulting geopolymer and the various applications thereof, US Patent Application 2010-0222204 (2010).
- [9] H. Chislitskaya, Acoustic properties of slag alkaline foamed concretes. In: Proceedings of the first international conference on alkaline cements and concretes, P.V. Krivenko (ed.), VIPOL Stock Company, Kiev, Ukraine, Vol. 2 (1994) 971–979.
- [10] P.V. Krivenko, G.Y. Kovalchuk, Heat-resistant fly ash based geocements. In: Proceeding of international conference on geopolymer, G.C. Lukey (ed.), Melbourne, Australia, 2002.
- [11] P.V. Krivenko, G.Y. Kovalchuk, Directed synthesis of alkaline aluminosilicate minerals in a geocement matrix, *J. Mater. Sci.* 42 (2007) 2944–2952.
- [12] J. Davidovits, Polymere Mineral, French Patent Application FR 79.22041 (FR 2,464,227) and FR 80.18970 (FR 2,489,290); US Patent 4,349,386, Mineral polymer, (1979).
- [13] H. Rahier, B. Van Mele, M. Biesemans, J. Wastiels, X. Wu, Low-temperature synthesized aluminosilicate glasses, *J. Mater. Sci.* 31 (1996) 71-79.
- [14] A. Palomo, J.I.L. de la Fuente, Alkali-activated cementitious materials: Alternative matrices for the immobilisation of hazardous wastes: Part I. Stabilisation of boron, *Cem. Conc. Res.* 33 (2003) 281-288.
- [15] D.D. Siemer, Hydroceramics, a "new" cementitious waste form material for U.S. defense-type reprocessing waste, *Mater. Res. Innov.* 6 (2002) 96-104.
- [16] M. Gordon, J. Bell, W.M. Kriven, Geopolymer: alkali bonded ceramics (ABCs) for high-tech applications, *Ceram Trans.* 175 (2006) 215-224.
- [17] V.F.F. Barbosa, K.J.D. MacKenzie, Thermal behaviour of inorganic geopolymers and composites derived from sodium polysialate, *Mater. Res. Bull.* 38 (2003) 319-331.
- [18] J.G.S. Van Jaarsveld, J.S.J. Van Deventer, The effect of metal contaminants on the formation and properties of waste-based geopolymers, *Cement Concrete Res.* 29 (1999) 1189-1200.

- [19] E. Gartner, Industrially interesting approaches to low-CO<sub>2</sub> cements, *Cement Concrete Res.* 34 (2004) 1489-1498.
- [20] G.C. Lukey, J.S.J. van Deventer, Drivers for the establishment of a geopolymer industry. In: *Materials 2003 : International conference and exhibition*, Sydney, Australia, 2003.
- [21] J. Davidovits, *Geopolymer Chemistry and Applications*. Institut Géopolymère, Saint-Quentin (F), (2008).
- [22] X.U. Hua, J.S.J. Van Deventer, The geopolymerization of aluminosilicate minerals, *J. Mineral Process.* 59 (2000) 247-266.
- [23] X.U. Hua, J.S.J. Van Deventer, The effect of alkali metals on the formation of geopolymeric gels from alkali-feldspars, *Colloids Surf. A Physicochem. Eng. Aspects* 216 (2003) 27-44
- [24] X.U. Hua, J.S.J. Van Deventer, G.C. Lukey, Effect of alkali metals on the preferential geopolymerization of stilbite/kaolinite mixtures, *Ind. Eng. Chem. Res.* 40 (2001) 3749-3756.
- [25] M. Rowles, B. O'connor, Chemical optimisation of the compressive strength of aluminosilicate geopolymers synthesised by sodium silicate activation of metakaolinite, *J. Mater. Chem.* 13 (2003) 1161-1165.
- [26] M. Schmucker, K.J.D. Mackenzie, Microstructure of sodium polysialate siloxo geopolymer, *Ceram. Int.* 31 (2005) 433-437.
- [27] A. Fernandez-Jimenez, A. Palomo, M. Criado, Microstructure development of alkali-activated fly ash cement: a descriptive model, *Cem. Concr. Res.* 35 (2005) 1204-1209.
- [28] T. Bakharev, Geopolymeric materials prepared using Class F fly ash and elevated temperature curing, *Cem. Concr. Res.* 35 (2005) 1224-1232.
- [29] W.K.W. Lee, J.S.J. Van Deventer, Effects of anions on the formation of aluminosilicate gel in geopolymers, *Ind. Eng. Chem. Res.* 41 (2002) 4550-4558.
- [30] X.U. Hua, J.S.J. Van Deventer, Geopolymerisation of multiple minerals, *Miner. Eng.* 15 (2002) 1131-1139.
- [31] J.C. Swanepoel, C.A. Strydom, Utilisation of fly ash in a geopolymeric material, *Appl. Geochem.* 17 (2002) 1143-1148.
- [32] P.S. Singh, M. Trigg, I. Burgar, T. Bastow, Geopolymer formation processes at room temperature studied by <sup>29</sup>Si and <sup>27</sup>Al MAS-NMR, *Mater. Sci. Eng. A* 396

(2005) 392-402.

[33] R.A. Fletcher, K.J.D. Mackenzie, C.L. Nicholson, S. Shimada, The composition range of aluminosilicate geopolymers, *J. Eur. Ceram. Soc.* 25 (2005) 1471-1477.

[34] D. Feng, H. Tan, J.S.J. Van Deventer, Ultrasound enhanced geopolymerisation, *J. Mater. Sci.* 39 (2004) 571-580.

[35] Ch. Panagiotopoulou, E. Kontori, Th. Perraki, G. Kakali, Dissolution of aluminosilicate minerals and by-products in alkaline media, *J. Mater. Sci.* 42 (2007) 2967-2973.

[36] V. Medri, S. Fabbri, J. Dedeczek, Z. Sobalik, Z. Tvaruzkova, A. Vaccari, Role of the morphology and the dehydroxylation of metakaolins on geopolymerization, *Appl. Clay Sci.* 50 (2010) 538–545.

[37] P. Duxson, The structure and thermal evolution of metakaolin geopolymers, PhD thesis, Department of Chemical & Biomolecular Engineering, The University of Melbourne, 2006.

[38] D. Khale, R. Chaudhary, Mechanism of geopolymerization and factors influencing its development: a review, *J. Mater. Sci.* 42 (2007) 729–746.

[39] A. Roy, P.J. Schilling, H.C. Eaton, Alkali activated class C fly ash cement, US Patent No. 5435843 (1996).

[40] J.W. Phair, J.S.J. Van Deventer, Effect of silicate activator pH on the leaching and material characteristics of waste-based inorganic polymers, *Miner. Eng.* 14 (2001) 289-304.

[41] V. Medri, Materie prime. In: Geopolimeri: polimeri inorganici chimicamente attivati, C. Leonelli, M. Romagnoli, Lulu.com (2011), 23-43.

[42] J.L. Bell, W.M. Kriven, A.P.R. Johnson, F. Caruso, Laser scanning confocal microscopic analysis of metakaolin-based geopolymers. In: Developments in porous, biological and geopolymer Ceramics: Ceramic Engineering and Science Proceedings, 28 (2007) 273-282.

[43] J.G.S. Van Jaarsveld, J.S.J. Van Deventer, Effect of the alkali metal activator on the properties of fly ash-based geopolymers, *Ind. Eng. Chem. Res.* 38 (1999) 3932-3941.

[44] C. Kuenzel, L.J. Vandeperre, S. Donatello, A.R. Boccaccini, C. Cheeseman, Ambient temperature drying shrinkage and cracking in metakaolin-based

- geopolymers, *J. Am. Ceram. Soc.*, 95 (2012) 3270-3277.
- [45] D.L.Y. Kong, J.G. Sanjayan, Damage behavior of geopolymer composites exposed to elevated temperatures, *Cement Concrete Comp.* 30 (2008) 986–991.
- [46] V. Medri, Materiali compositi a matrice geopolimerica. In: *Geopolimeri: polimeri inorganici chimicamente attivati*, C. Leonelli, M. Romagnoli, Lulu.com (2011), 149-169.
- [47] S. Bernal, R. De Gutierrez, S. Delvasto, E. Rodriguez, Performance of an alkali-activated slag concrete reinforced with steel fibers, *Constr. Build. Mater.* 24 (2010) 208–214.
- [48] Q. Zhao B. Nair T. Rahimian P. Balaguru, Novel geopolymer based composites with enhanced ductility, *J. Mater. Sci.* 42 (2007) 3131–3137.
- [49] T. Lin, D. Jia, P. He, M. Wang, Thermal-mechanical properties of short carbon fiber reinforced geopolymer matrix composites subjected to thermal load, *J. Cent. South Univ. Technol.* 16 (2009) 0881–0886.
- [50] D.H. Tran, D. Kroisová, P. Louda, O. Bortnovsky, P. Bezucha, Effect of curing temperature on flexural properties of silica-based geopolymercarbon reinforced composite, *JAMME* 37 (2009) 492-497.
- [51] Z. Zhang, X. Yao, H. Zhu, S. Hua, Y. Chen, Preparation and mechanical properties of polypropylene fiber reinforced calcined kaolin-fly ash based geopolymer, *J. Cent. South Univ. Technol.* 16 (2009) 49–52.
- [52] Y. Zhang, W. Sun, Z. Li, Impact behavior and microstructural characteristics of PVA fiber reinforced fly ash-geopolymer boards prepared by extrusion technique, *J. Mater. Sci.* 41 (2006) 2787–2794.
- [53] Y. Zhang, W. Sun, Z. Li, X. Zhou, Eddie, C. Chau, Impact properties of geopolymer based extrudates incorporated with fly ash and PVA short fiber, *Constr. Build. Mater.* 22 (2008) 370–383.
- [54] M. Alzeer, K.J.D. MacKenzie, Synthesis and mechanical properties of new fibre-reinforced composites of inorganic polymers with natural wool fibres, *J. Mater. Sci.* 47 (2012) 6958–6965.
- [55] A. Teixeira-Pinto, B. Varela, K. Shrotri, R.S.P. Panandiker, J. Lawson, Geopolymer-jute composite: A novel environmentally friendly composite with fire resistant properties. *Developments in Porous, Biological and Geopolymer Ceramics: Ceramic Engineering and Science Proceedings* 28 (2009) 337–346.

- [56] J. Davidovits, Geopolymers - Inorganic polymeric new materials, *J. Therm. Anal.* 37 (1991) 1633-1656.
- [57] J. Davidovits, Properties of geopolymer cements. First international conference on alkaline cements and concretes, Kiev, Ukraine, VIPOL StockCompany (1994).
- [58] J. Davidovits, Geopolymers: man-made rock geosynthesis and the resulting development of very early high strength cement, *J. Mater. Educ.* 16 (1994) 91-137.
- [59] P. Duxson, A. Fernández-Jiménez, J. L. Provis, G. C. Lukey, A. Palomo, J. S. J. van Deventer, Geopolymer technology: the current state of the art, *J. Mater. Sci.* 42 (2007) 2917–2933.
- [60] R. Aiello, F. Crea, A. Nastro, B. Subotic´, F. Testa, Influence of cations on the physicochemical and structural properties of aluminosilicate gel precursors. Part 1. Chemical and thermal properties, *Zeolites* 11 (1991) 767-775.
- [61] I.I. Ivanova, R. Aiello, J.B. Nagy, F. Crea, E.G. Derouane, N. Dumont, A. Nastro, B. Subotic´, F. Testa, Influence of cations on the physicochemical and structural properties of aluminosilicate gel precursors: II. Multinuclear magnetic resonance characterization, *Micropor. Mater.* 3 (1994) 245-257.
- [62] P. Duxson, J.L. Provis, G.C. Lukey, S.W. Mallicoat, W.M. Kriven, J.S.J. Van Deventer, Understanding the relationship between geopolymer composition, microstructure and mechanical properties, *Colloid. Surf. A* 269 (2005) 47-58.
- [63] P. Rovnanik, Effect of curing temperature on the development of hard structure of metakaolin-based geopolymer, *Constr. Build. Mater.* 24 (2010) 1176-1183.
- [64] J.W. Phair, J.D. Smith, J.S.J. Van Deventer, Characteristics of aluminosilicate hydrogels related to commercial “geopolymers”, *Mater. Lett.*, 57 (2003) 4356-4367.
- [65] W.M. Kriven, J.L. Bell, M. Gordon, Microstructure and microchemistry of fully-reacted geopolymers and geopolymer matrix composites, *Ceram. Trans.* 153 (2004) 227-250.
- [66] V.F.F. Barbosa, K.J.D. MacKenzie, C. Thaumaturgo, Synthesis and characterisation of materials based on inorganic polymers of alumina and silica: sodium polysialate polymers, *Int. J. Inorg. Mater.* 2 (2000) 309-317.

- [67] P. Colomban, Sol-gel control of the micro/nanostructure of functional ceramic-ceramic and metal-ceramic composites, *J. Mater. Res.* 13 (1998) 803-811.
- [68] P. Duxson, G.C. Luckey, J.S.J. Van Deventer, Thermal conductivity of metakaolin geopolymers used as a first approximation for determining gel interconnectivity, *Ind. Eng. Chem. Res.* 45 (2006) 7781-7788
- [69] Z. Zuhua, Y. Xiao, Z. Huajun, C. Yue, Role of water in the synthesis of calcined kaolin-based geopolymer, *Appl. Clay Sci.* 43 (2009) 218-223.
- [70] K. Okada, A. Ooyama, T. Isobe, Y. Nakajima, K.J.D. MacKenzie, Water retention properties of porous geopolymers for use in cooling applications, *J. Eur. Ceram. Soc.* 29 (2009) 1917-1923.
- [71] T.L. Metroke, M.V. Henley, M.I. Hammons, Effect of curing conditions on the porosity characteristics of metakaolin-fly ash geopolymers. In *Strategic Materials and Computational Design: Ceramic Engineering and Science Proceedings*, 31 (2010) 11-15.
- [72] E. Landi, V. Medri, E. Papa, J. Dedecek, P. Klein, P. Benito, A. Vaccari, Alkali-bonded ceramics with hierarchical tailored porosity, *Appl. Clay Sci.* 73 (2013) 56-64.
- [73] K. Okada, T. Isobe, K. Katsumata, Y. Kameshima, A. Nakajima, K.J.D. MacKenzie, Porous ceramics mimicking nature-preparation and properties of microstructures with unidirectionally oriented pores, *Sci. Technol. Adv. Mater.* 12 (2011) 064701.
- [74] A.R. Studart, U.T. Gonzenbach, E. Tervoort, L.J. Gauckler, Processing routes to macroporous ceramics: a review, *J. Am. Ceram. Soc.* 89 (2006), 1771-1789.
- [75] T.J. Fitzgerald, V.J. Michaud, A. Mortensen, Processing of microcellular Sic foams. 2. Ceramic Foam Production, *J. Mater. Sci.* 30 (1995) 1037-1045.
- [76] J. Luyten, S. Mullens, J. Cooymans, A.M. De Wilde, I. Thijs, New processing techniques of ceramic foams, *Adv. Eng. Mater.* 5 (2003) 715-718.
- [77] S.M. Naga, A.A. El-Maghraby, A.M. El-Rafei, P. Greil, T. Khalifa, N.A. Ibrahim, Porous fibrous mullite bodies, *Am. Ceram. Soc. Bull.* 85 (2006) 21-24.
- [78] P.V. Vasconcelos, J.A. Labrincha, J.M.F. Ferreira, Permeability of diatomite layers processed by different colloidal techniques, *J. Eur. Ceram. Soc.* 20 (2000) 201-207.
- [79] R.A. Lopes, A.M. Segadaes, Microstructure, permeability and mechanical

behaviour of ceramic foams, *Mater. Sci. Eng. A-Struct. Mater. Prop. Microstruct. Process.*, 209 (1996) 149–155.

[80] H.F. Yang, G.J. Zhang, N. Kondo, T. Ohji, S. Kanzaki, Synthesis of porous Si<sub>3</sub>N<sub>4</sub> ceramics with rod-shaped pore structure, *J. Am. Ceram. Soc.* 88 (2005) 1030–1032.

[81] H. Wang, I.Y. Sung, X.D. Li, D. Kim, Fabrication of porous SiC ceramics with special morphologies by sacrificing template method, *J. Porous Mater.*, 11 (2004) 265–271.

[82] S.R. Mukai, H. Nishihara, H. Tamon, Formation of monolithic silica gel microhoneycombs (SMHs) using pseudosteady state growth of microstructural ice crystals, *Chem. Commun.* 7 (2004) 874–875.

[83] K. Araki, J.W. Halloran, Porous ceramic bodies with interconnected pore channels by a novel freeze casting technique, *J. Am. Ceram. Soc.* 88 (2005) 1108–1114.

[84] H. Kim, C. da Rosa, M. Boaro, J.M. Vohs, R.J. Gorte, Fabrication of highly porous yttria-stabilized zirconia by acid leaching nickel from a nickel–yttria-stabilized zirconia cermet, *J. Am. Ceram. Soc.* 85 (2002) 1473–1476.

[85] M. Rajamathi, S. Thimmaiah, P.E.D. Morgan, R. Seshadri, Macroporous materials from crystalline single-source precursors through decomposition followed by selective leaching, *J. Mater. Chem.* 11 (2001) 2489–2492.

[86] D. Medpelli, J.-M. Seo, D.-K. Seo, Geopolymer with hierarchically meso-/macroporous structures from reactive emulsion templating, *J. Am. Ceram. Soc.* 97 (2014) 70–73.

[87] B.E. Glad, W.M. Kriven, Highly porous geopolymers through templating and surface interactions, *J. Am. Ceram. Soc.* 98 (2015) 2052–2059.

[88] G. Franchin, P. Colombo, Porous geopolymer components through inverse replica of 3D printed sacrificial templates, *J. Ceram. Sci. Tech.*, 6 (2015) 105–112.

[89] K. Okada, A. Imase, T. Isobe, A. Nakajima, Capillary rise properties of porous geopolymers prepared by an extrusion method using polylactic acid (PLA) fibers as the pore former, *J. Eur. Ceram. Soc.* 31 (2011) 461–467.

[90] S. Deville, Freeze-casting of porous ceramics: a review of current achievements and issue, *Adv. Eng. Mater.* 10 (2008) 155–169.

[91] S. Deville, E. Saiz, R.K. Nalla, A.P. Tomsia, Freezing as a path to build

complex composites, *Science* 311 (2006) 515-518.

[92] T. Fukasawa, Z.Y. Deng, M. Ando, T. Ohji, Y. Goto, Pore structure of porous ceramics synthesized from water-based slurry by freeze-dry process, *J. Mater. Sci.* 36 (2001) 2523-2527.

[93] K. Araki, J.W. Halloran, Porous ceramic bodies with interconnected pore channels by a novel freeze casting technique, *J. Am. Ceram. Soc.* 88 (2005) 1108-1114.

[94] S. Deville, E. Saiz, A. Tomsia, Freeze casting of hydroxyapatite scaffolds for bone tissue engineering, *Biomaterials* 27 (2006) 5480-5489.

[95] E. Landi, F. Valentini, A. Tampieri, Porous hydroxyapatite/gelatine scaffolds with ice-designed channel-like porosity for biomedical applications, *Acta Biomater.* 4 (2008) 1620-1626.

[96] H. Zhang, I. Hussain, M. Brust, M.F. Butler, S.P. Rannard, A.I. Cooper, Aligned two- and three-dimensional structures by directional freezing of polymers and nanoparticles, *Nat. Mater.* 4 (2005) 787-793.

[97] E. Landi, D. Sciti, C. Melandri, V. Medri, Ice templating of ZrB<sub>2</sub> porous architectures, *J. Eur. Ceram. Soc.* 33 (2013) 1599-1607.

[98] H. Mori, K. Aontani, N. Sano, H. Tamon, Synthesis of a hierarchically micro-macroporous structured zeolite monolith by ice-templating, *J. Mater. Chem.* 21 (2011) 5677-5681.

[99] V. Vaou, D. Papias, Thermal insulating foamy geopolymers from perlite, *Miner. Eng.* 23 (2010) 1146-1151.

[100] E. Prud'Homme, P. Michaud, E. Joussein, C. Peyratout, A. Smith, S. Rossignol, In situ inorganic foams prepared from various clays at low temperature, *Appl. Clay Sci.* 51 (2011) 15-22.

[101] E. Prud'Homme, P. Michaud, E. Joussein, C. Peyratout, A. Smith, S. Arri-Clacens, J.M. Clacens, S. Rossignol, Silica fume as porogen agent in geo-materials at low temperature, *J. Eur. Ceram. Soc.* 30 (2010) 1641-1648.

[102] E. Kamseu, E. Landi, Geopolimeri e materiali porosi. In Geopolimeri: polimeri inorganici chimicamente attivati, C. Leonelli, M. Romagnoli, Lulu.com (2011) 222-251.

[103] W. Van Bonin, U. Nehen, U. Von Gizycki, Hydrogen peroxides blowing agent for silicate foams, US Patent 3, 864,137 (1975).

- [104] J.L. Bell, W.M. Kriven, Preparation of ceramic foams from metakaolin-based geopolymer gels. In: *Developments in Strategic Materials: Ceramic Engineering and Science Proceedings*, 29 (2009) 97-111.
- [105] E. Kamseu, B. Nait-Ali, M.C. Bignozzi, C. Leonelli, S. Rossignol, D.S. Smith, Bulk composition and microstructure dependence of effective thermal conductivity of porous inorganic polymer cements, *J. Eur. Ceram. Soc.* 32 (2012) 1593–1603.
- [106] X.G. Zhang, *Electrochemistry of silicon and its oxide*, Kluwer Academic/Plenum Publishers, New York, 2001
- [107] V. Medri, E. Papa, J. Dedecek, H. Jirglova, P. Benito, A. Vaccari, E. Landi, Effect of metallic Si addition on polymerization degree of *in situ* foamed alkali-aluminosilicates, *Ceram. Internat.* 39 (2013) 7657-7668.
- [108] M. Strozi Cilla, P. Colombo, M.R. Morellia, Geopolymer Foams by Gelcasting, *Ceram. Internat.* 40 (2014) 5723–5730.
- [109] J.D. Cawley, Solid freeform fabrication of ceramics, *Curr. Opin. Solid St. M.* 4 (1999) 483–489.
- [110] P. Colombo, G. Franchin, H. Elsayed, A. Conte, P. Scanferla, A. De Marzi, L. Grossi, A. Italiano, Processi innovative di fabbricazione utilizzando geopolimeri, VIII Giornata di Studio del Gruppo di lavoro “Geopolimeri”, Padova, Italy (2015).
- [111] P. Posi, C. Teerachanwit, C. Tanutong, S. Limkamoltip, S. Lertnimoolchai, V. Sata, P. Chindaprasirt, Lightweight geopolymer concrete containing aggregate from recycle lightweight block, *Mater. Des.* 52 (2013) 580–586.
- [112] L. Zuda, J. Drchalov, P. Rovnan, P. Bayer, Z. Keršner, R. Cerny, Alkali-activated aluminosilicate composite with heat-resistant lightweight aggregates exposed to high temperatures: Mechanical and water transport properties, *Cem. Concr. Compos.* 32 (2010) 157–163.
- [113] E.R. Vance, D.S. Perera, P. Imperia, D.J. Cassidy, J. Davis, J.T. Gourley, Perlite waste as a precursor for geopolymer formation, *J. Aust. Ceram. Soc.* 45 (2009) 44–49.
- [114] K. Pimraksa, P. Chindaprasirt, A. Rungchet, K. Sagoe-Crentsil, T. Sato, Lightweight geopolymer made of highly porous siliceous materials with various  $\text{Na}_2\text{O}/\text{Al}_2\text{O}_3$  and  $\text{SiO}_2/\text{Al}_2\text{O}_3$  ratios, *Mater. Sci. Eng. A* 528 (2011) 6616–6623.

[115] V. Medri, A. Ruffini, Alkali-bonded SiC based foams, *J. Eur. Ceram. Soc.* 32 (2011) 1907-1913.

[116] V. Medri, A. Ruffini, The influence of process parameters on *in situ* inorganic foaming of alkali-bonded SiC based foams, *Ceram. Internat.* 38 (2011) 3351–3359.

### 3. Experimental procedures

This chapter reports the procedure and the raw materials used for the production of the starting geopolymer slurries. In this Thesis many types of geopolymer samples were produced and characterized using the different analytical techniques described below. Due to the wide nature of this study, some specific details on the experimental procedures have been also described in the relevant chapters.

#### 3.1 General preparation of the geopolymer slurries

Geopolymers synthesis typically requires an alluminosilicate starting powder, an activating alkali aqueous solution and fillers, when required. The general starting geopolymer mixtures, used and reported in this Thesis, are obtained from a commercial metakaolin and aqueous potassium silicate solutions. The commercial Argical M1200S metakaolin was purchased from Imerys (F) and has the composition and characteristics reported in Table 3.1.

The activating alkali solutions are prepared by dissolving KOH pellets (purity > 85 % from Sigma-Aldrich) in deionized water and adding fumed silica powder (99.8 % from Sigma-Aldrich) under magnetic stirring. Potassium silicate solutions were prepared with a molar ratio  $\text{SiO}_2:\text{K}_2\text{O} = 2.0$  and  $\text{H}_2\text{O}:\text{K}_2\text{O} = 12.0, 13.5$  and  $23.0$ . The corresponding slurries obtained by mechanical mixing (100 r.p.m., for different time) of the metakaolin with the silicate solutions are coded in the Thesis as G12, G13 and G23, respectively.

When other powders and fillers are used for the production of the samples, the information on the raw materials and modifications in the preparative of the starting slurries are reported in the related chapter.

**Table 3.1** Chemical composition and characteristics of commercial metakaolin Argical M1200S.

Chemical composition (%)						$D_{50}$ ( $\mu\text{m}$ )	Ssa ( $\text{m}^2 \text{g}^{-1}$ )	Crystalline phase
$\text{Al}_2\text{O}_3$	$\text{SiO}_2$	$\text{Fe}_2\text{O}_3$	$\text{TiO}_2$	$\text{K}_2\text{O} + \text{Na}_2\text{O}$	$\text{CaO} + \text{MgO}$			
39.0	55.0	1.8	1.5	1.0	1.0	1.7	19.0	Quartz Muscovite

## **3.2 Characterization techniques**

### **3.2.1 Viscosity measurement**

The rheological properties of the starting geopolymer slurries were characterized by a controlled-stress rotational rheometer (Bohlin C-VOR 120, Malvern, UK) equipped with a parallel plate sensor with 20 mm (PP20) or 60 mm (PP60) diameter and forcing the gap to 0.5 or 1 mm [1-2]. The geopolymer slurries were prepared manually outside the rheometer, then introduced on the plate after mixing. Flow curves were determined by increasing the shear rate from 0 to 100 s<sup>-1</sup> and then decreasing from 100 to 0 s<sup>-1</sup>.

### **3.2.2 Macrostructure characterization**

The macrostructure of the samples was investigated by the observation of high resolution photos (3264 x 2448 pixel) or scanner images (1200 dpi, Sharp, JX330). The macropore size distributions, pore length and pore width, were investigated through image analysis of the high resolution photos, using the open source program ImageJ [3].

### **3.2.3 Micro Computed Tomography ( $\mu$ -CT)**

The 3-dimensional internal structures of geopolymer monoliths produced by means of ice-templating technique (chapter 4) were studied by  $\mu$ -CT. The samples were scanned using the Skyscan Micro-CT system model 1172 (Skyscan Bruker, Kontich, B). The SkyScan 1172 scanner was operated at 100 kV and 100  $\mu$ A, and the exposure time was set to 240 ms. Scanning was performed by 180° rotation around the vertical axis and with a rotation step of 0.2°. During the scanning, a 0.5-mm Al filter was used to improve the quality of the images. The necessary field of view (FOV) for the sample was determined, resulting in an optimal image pixel size of 9.8  $\mu$ m. The projected images were reconstructed in 2000 x 2000 pixel-sized cross-sectional images using a modified Feldkamp cone-beam reconstruction algorithm [4] (NRecon, v.1.6.9 software; Skyscan Bruker). The slices were converted into an 8-bit BMP output format and the values within the dynamic range were mapped into gray levels 0 – 255. This output format was suitable for the further processing and the structural information, as volume fraction and structure orientation, was obtained from binary images using

commercially available software CTan, v. 1.14.4; Skyscan Bruker. The solid/pore threshold was set by both trying different values and visually inspecting the appearance of the cross sections [5]. A variation in the threshold +/- 2 results in a variation of structural parameters, such as porosity, of less than 1 %.

### **3.2.4 Microstructure characterization**

The morphological and microstructural features of geopolymers were examined by Environmental Scanning Electron Microscopy (E-SEM FEI Quanta 200, FEI Co.) and SEM-FEG (Zeiss) [6]. The sample pieces observed, were first stuck on SEM stubs (stainless steel) by means of a carbon adhesive tape or paste.

### **3.2.5 True density**

The true density ( $\rho_0$ ) - i.e. mass/volume of the solid - of the samples was determined by He pycnometry (Multivolume pycnometer 1305 by Micrometrics) [7]. The analysis were performed on ground and 150  $\mu\text{m}$  sieved samples.

### **3.2.6 Bulk density**

The bulk density ( $\rho$ ) of samples was determined by weight-to-volume ratio. The volume was geometrically measured by using a caliper (accuracy $\pm$ 0.05 mm).

### **3.2.7 Total porosity**

The percent values of sample total porosity ( $X_p$ ) were calculated according to the equation (1), using the bulk and true density calculated as reported above.

$$\text{Total porosity - } X_p (\%) = [1 - (\text{bulk density} / \text{true density})] \times 100 \quad (1)$$

### **3.2.8 Mercury Intrusion Porosimetry (MIP)**

The pore size distribution in the range 0.0058–100  $\mu\text{m}$  was analyzed by Hg porosimetry [8] (surface tension = 0.48 N/m and contact angle = 140°, Thermo Finnigan Pascal 140 and Thermo Finnigan Pascal 240). From the analysis, the pore size distribution and the values of total pore volume, modal, median and the maximum frequency diameter, were used to characterize the geopolymer materials obtained. The measurement error is related to the accuracy of Hg intrusion

porosimetry (< 4 %).

### **3.2.9 N<sub>2</sub> adsorption/desorption analysis**

Measurements of specific surface areas, pore volumes, and pore size distributions in the 2-500 nm range were carried out in a Micromeritics ASAP 2020 instrument by N<sub>2</sub> adsorption/desorption at -196 °C. Samples were previously degassed under vacuum, heated up to 250 °C, and maintained for 60 min at a pressure below 15 µm Hg. The specific surface area (Ssa) was calculated by the Brunauer–Emmet–Teller (BET) method [9-10]. The total pore volume was obtained at  $p/p_0 = 0.995$ . Pore size distributions were obtained by the BJH method using the desorption branch [11]. The obtained isotherms were classified according to IUPAC [12]. Powders belonging to ground and 600 µm sieved samples were analyzed. The measurement error is related to the accuracy of N<sub>2</sub> adsorption/desorption techniques (< 1 %).

### **3.2.10 Specific surface area**

Specific surface area values (Ssa) by Brunauer–Emmet–Teller (BET) analysis [13] were obtained using a Sorptly 1750 (Carlo Erba Instrument, Milan, I) instrument. The analyses were performed on ground and sieved samples; the fraction collected between 1mm and 600 µm was used for the analysis.

### **3.2.11 Stability in water**

The stability in water was checked by complete immersion of cubic specimens (10 mm side) in deionized water at 25 °C for 11 d. Samples were preventively dried in a heater at 100 °C and, after cooling, their mass was measured. Samples were held by thin supports to avoid any contact with the bottom of the closed vessel. The mass of wet specimens was measured to calculate the maximum percentage of absorbed water (WS) reached after saturation, while the weight loss percent was calculated on the mass of the tested specimens after drying at 100 °C.

### **3.2.12 Linear Shrinkage Measurement**

The linear shrinkage of the samples was obtained using the measurement of the sample dimensions before and after the thermal treatment applied, and calculated

by the following equation (2):

$$\text{Linear shrinkage (\%)} = [(L_0 - L) / L_0] \times 100 \quad (2)$$

where  $L_0$  is the dimension of the sample before and  $L$  after the thermal treatment.

### **3.2.13 Attenuated Total Reflection - Fourier Transform Infrared Spectroscopy (ATR-FTIR)**

ATR-FTIR spectroscopy [14] was used to investigate the formation of the silica fume-based foams, during time evolution (paragraph 6.2). The spectra were obtained from a ThermoFischer Scientific 380 infrared spectrometer (Nicolet Instrument) using the attenuated total reflection (ATR) apparatus. The FTIR spectra were gathered between 500 and 4000  $\text{cm}^{-1}$ . The acquisition was begun with the deposition of a drop of the reacting mixture onto a diamond substrate. The commercially available software OMNIC (Nicolet Instruments) was used for data acquisition and spectral analysis; to remove the atmospheric  $\text{CO}_2$  contribution the spectra were corrected and normalized. To monitor the foam formation, spectra were acquired every 10 min for a total of 69 spectra.

### **3.2.14 X-Ray Diffraction (XRD)**

The mineralogical composition of the geopolymer specimens was evaluated by X-ray powder diffraction (XRD) [15] (Bruker D8 Advance in theta–theta configuration; scanning: 4–80  $2\theta$ ; Cu- $K_\alpha$  radiation,  $\lambda=0.15406$  nm; 40 kV; 40 mA), a technique that allows to identify the crystalline phases in the solid materials. Shreds of the samples were selected, milled and 100  $\mu\text{m}$  sieved to obtain the powders suitable for the analysis.

### **3.2.15 X-Ray Fluorescence (XRF)**

The chemical composition, the Si/Al and K/Al molar ratios in the final consolidated samples were determined by X-ray Fluorescence (XRF) analysis [16]. Measurements were performed in a PANalytical Axios Advanced WD-XRF (wave length dispersive x-ray fluorescence) Spectrometer, equipped by a X-ray tube (Rh target) working at 4 kW. The pellets to be analyzed (diameter 13 mm) were prepared by mixing 0.300 g of the sample with 0.100 g wax (binder) at 100

kN for 120 min.

### **3.2.16 Flexural strength**

Flexural strength was measured on 100 mm × 20 mm × 20 mm prisms, using a three-point jig with a span of 80 mm on a universal screw-type testing machine Zwick mod. Z050 (Zwick, Ulm, D) using a cross-head speed of 3mm min<sup>-1</sup>. At least 5 prisms for each material were tested. The flexural strength was calculated according to the formula (3):

$$\sigma = 3 \cdot F \cdot l / (2 \cdot b \cdot h^2) \quad (3)$$

where:  $\sigma$  = fracture stress (MPa),  $F$  = peak force at fracture (N),  $l$  = jig span (mm),  $b$  = test piece width (mm),  $h$  = test piece thickness (mm).

### **3.2.17 Compressive strength**

Compressive strength tests were performed on 5 cubic specimens with 20 mm side. The load was applied both perpendicular and parallel to the casting direction of the samples. A testing machine (Zwick Z050, Ulm, D) and a cross-head speed of 2 mm min<sup>-1</sup> were used for the tests.

### **3.2.18 Dilatometric analysis**

The thermal behaviour of the samples was investigated by dilatometric analysis, performed with a dilatometer DIL402E Netzsch (D) [17-18]. The characterization were performed up to 1200 °C in static air (heating rate 10 °C/min) and the recorded data were elaborated by Proteus Analysis Software.

### **3.2.19 Thermal conductivity**

The thermal conductivity of the vermiculite-based geopolymer panels (paragraph 6.1) was measured with a heat flow meter DTC 300 (TA Instruments, New Castle, USA) according to ASTM E1530 and UNI EN 12664 standard methods [19-20]. Cylindrical specimens (50.8 mm diameter and 6.0 mm thickness) were obtained by coring and machining the panels. Samples were tested in dry conditions (oven-dried at 50 °C until constant mass conditions were reached, conventionally reached when the percentage reduction in mass was about 0.2 %) and at a mean temperature of about 10 °C. At least three specimens for each composition were

tested. The circular surfaces of the samples were grinded in order to reach a high degree of smoothness, reducing the contact resistance at the interface with the measuring apparatus. The use of silicic thermal compound and a reproducible pneumatic load between the machine plates and the samples, further helped to reach a perfect thermal contact and ensure a higher reproducibility of the results. The thermal conductivity of the silica fume-based foams (paragraph 6.2) was analyzed using a hot disk thermal constant analyzer. The analysis was based on the theory of the transient plane source where the sensor in the shape of a double spiral acted as a heat source, to increase the temperature of the sample, and temperature sensor, for recording the time-dependent temperature increase [21]. For each composition, eight samples, with a diameter of 5 cm and a thickness varying from 1.3 to 2.2 cm, were prepared, cut and polished to obtain planar surfaces. The probe for the analysis was inserted between two samples of each composition and the values were collected positioning the probe in three different points. The final thermal conductivity values were given as an average of the collected data.

## References

- [1] G. Schramm, A practical approach to rheology and rheometry, Haake (1994).
- [2] A. Poulesquen, F. Frizon, D. Lambertin , Rheological behavior of alkali-activated metakaolin during geopolymerization, *J. Non-Cryst. Solids* 357 (2011) 3565–3571.
- [3] [imagej.nih.gov/ij/](http://imagej.nih.gov/ij/)
- [4] L.A. Feldkamp, L.C. Davis, J.W. Kress, Practical cone-beam algorithm, *J. Opt. Soc. Am.* 1 (1984) 612–619.
- [5] S. Bugani, M. Camaiti, L. Morselli, E. Van de Castele, K. Janssens, Investigating morphological changes in treated vs. untreated stone building materials by x-ray micro-CT, *Anal. Bioanal. Chem.* 391 (2008) 1343–1350.
- [6] W. Zhou, R. Apkarian, Z.L. Wang, D. Joy, Fundamentals of scanning electron microscopy (SEM). In: Scanning microscopy for nanotechnology, Springer New York (2007) 1-40.
- [7] P.A. Webb, Volume and Density Determinations for Particle Technologists

- Micromeritics Instrument Corp., Norcross, Georgia, USA (2001) 1-16.
- [8] H. Giesche, Mercury porosimetry: a general (practical) overview, *Part. Part. Syst. Charact.* 23 (2006) 1-11.
- [9] G. Fagerlund, Determination of specific surface by the BET method, *Mater. Struct.* 6 (1973) 239-245.
- [10] S. Lowell, J.E. Shields, M.A. Thomas, M. Thommes, Characterization of porous solids and powders: surface area, pore size, and density, Springer (2004).
- [11] E.P. Barret, L.G. Joyner, P.H. Halenda, the determination of pore volume and area distributions in porous substances. I. Computations from nitrogen isotherms, *J. Am. Chem. Soc.* 73 (1951) 373-380.
- [12] K.S.W. Sing, R.T. Williams, Physisorption hysteresis loops and the characterization of nonporous materials, *Adsorpt. Sci. Technol.* 22 (2004) 773-782.
- [13] S. Brunauer, P.H. Emmett, E. Teller, Adsorption of Gases in Multimolecular Layers, *J. Am. Chem. Soc.* 60 (1938) 309–319.
- [14] G. Ramer, B. Lendl, Attenuated total reflection Fourier transform infrared spectroscopy, Encyclopedia of Analytical Chemistry, John Wiley & Sons, Ltd. (2013).
- [15] B. E. Warren, X-Ray Diffraction, Addison-Wesley, Reading, MA (1969).
- [16] T.G. Duimakaeva, A.L. Tsvetyansky, V.N. Losev, Basic theory and methods of X-ray fluorescence analysis, *Fresenius Z. Anal. Chem.* 335 (1989) 49-53.
- [17] J.D. James, J.A. Spittle, S.G.R. Brown, R.W. Evans, A review of measurement techniques for the thermal expansion coefficient of metals and alloys at elevated temperatures, *Meas. Sci. Technol.* 12 (2001) R1–R15.
- [18] Principles of push-rod dilatometry, Anter Corporation, technical note 69 (2002).
- [19] ASTM, E1530-11, Standard Test Method for Evaluating the Resistance to Thermal Transmission of Materials by the Guarded Heat Flow Meter Technique, ASTM International, West Conshohocken PA (USA), 2011.
- [20] UNI EN 12664, Thermal Performance of Building Materials and Products — Determination of Thermal Resistance by Means of Guarded Hot Plate and Heat Flow Meter Methods — Products of Low and Medium Thermal Resistance, UNI Ente Nazionale Italiano di Unificazione, Milano (I), 2012.

[21] S. E. Gustafsson, Transient plane source techniques for thermal conductivity and thermal diffusivity measurements of solid materials, *Rev. Sci. Instrum.* 62 (1991) 797-804.

## 4. Ice-templating of geopolymers

### 4.1 Introduction

The production process of geopolymers, in aqueous medium, allows to tailor the porosity; water content in the starting mixtures affects the intrinsic mesoporosity of the geopolymer matrix, since water acts as pore former during the polycondensation stage [1], as mentioned in paragraph 2.6. Furthermore, the aqueous geopolymer mixture enables to use the ice-templating technique to achieve a lamellar macroporosity in the final consolidated materials.

Freeze-casting technique (or ice-templating when water is chosen as liquid medium) belongs to the sacrificial template method, used to produce porous materials widely described in paragraph 2.7.1.1. In this Thesis, ice-templating is used with geopolymers to induce the formation of unidirectional oriented channel like pores, to add an ultra-macroporosity to the intrinsic mesoporosity of the geopolymer matrix. This technique is particularly interesting for the peculiar structures and properties showed by ceramic porous freeze-cast materials, that allow to use geopolymers for new applications. For example, unidirectional porosity induces an higher permeability useful in the filter and catalysis field; furthermore, unidirectional porous constructs are potentially good thermal insulators [2].

Although the literature reports ice-templating of colloidal inert ceramic suspensions, the novelty of the present study is to apply the technique to a water-based sol-gel system able to produce metakaolin-based geopolymers, without the aid of dispersants or binders [3-4]. The main issue is to promote the simultaneous formation of geopolymer intrinsic mesoporosity and lamellar macroporosity by unidirectional ice growth together with a final chemical consolidation, avoiding any high temperature thermal treatment.

From the literature is known that several parameters influence the formation of the final material porosity [5]. Parameters affecting the final structure can be found in different stages of the ice-templating process and, in particular, in the formulation and preparation of the slurry (including the characteristic of the starting raw powders) and in the subsequent freezing, solidification stage, specific and related to the ice-templating process. In general, the formulation of the slurry must be

optimized to avoid segregation problems, furthermore, the viscosity of the liquid, the solid loading, the powders particle size and the use of additives, able to modify the viscosity, surface tension and the supercooling effects, are parameters to be taken into account [5-8]. Solidification conditions and kinetics (freezing temperature, freezing rate, freezing time) have a dramatic influence on the final microstructure of directional freeze casting [5, 9]. Indeed, the imposition of a defined temperature gradient forces the growth of the ice crystals along the same, while an increase of the freezing kinetics determines an increase of the solidification front speed, with consequent formation of a finer lamellar microstructure [10].

The parameters found to influence the samples produced in this work are summarized in figure 4.1 and mainly depend on the formulation and synthesis of the starting slurries. There is not a direct influence of the powder particle size, because the same metakaolin is used for all the slurries, but rather on the dimension of the geopolymerized particles obtained after the maturation step applied to the mixtures before the ice-templating process.

Similarly, the freeze dryer used for the ice-templating process not allows the control of the freezing rate in time. The instrument allows to set up the negative temperature of the freeze dryer shaft, but the solidification conditions depend on the temperature gradient established in the mold from the bottom part, in contact with the cold substrate, to the top. The temperature gradient, in turn, depends on the starting slurries, the interaction between particles, the dilution and possible segregation problems that determine the de-mixing of the cast mixtures. These multiple parameters, that can be interdependent, dictate the ordering and the structural properties of the final materials. In this work a systematic study of these parameters is done and emphasis is given on the influence of these parameters on the mesoporosity and macroporosity obtained in the final ice-templated samples, in order to identify a defined procedure usable on a scale-up process, to obtain reproducible samples.

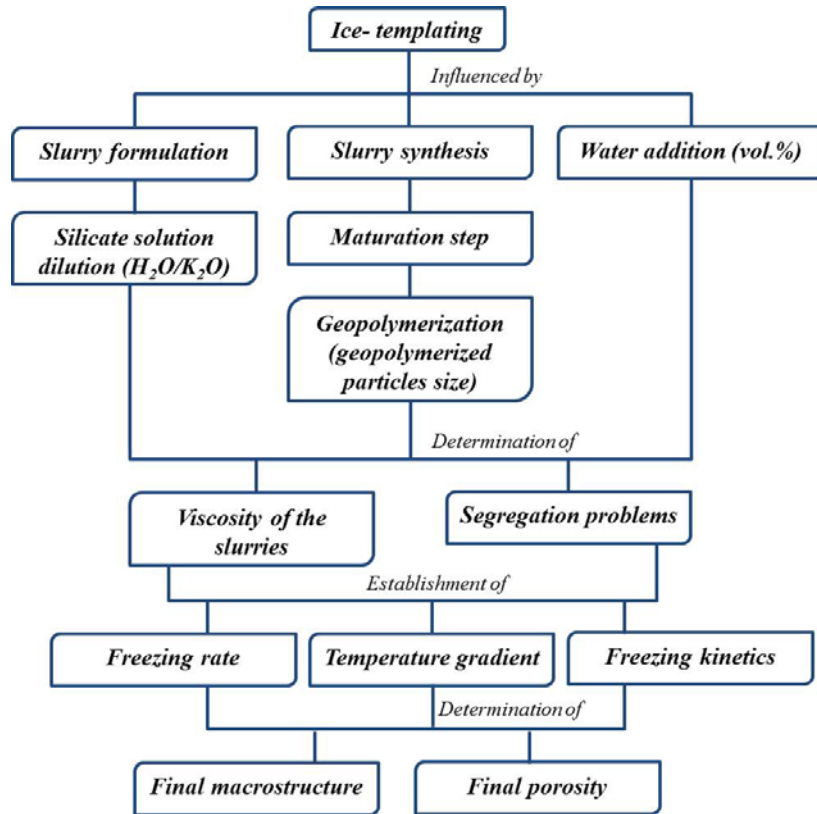


**Figure 4.1** Studied parameters that influence the ice-templating process and the final ice-templated materials porosity.

Starting from a geopolymer mixture of metakaolin and potassium silicate aqueous solution [1], geopolymerization is triggered through a maturation step, without to reach a complete consolidation. Then, different amounts of water are mixed to the geopolymer paste for ice templating and the chemical consolidation proceeds during freeze casting and drying.

First, the effect of different water amounts (20, 50, 70 vol.%), added for the ice-templating to a geopolymer starting mixture with dilution  $H_2O/K_2O=13.5$ , is studied preparing samples with 15 mm diameter and 10 mm height.

The quantity of water that produced the most promising properties is selected to produce lamellar monoliths. Also a more diluted geopolymer starting mixture with  $H_2O/K_2O = 23.0$  is used for the production of freeze-cast monoliths. Different monoliths are obtained changing the amount of water (30, 50 vol.%) added for the ice-templating and the maturation step applied to the starting slurry.

The ice-templated samples are widely characterized in term of macro- and micro-structure, intrinsic and induced lamellar porosity, chemical composition and the

development of the internal lamellar structure is observed by scanning micro-computed tomography ( $\mu$ -CT).

The overall process of ice-templating, studied on small geopolymer monoliths, is used to produce big samples, with increasingly diameter and height up to 5 cm and 7 cm respectively, to verify the feasibility and reproducibility of the lamellar pore structure on the scale-up process.

## **4.2 Samples preparation**

The initial starting mixtures are prepared using metakaolin M1200S as starting powder and activating alkali potassium silicate aqueous solutions. Two potassium silicate solutions with a molar ratio  $\text{SiO}_2:\text{K}_2\text{O} = 2.0$  and  $\text{H}_2\text{O}:\text{K}_2\text{O} = 13.5$  and  $23.0$  are used (see chapter 3 for compositions and procedures). The two slurries (coded G13 and G23), with a theoretical Si/Al molar ratio equal to 2.0, are prepared by the mechanical mixing of metakaolin and the potassium di-silicate solution for 20 min at 100 r.p.m.

After preparation, the slurries undergo different maturation step, reported in detail in the following paragraphs, to favor the geopolymerization without to reach a complete consolidation of the material. Deionized water, in different volume %, is added to the slurries and mechanically mixed for 8 min to induce the lamellar macroporosity during the ice-templating process. The mixtures are cast in cylindrical rubber molds, pre-cooled on the freeze dryer shaft set at  $-40^\circ\text{C}$  (Edwards Mod.MFD01, Crawley, UK).

The slurries cast in the molds are frozen at  $-40^\circ\text{C}$  and the solidified phase is sublimated in the freeze dryer in 24 h under a pressure of 10 Pa. After demolding, samples are rinsed in deionized water to remove any residues of unreacted potassium silicate and then dried in a heater at  $100^\circ\text{C}$ . The general scheme of the production process of the freeze-cast geopolymers is reported in figure 4.2.

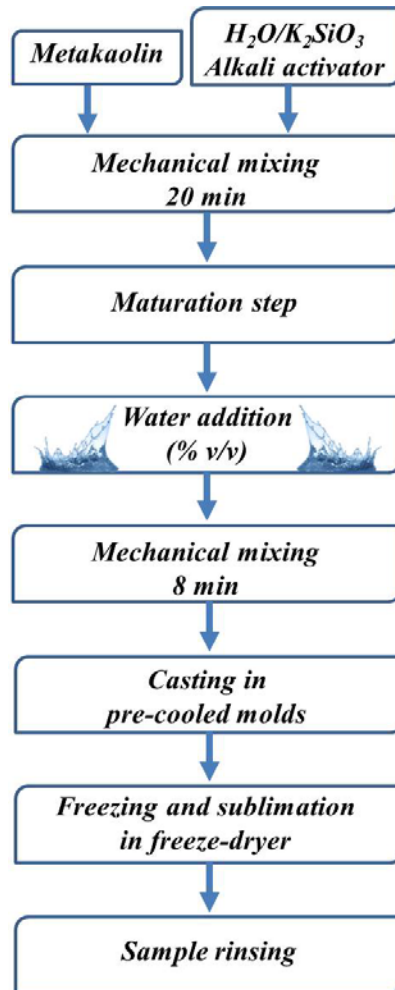


**Figure 4.2** Scheme of the ice-templating of geopolymers.

### 4.3 Effect of water addition on slurry G13

First, the effect of the water amount, added for ice-templating, is studied on the slurry G13. Deionized water in different percentages (20, 50 and 70 vol.%) is added to slurry G13 after a maturation step of 4 h at room temperature (r.t.) (treatment code T1). This preliminary study is made on samples with 15 mm diameter and 10 mm height.

A reference geopolymer, coded G13 (Table 4.1), is prepared by casting the slurry into plastic cylindrical mold and applying a curing of 24 h at r. t. and 24 h at 80 °C in a heater, allowing to obtain a fully geopolymerized material [1].

The sample codes, the compositions and the maturation step applied are listed in Table 4.1. The water addition is reported as vol.% over the theoretical volume of the geopolymer solid matrix plus the added water, while the solid loadings refer to

the wt.% of the metakaolin in the starting slurries.

The produced samples are deeply investigated to understand how the water amount in the starting mixture can affect the development of the porosity in the material. The intrinsic porosity of the geopolymer and the lamellar porosity, induced by the ice-templating process, are examined as well as the micro- and the macrostructure of the freeze-cast samples. From this preliminary screening the best mixture is selected for the production of monoliths ( $\varnothing = 15$  mm, height = 25 mm) that are investigated by micro computed tomography ( $\mu$ -CT) to assess the internal development of the lamellar porosity.

**Table 4.1** Sample code, compositions and maturation step of the reference geopolymer and of the freeze-cast geopolymers.

Sample code	K silicate dilution, H <sub>2</sub> O/K <sub>2</sub> O	Additional H <sub>2</sub> O for freeze casting (vol.%)	Solid loading (wt.%)	Maturation step
G13	13.5	-	63	24h r.t.+24h 80°C
G13-20	13.5	20	53	4h r.t.
G13-50	13.5	50	36	4h r.t.
G13-70	13.5	70	23	4h r.t.

#### 4.3.1 Macro- and microstructures of the ice-templated G13 geopolymers

Freeze-cast geopolymers show different macro- and microstructures depending on the amount of additional water used for the ice-templating process. The macrostructure of the samples may be observed in the high resolution photos of the top surfaces and of the cross sections reported in figure 4.3. Samples added with the 20, 50 and 70 vol.% of water develop a non-unidirectional lamellar structure. The water amount of the starting mixture plays an important role during the lamellae formation [10], because the ice-templating process consists in a segregation-induced templating of a second phase (in the present case, the newly formed geopolymer particles) by a solidifying liquid medium (water) that is subsequently removed by sublimation [11]. In the sample G13-20 the lamellar macrostructure is completely lost (Fig. 4.3a, d) because of the highest solid loading and the lowest volume of water available for ice-templating (Table 4.1). The low amount of water speeds the freezing rate [10] and geopolymer particles remain entrapped between the growing ice-crystals not able to develop in a lamellar way.

In sample G13-50 (Fig. 4.3b) and G13-70 (Fig. 4.3c) lamellae and channels are observed on the top surface, but the orientation of the lamellae over the cross section is tilted in the sample G13-50 (Fig. 4.3e) and completely random in the sample G13-70 (Fig. 4.3f). Moreover, sample G13-70 is brittle and difficult to handle, having the lowest solid loading (Table 4.1).

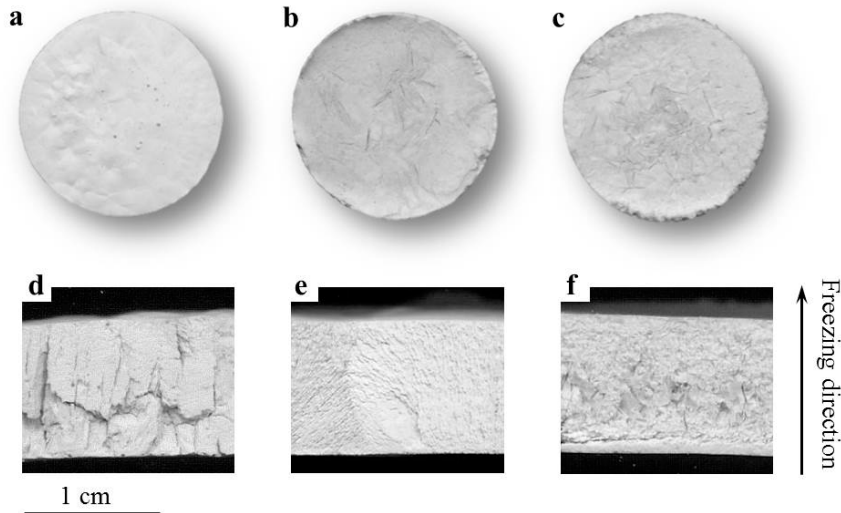


**Figure 4.3** Top surfaces (a, b, c) and longitudinal cross sections (d, e, f) of samples G13-20 (a, d), G13-50 (b, e) and G13-70 (c, f) [3].

The microstructure of the samples was investigated by SEM analysis. In figure 4.4 the SEM micrographs of the fracture surfaces are displayed; for all the samples the typical geopolymer precipitates are present [1] together with some characteristic features deriving from the ice-templating process [11].

Even though lamellae are not formed in the sample G13-20, as shown in figure 4.3d, a dendritic pattern is evidenced on the fracture surface (Fig. 4.4a, b). A finer dendritic pattern is observed in the microstructure of G13-50 (Fig. 4.4c, d), where lamellae are present on the top surface and within the sample (Fig. 4.3b, e). The micrographs of sample G13-70 (Fig. 4.4e, f) show a lamellae surface that exhibits a particular topography with jagged dendritic-like features, running in the solidification direction. Cracks are found on the lamellae surface as a further confirmation of the weakness of sample G13-70.

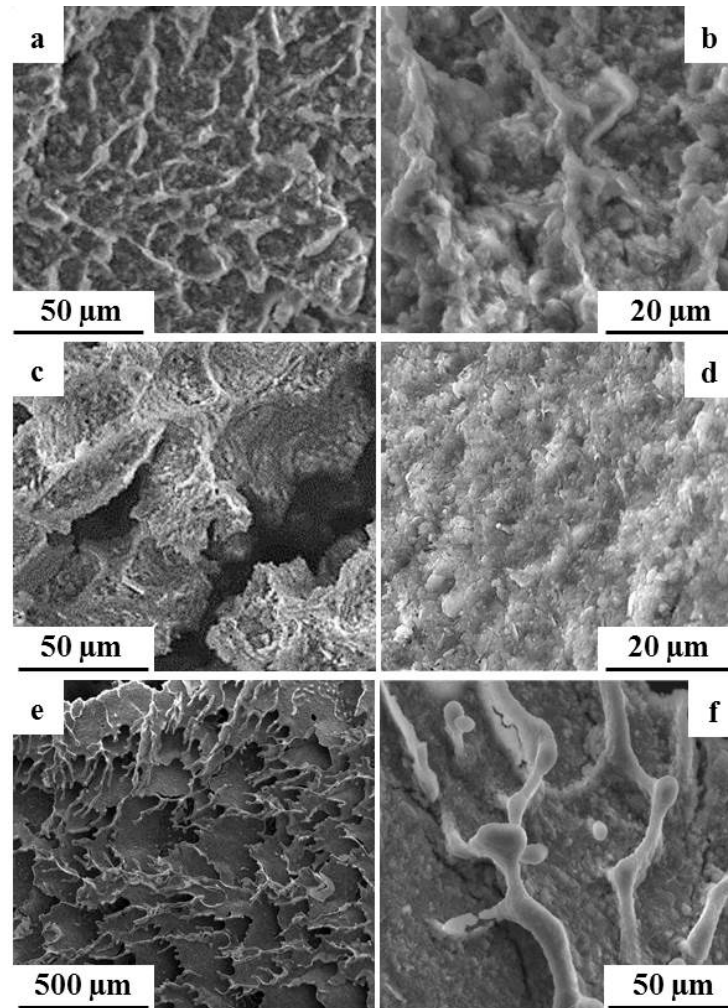


**Figure 4.4** SEM micrographs of the fracture surfaces of the samples G13-20 (a, b), G13-50 (c, d); lamellae surface of samples G13-70 (e, f) [3].

### 4.3.2 Intrinsic and induced porosity of the freeze-cast geopolymers

The total porosity of the samples (calculated by equation (1) reported in chapter 3) is reported in Table 4.2; it increases with the increase of the water amount used for the ice-templating process. The pore size distributions, obtained by mercury intrusion porosimetry (MIP), of the reference and freeze-cast geopolymers are reported in figure 4.5.

The results mainly concern the intrinsic porosity of the geopolymer matrix and partially the smallest macropores due to ice-templating. Pores ranging from 0.0058 to 1  $\mu\text{m}$  are related to the intrinsic porosity of the matrix, in fact water does not enter into the geopolymer framework [12] and acts as a pore forming agent when it is removed during the consolidation step [13-14]. In the pore size distributions of the freeze-cast samples, pores in the range from 1 to 100  $\mu\text{m}$  are

also detected, owing to the ice-templating process since they are not present in the reference material G13.

The total pore volume (Table 4.2) and average pore diameter (Fig. 4.5) increase with the increase of the water added for the ice-templating. The pore size distribution of the reference G13 sample is monomodal and located in the range 10-40 nm (Fig. 4.5a). Conversely, the pore size distribution of sample G13-20 is bimodal, with the main peaks detected at 10 nm and 400 nm (Fig. 4.5b). Sample G13-50 shows a pore size distribution still bimodal, but the contribution of macropores increases with a main peak at 20  $\mu\text{m}$ , even if pores of 10 nm are still detected. Sample G13-70, produced with a further increase of the water for ice-templating, presents a monomodal size distribution with the main peak located at higher macropore size (80  $\mu\text{m}$ ).

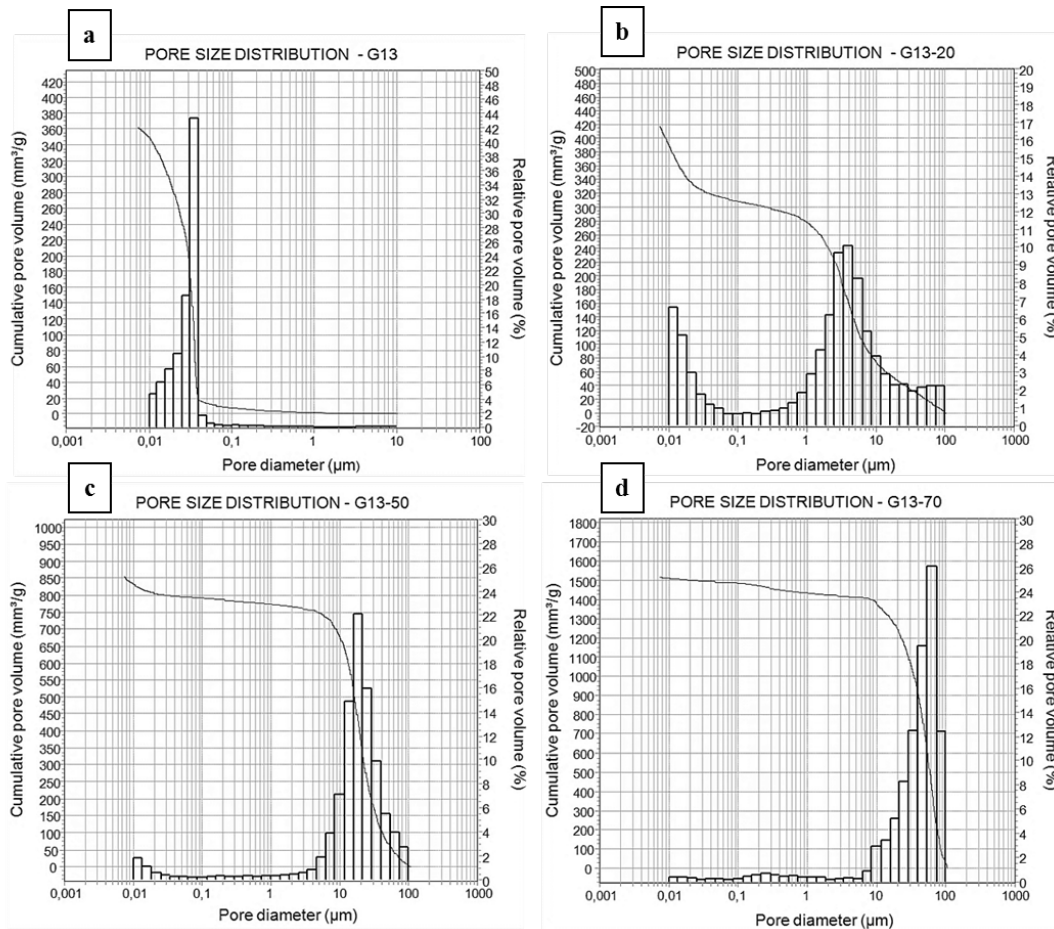


**Figure 4.5** Pore size distributions obtained by Hg intrusion porosimetry of the samples: a) G13, b) G13-20, c) G13-50 and d) G13-70 [3].

**Table 4.2** Bulk density ( $\rho$ ), total porosity ( $X_p$ ; by Hg porosimetry\*), total pore volume (by Hg porosimetry) and specific surface area (Ssa) and pore volume ( $V_p$ ) obtained by  $N_2$  adsorption/desorption measurements.

Sample	$\rho$ ( $g \cdot cm^{-3}$ )	$X_p$ (%)	Total pore volume ( $mm^3 g^{-1}$ )	Ssa ( $m^2 g^{-1}$ )	$V_p$ ( $cm^3 g^{-1}$ )
G13	-	43*	362	60.3	0.343
G13-20	1.1	53	418	46.0	0.147
G13-50	0.7	70	1404	39.4	0.115
G13-70	0.4	83	1516	4.5	0.014

The intrinsic porosity of the materials, that falls outside the Hg porosimetry detection range, was further investigated by  $N_2$  adsorption/desorption measurements to obtain complementary informations.  $N_2$  adsorption/desorption isotherms obtained for the reference G13 and the ice-templated samples are displayed in figure 4.6. The isotherms are characteristic of macroporous materials and classified as type II in the IUPAC classification [15]. All the samples show hysteresis loops, whose shape is slightly dependent on amount of added water. The reference G13 has a quite narrow hysteresis loop with almost parallel adsorption/desorption branches, the hysteresis terminates with a small plateau at high  $p/p^0$  values; however, it is a limit situation. Ice-templated materials have broadened loops and the presence of a plateau at high  $p/p^0$  values is not observed. The hysteresis may be considered as a mix of H2 and H3 (according to IUPAC classification [15]), which may be related to interparticle pores. The hysteresis loop shape depends on the amount of water, indeed the larger the additional water content for freeze casting the broader the loop in all the  $p/p^0$  range, in accordance with a greater delay in the completion of the geopolymerization reaction. The changes in the shape of the hysteresis loops suggest modifications of the number and dimension of pores during the freeze casting.

The pore size distributions obtained from the analysis are reported in figure 4.6b. The reference G13 has a broad pore distribution between 4 to 100 nm with maximum at about 13 nm. The contribution of pores with width in the range 20-100 nm is low, in agreement with the Hg porosimetry data. Ice-templated samples G13-20 and G13-50 have maximum of the pore size distribution plots at 7 and 5 nm respectively, while mesopores in sample G13-70 are almost absent. These results confirm that the consolidation of the material takes place during the freeze drying, leading to a densification and formation of smaller pores, the amount of

water determining the process.

Specific surface area ( $S_{sa}$ ) and pore volume values ( $V_p$ ), obtained by  $N_2$  adsorption/desorption analysis, reported in Table 4.2, result to be affected by the additional water used for the freeze-casting. The further water slows the completion of the geopolymerization; the consolidation, taking place during the freezing process, yields to a decrease in the surface area and pore volume of the geopolymer matrix, which is related to the water content.

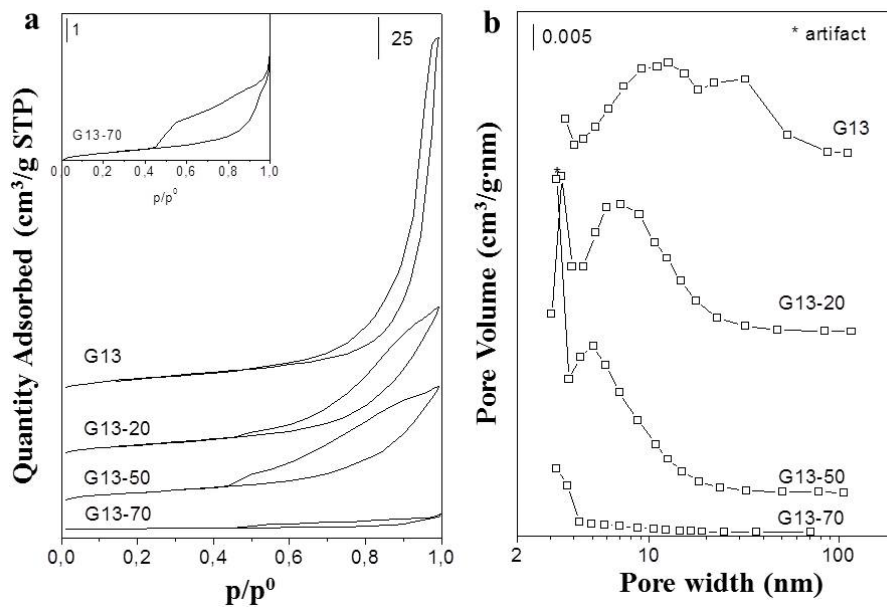


**Figure 4.6**  $N_2$  isotherms (a) and BJH pore size distributions (b) of reference G13 and ice-templated samples (G13-20, G13-50 and G13-70) [3].

#### 4.3.3 Chemical composition of the ice-templated samples (XRF analysis)

A preliminary investigation of the chemical composition of freeze-cast geopolymers was performed by X-Ray Fluorescence analysis (XRF) to determine the Si/Al and K/Al molar ratios in the final consolidated samples. The molar percentages of Si, Al and K and the molar ratios, in the reference material G13 and the freeze cast samples, are reported in Table 4.3.

While G13 exhibits almost the expected composition, i.e. molar ratios Si/Al=1.99 (nominal 2.00) and K/Al=0.80, the freeze-cast samples have lower molar ratios values. Sample G13-20 presents a Si/Al molar ratio equal to 1.62 and K/Al=0.35, sample G13-50 shows a Si/Al=1.87 and K/Al=0.36, while in the sample G13-70 a Si/Al=1.79 and a K/Al=0.35 are recorded.

**Table 4.3** Molar percentages of Si, Al and K and Si/Al and K/Al molar ratios of the reference material G13 and freeze cast G13-20, G13-50 and G13-70 samples determined by XRF.

Sample	Si mol%	Al mol%	K mol%	Si/Al	K/Al
G13	52.55	26.36	21.09	1.99	0.80
G13-20	54.61	33.72	11.67	1.62	0.35
G13-50	57.78	30.98	11.25	1.87	0.36
G13-70	56.91	31.84	11.26	1.79	0.35

The consolidated freeze-cast samples, after the washing and drying final step, register a weight loss of  $17 \pm 1\%$ , that may be hypothesized to depend on material and unreacted potassium silicate leakages, such as confirmed by XRF data, in which K and Si losses were registered. The composition of the salt removed by the rinsing treatment is different from the starting solution (containing potassium di-silicate  $K_2O \cdot 2SiO_2$ ), and may be roughly estimated as  $K_2O \cdot 1.6 SiO_2$  for G13-20,  $K_2O \cdot 0.6 SiO_2$  for G13-50 and  $K_2O \cdot 0.9 SiO_2$  for G13-70 sample, respectively. Potassium silicate solution is a polymer solution of silicate oligomers, stabilized by  $K_2O$  (i.e.  $KOH:H_2O$ ) [16]. Since the starting geopolymer mixture undergoes a maturation step to trigger the geopolymerization without a final consolidation, the contained potassium silicate aqueous solution continuously modifies its chemical composition during this step. The addition of the extra water, required for the ice-templating, dilutes the residual potassium silicate solution. During the freezing step at  $-40\text{ }^\circ\text{C}$ , the water starts to form ice crystals and leaves the remaining solution over-saturated in  $SiO_2$ , that afterwards polymerize into a gel [16,17]. In sample G13-20, the fast freezing, due to the low amount of water, may be supposed to quench the formation of large chains of silicate oligomers, that remain entrapped within the ice crystals and then washed away during the rinsing step. In the case of G13-50 and G13-70 samples, the main part of the polymerized (amorphous)  $SiO_2$  is segregated by the lamellar ice crystals and embedded in the geopolymer matrix, while the soluble  $K_2O$  is removed by water rinsing. This latter explains the discrepancy between the Si/Al and K/Al molar ratio values obtained for the ice-templated samples (Table 4.3), that may be related to both the amount of added water and the resulting freezing rates.

#### 4.4 Production and characterization of G13-50 monoliths

Based on the screening on the effect of the water amount added for ice-templating, an intermediate value of 50 vol.% of water results the most promising for the production of monoliths. The slurry of sample G13-50 was used to produce monoliths with a diameter of 15 mm and height of 25 mm. Highly reproducible lamellar monoliths were obtained from the ice-templating process (Fig. 4.7a). The top surface shows parallel lamellae grouped in domains of differently oriented planes (Fig. 4.7b, c). An image analysis of the top surface reveals that the average lamellae thickness is around 50  $\mu\text{m}$ , while the average interdistance between the lamellae is around 15  $\mu\text{m}$  (Fig. 4.7c).

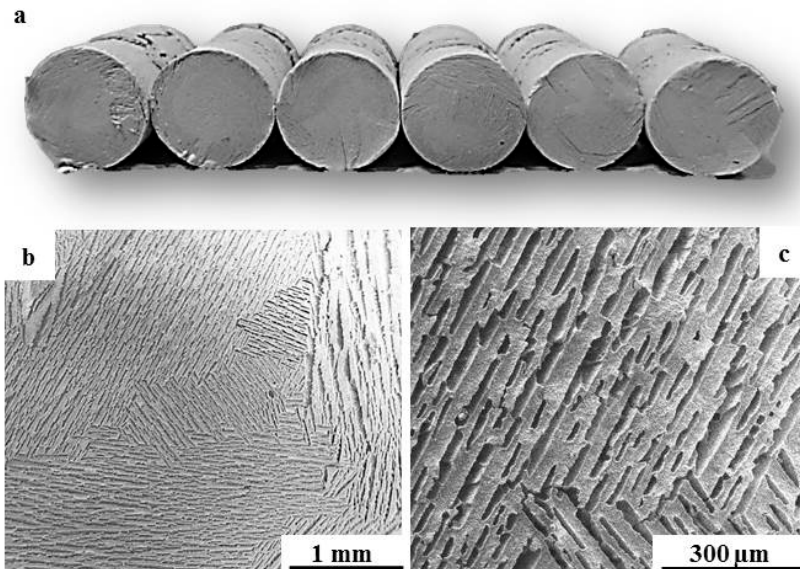


**Figure 4.7** G13-50 monoliths with 15 mm diameter and 25 mm height (a) and SEM micrographs of their lamellar top surface (c, d) [3].

##### 4.4.1 Analysis by $\mu$ -Computed Tomography of the G13-50 monolith

The lamellar 3-dimensional pore structure developed by monolith G13-50 was studied by  $\mu$ -CT. A 2D vertical slice from the middle of the monolith and 2D horizontal slices of three separate zones of the 25 mm high geopolymer monolith were obtained (Fig. 4.8). The images are virtual cross sections perpendicular and longitudinal to the lamellae growth direction. The production of the monoliths requires an increase of the mixture volume in the mold, that determines the decrease of the freezing rate. Consequently, a temperature gradient is created

within the mold promoting the unidirectional growth of the ice, observable in the vertical section of the monolith (Fig. 4.8). The vertical cross section can be divided into three zones:

Zone 1 – random pores may be seen close to the bottom, where the mold is in contact with the cold shaft of the freeze-dryer. The freezing rate in this zone is very fast and the supercooling degree is high, thus ice crystals have no time to orient massively and grow unidirectionally [10]. Geopolymer particles have not enough time to rearrange or redistribute by the diffusion mechanism [7], remaining engulfed in the ice crystals and forming a dense layer.

Zone 2 – the rate of the liquid front decreases and a lamellar morphology starts to appear, showing that the columnar ice front is rejecting the particles. Some lamellar ice crystals start to grow tilted toward the center, where the ice front crosses and forms a herringbone porous structure.

Zone 3 – a progressive lamellar ordering is present. Lamellae run toward the top of the sample, with an almost constant thickness.

This lamellae development is also observed in the 2D horizontal slices (Fig. 4.8a, b, c).

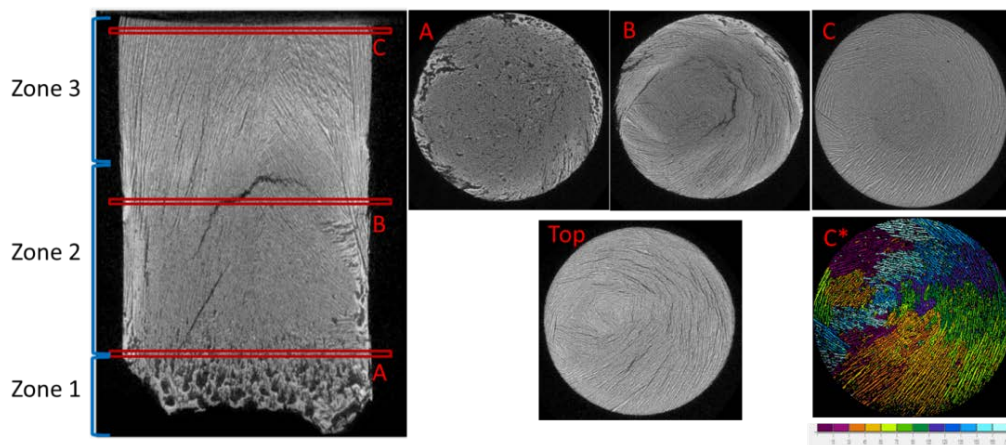


**Figure 4.8**  $\mu$ -CT slices of the G13-50 monolith: vertical cross section (the freezing direction is from the bottom-zone 1 toward the top-zone 3) and horizontal cross sections (A, B, C, Top). The color image C\* highlights the different orientations of the lamella domains [3].

Horizontal 2D slice A, taken from the part of the monolith closer to the base of the cold mold surface, shows that random pores coexist with some lamellar ones.

In the middle horizontal slice B, aligned lamellae and random pores are still found.

The last horizontal slice C evidences a well-defined lamellar microstructure, even more visible in the cylinder top horizontal slice.

Horizontal top slice shows that lamellae are arranged in domains kept over a great distance, giving rise to a spiral-like structure. An example of this different orientation of the lamella domains is showed in figure 4.8 C\*. The orientation of each domain may be related to the original nucleation conditions [7]. This random distribution attests that ice crystals do not grow only perpendicularly to the bottom of the mold, but also diagonally, due to different temperature gradients generated within the mold.

Vertical and horizontal cross sections evidence the presence of discontinuities in the monolith structure that might be voids or cracks. Discontinuities mainly run up to the boundaries between lamellar domains, so they may represent such boundaries or be also considered as ice-templating defects, such as ice-lenses [18].

$\mu$ -CT analysis enables an estimation of the homogeneity of the porosity developed during ice-templating by image analysis. The porosity percentage calculated in the bottom, middle, and top slices, excluding the largest pores that may be related to some cracks rather than to the freeze-casting, are 51, 48, and 48 %, respectively. The porosity values may differ from the results obtained by MIP, due to either the intrinsic spatial resolution of  $\mu$ -CT or the bottleneck effect of MIP [19]. From the porosity values obtained it may be stated that total porosity is rather constant along the cylinder. However, the porosity is modified along the cylinder in terms of morphology, shape, size, and distribution, as evidenced by the analysis of the vertical and horizontal cross sections.

#### **4.5 Effect of water addition and different maturation steps on slurry G23**

Samples were obtained following the general process formation scheme reported in figure 4.2, with some modification in the maturation step. After preparation, the slurry G23 underwent a maturation step at r.t. for 24 h (treatment code T2). Other

two maturation steps were tested on slurry G23: in the first one, after 24 h at r.t. the mixture was left for 1.5 h at 80 °C in a heater (treatment code T3); in the second one, after 24 h at r.t. the mixture was added with the water for the ice-templating and then treated for 2 h at 80 °C in a heater (treatment code T4).

Two different amount, 30 and 50 vol.%, of deionized water for the ice-templating process were added to the slurries. The mixtures were cast in cylindrical rubber molds for the production of monolith with 15 mm diameter and 25 mm height. Samples codes, compositions and the treatments applied are listed in Table 4.4. The water addition is reported as vol.% over the theoretical volume of the geopolymer solid matrix plus the added water. Solid loadings refer to the wt.% of the metakaolin in the starting slurries. At least five monoliths for each slurry were produced to check the reproducibility of the ice-templating process.

**Table 4.4** Sample code, compositions and maturation step of the freeze-cast geopolymer obtained from slurry G23.

Sample code	K silicate dilution, H <sub>2</sub> O/K <sub>2</sub> O	Solid loading (wt.%)	Maturation step	Additional H <sub>2</sub> O for freeze casting (vol.%)
G23-T2-30	23	35	T2: 24 h r.t.	30
G23-T2-50	23	27	T2: 24 h r.t.	50
G23-T3-30	23	35	T3: 24 h r.t. + 1.5 h 80 °C	30
G23-T3-50	23	27	T3: 24 h r.t. + 1.5 h 80 °C	50
G23-T4-30	23	35	T4: 24 h r.t. +H <sub>2</sub> O + 2 h 80 °C	30
G23-T4-50	23	27	T4: 24 h r.t. +H <sub>2</sub> O + 2 h 80 °C	50

#### 4.5.1 Macro-structure of the freeze-cast samples

From a first macrostructural screening on the consolidated samples, the freeze-cast samples obtained applying the maturation treatment T4 show the worst structural properties. The mixtures after the maturation step result highly viscous and difficult to cast, especially the mixture added with 30 vol.% of water. G23-T4-30 monoliths show a clear separation between the dense bottom of the sample and the lamellar zone (Fig. 4.9). The casting of the slurry requires longer time causing sedimentation problems and the disintegration of the samples after the rinsing treatment. For the mentioned reasons samples G23-T4-30 are not further characterized.

Conversely, the higher amount of water added for sample G23-T4-50 allows an adequate casting, despite the viscosity of the starting mixture. The consolidated samples do not show phase separation and are characterized together with the other samples obtained by treatments T2 and T3. Indeed, the monoliths obtained by the treatments T2 and T3 result compact and easy to handle (Fig. 4.9). All the monoliths present a denser zone of 3-4 mm thickness where the mixture is in contact with the cold surface of the mold, cooled by the freeze-dryer shaft set at -40 °C. In this zone the freezing rate is high and the particles remain engulfed in the ice crystals generating a dense layer [7]. Then the freezing rate decreases, moving towards the top of the sample, and unidirectional lamellar pores start to grow. Different structures and morphologies are obtained as a function of the maturation step applied and the water amount added for the ice-templating. The main differences are well evident in the photos of the top surface of the samples (Fig. 4.10), that will be used later to investigate, by image analysis, the macroporosity generated by the lamellar pores.



**Figure 4.9** Freeze-cast monoliths ( $\varnothing=15\text{mm}$ ,  $h=25\text{mm}$ ) obtained applying maturation step T2, T3 and T4 and adding 30 and 50 vol.% of water.

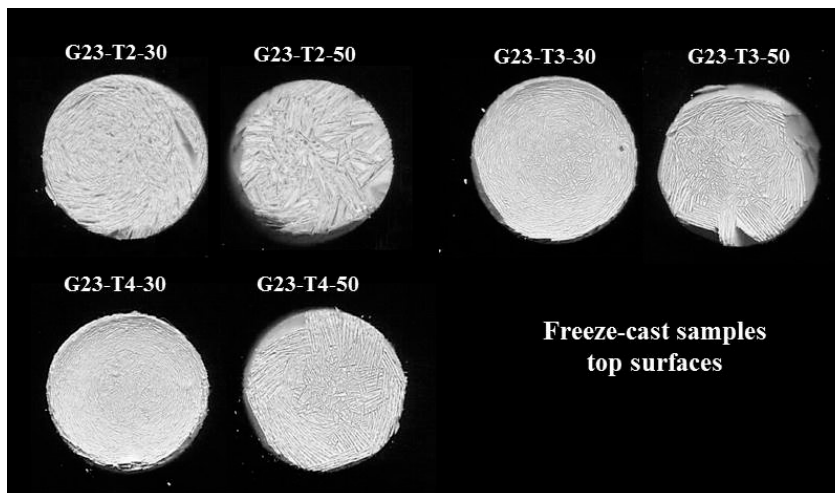


**Figure 4.10** Top surfaces of the freeze-cast monoliths ( $\varnothing=15\text{mm}$ ,  $h=25\text{mm}$ ) obtained applying the maturation steps T2, T3 and T4 and adding 30 and 50 vol.% of water.

#### 4.5.2 Rheology of the starting slurries

Viscosity is particularly important in freeze-casting, since for a given particle size it determines the critical freezing-front velocity at which particle trapping occurs inside the growing ice crystals [20].

The logarithmic plots of the viscosity versus shear rate of selected mixtures, obtained from slurry G13 and G23 added with 50 vol.% of water for ice-templating and subjected to different maturation treatments, are shown in figure 4.11. In the graphs the G13 and G23 mixtures are depicted before and after maturation steps and water addition for freeze casting. The sample code, the maturation applied to the slurry and the viscosity values at  $100 \text{ s}^{-1}$  are reported in Table 4.5. Geopolymer slurries exhibit a pseudo-plastic behavior and the viscosity is greatly dependent on the  $\text{H}_2\text{O}/\text{K}_2\text{O}$  molar ratio, equal to 13.5 for slurry G13 and 23.0 for slurry G23 [21]. Favier et al. [22] reported that colloidal interactions between metakaolin particles are negligible and hydrodynamic effects control the rheological behavior, namely the viscosity of the aqueous alkaline activator.

As shown in figure 4.11, after the first maturation step at r.t. the viscosities increase due to the ongoing geopolymerization process. The different maturation times at r.t., set at the beginning on a trial and error approach to favour the geopolymerization without a complete consolidation of the mixture, generate a viscosity of the same order of magnitude for the mixtures G13 and G23, regardless the different maturation time, 4 h (T1) and 24 h (T2) respectively.

Slurry G13 is less diluted and more viscous ( $5.06 \text{ Pa}\cdot\text{s}$ ) till the beginning, so 4 h at r.t. result enough to speed the geopolymerization reaction up, keeping the mixture suitable for the ice-templating process.

The higher dilution of the G23 slurry slows down the polycondensation process and 24 h at r.t. are required to increase the geopolymerization degree and the viscosity of the slurry, that changes from  $0.25$  to  $2.03 \text{ Pa}\cdot\text{s}$ .

Obviously, the water addition for ice templating decreases the viscosities, but the slurries G13-T1-50 and G23-T2-50 show again similar viscosities (Table 4.5).

After the thermal treatment T3 (1.5 h at  $80 \text{ }^\circ\text{C}$ ) on G23, the resulting paste showed a too high plasticity to be measured. It follows that after water addition the viscosity of G23-T3-50 is one order of magnitude higher than that of the slurries G13-T1-50 and G23-T2-50 (Table 4.5), being the curve very similar to that of

G23-T2 (Fig. 4.11b).

A relation between the viscosity of the slurry and the development of the lamellar morphology is confirmed in the characterizations of the freeze-cast samples reported below. Briefly, an increase of the slurry viscosity hampers the rejection of the particles by the ice front and increases the freezing rate.

**Table 4.5** Sample code, maturation step applied and viscosity at  $100 \text{ s}^{-1}$ .

Sample	Maturation step	Viscosity at $100 \text{ s}^{-1}$ (Pa·s)
G13	Freshly prepared	5.06
G13-T1	T1: 4 h r.t.	9.17
G13-T1-50	T1+50 vol.% H <sub>2</sub> O	0.02
G23	Freshly prepared	0.25
G23-T2	T2: 24 h r.t.	2.03
G23-T2-50	T2+50 vol.% H <sub>2</sub> O	0.01
G23-T3	T3: T2+1.5 h 80 °C	-
G23-T3-50	T3+50 vol.% H <sub>2</sub> O	0.75

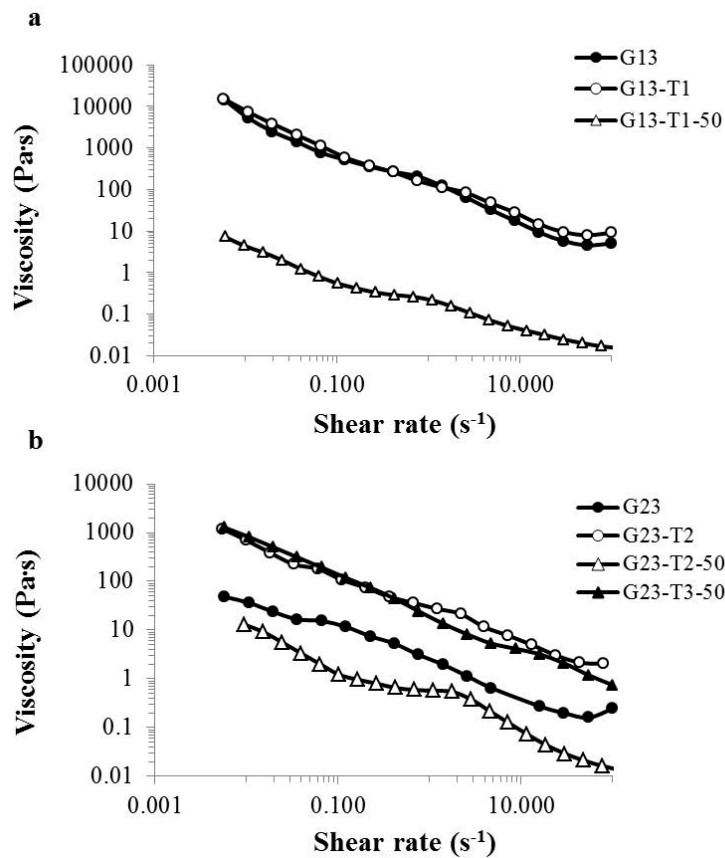


**Figure 4.11** Logarithmic plots of the viscosity versus the shear rate of the geopolymer slurries for both the compositions G13 (a) and G23 (b), before and after maturation/curing steps and water addition for freeze casting. The data error is  $\pm 5 \%$ .

### 4.5.3 Microstructure of the freeze-cast samples

ESEM micrographs were taken on the monoliths top surface to study the morphology of the lamellae at higher magnifications. SEM-FEG images of the lamellae surface were taken to study the microstructure of the geopolymer matrix. In general, the top surfaces of freeze cast samples show lamellae arranged in macro-domains, where the lamellae have the same orientation (Fig. 4.12). Within a single domain the lamellae are parallel. The dimensions of the macro-domains change among the different geopolymer samples, as well as the thickness and width of lamellae and pores (Fig. 4.12). At very low magnification, G23-T2-50 shows well developed wide pores and thicker lamellae in comparison to the other samples, where they are shorter, thinner and more randomly oriented. In particular, sample G23-T2-50 (Fig. 4.12c) shows a second order of arrangement of the lamellae, so that it appears as solid portion on macro-scale formed by very thin lamellae and pores parallel aligned. As shown in figure 4.12d a sort of lamellar micro-domains inside the macro-domains can be observed, differently from the other samples at the same magnification. Literature reports the formation of micro- and macrodomains with mutually miscible solvents, due to the growing of populations of crystals at different times [23-24]. In the same manner, a high dilution favors the de-mixing of potassium silicate solution with the water component enriched in soluble  $K_2O$ , that starts to crystallize into ice, and the remaining liquid portion over-saturated with respect to  $SiO_2$ . Thus, a locally variation of the  $K_2O/SiO_2$  ratio leads to different temperatures and rates of solidification.

Samples obtained by the treatment T3 show denser and less bridged lamellae, that in some cases present cracks on the surface (Fig. 4.12b, e).

The differences in the morphological characteristics of the monolith top surfaces (namely the lamellar pore width, that is the short axis of the pores cut perpendicular to the freezing direction [25], and lamella thickness) depend on the ice-crystals growth that may be related to the geopolymerization degree and therefore to the differences in the viscosity of the slurries. The lamellar pore width decreases by increasing the freezing rate [10, 26], that depends on the liquid amount. This effect is clear in monoliths with 30 vol.% of water; a higher solid loading (Table 4.4) increases the freezing rate and the pore width range decreases

(Fig. 4.12a, b). Conversely, samples with 50 vol.% present a bigger pore width range (Fig. 4.12c, e).

Furthermore, the viscosity of the starting slurry changes, depending on the type of maturation treatment used; the thermal treatment used for maturation step T3 increases the viscosity of the slurry, because the geopolymerization is sped up and the higher viscosity increases the freezing rate [20], resulting in a narrow lamellar pore width range.

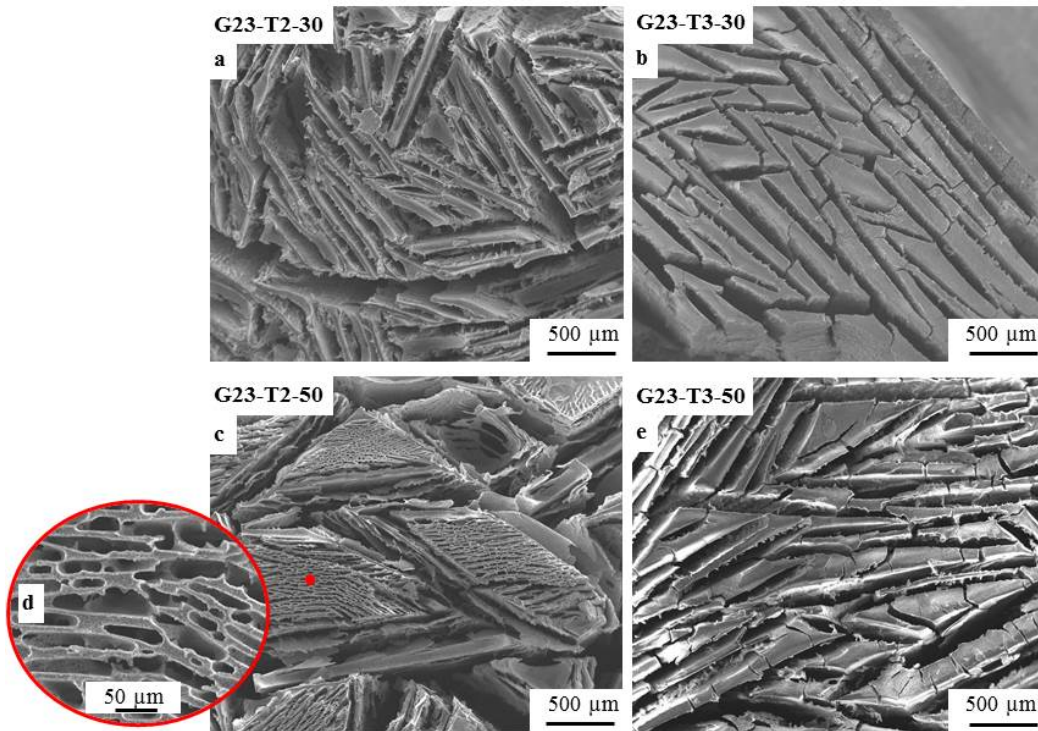


**Figure 4.12** ESEM micrographs of some monolith top surfaces a) G23-T2-30, b) G23-T3-30, c-d) G23-T2-50, and e) G23-T3-50.

Dendritic-like features, due to the ice-templating process, are observed for all the samples. In figure 4.13 the microstructures of the samples added with 50 vol.% of water are reported as representative examples. Some jagged dendrites, running in the solidification direction, are observed especially in the sample G23-T2-50 (Fig. 4.13a, b) and in some cases they form protuberances and bridges between adjacent lamellae. Some cracks are evident along the dendritic pattern of sample G23-T3-50 (Fig. 4.13c) as confirmation of the cracks observed on the lamellae in figure 4.12b and e.

Lamellae are built up by bounded geopolymer nanoparticles. Characteristic

geopolymer precipitates are found in all the freeze-cast microstructures reported in figure 4.14. These particles are more abundant, homogeneous in size and smoother in the samples obtained by the treatment T3, confirming a more homogeneous gelation process and a higher geopolymerization degree.

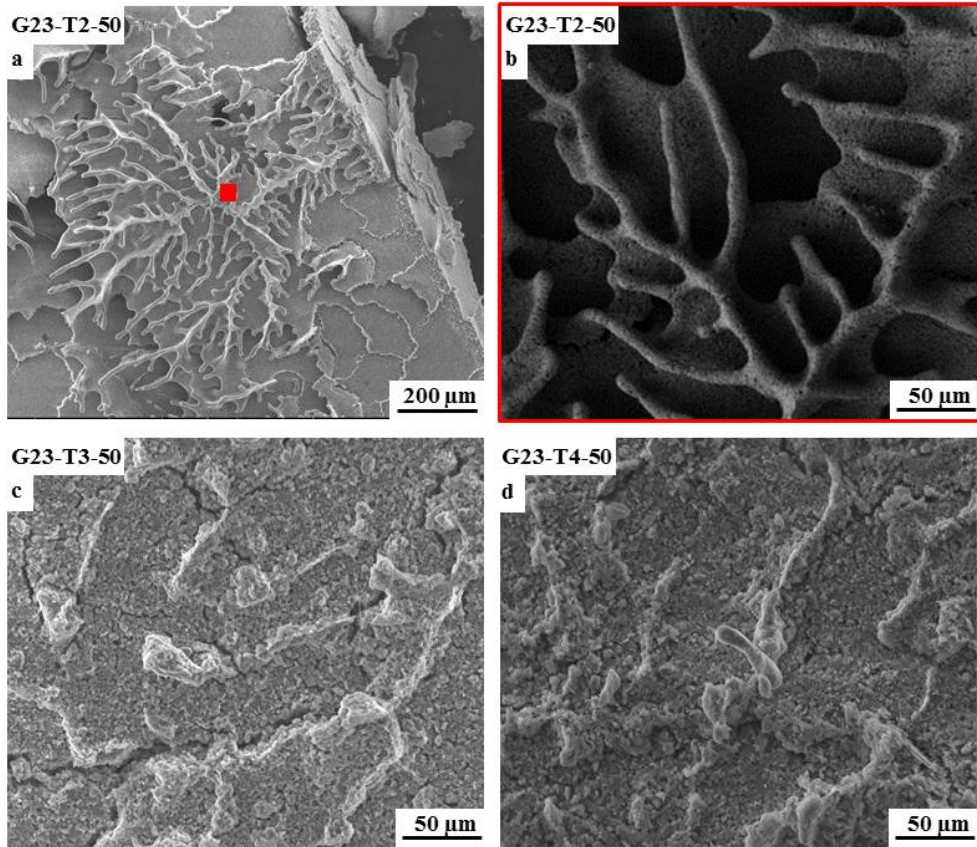


**Figure 4.13** Examples of dendritic-like patterns, due to the ice-templating process, found in the freeze-cast samples a-b) G23-T2-50, c) G23-T3-50 and d) G23-T4-50.

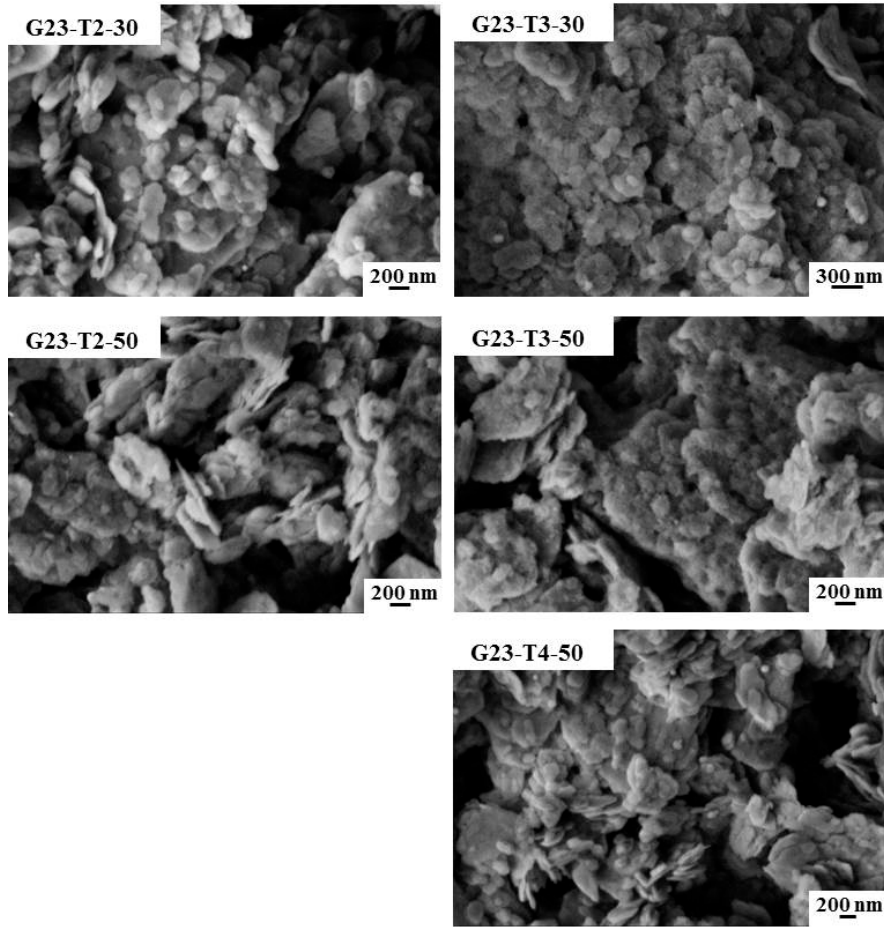


**Figure 4.14** SEM-FEG micrographs of the lamella microstructure in the freeze-cast samples, with evidences of geopolymer precipitates.

#### 4.5.4 Chemical composition (XRF analysis)

The chemical composition of ice-templated monoliths was studied by XRF. The silicon, aluminum and potassium molar percentages and the Si/Al and K/Al molar ratios are reported in Table 4.6. In a fully geopolymerized G23 matrix, Si/Al and K/Al molar ratios are theoretically equal to 2.00 and 0.80, respectively [1]. The calculated molar ratios, for the ice-templated monoliths, are much below the expected values. The water addition has an almost negligible effect, while the thermal treatment in the maturation steps T3 and T4 increases the Si/Al ratio. Treatment T4 causes a slight increase of the Si/Al value, probably because the addition of water before the thermal treatment slows down the geopolymerization process, making the thermal activation less effective. In the treatment T3, the maturation of the geopolymer matrix, not yet diluted with the water, was extended for 1.5 h at 80 °C. The Si-content slightly increases and the Si/Al ratio increases

up to  $\approx 1.6$  for both the samples. The maturation step T3 results the most effective to favor the geopolymerization process as confirmed by SEM-FEG micrographs, in which geopolymer precipitates are more abundant (Fig. 4.14). The lower K/Al ratio values depend on the continuous modification of the chemical composition of the potassium silicate aqueous solution during the geopolymerization (the maturation step), as reported before for the freeze-cast samples G13 (paragraph 4.3.3).  $K_2O$  aqueous solution starts to crystallize into the ice, during the freezing at  $-40\text{ }^\circ\text{C}$ , while  $SiO_2$  is either partially segregated by lamellar ice crystals or embedded into the geopolymer matrix, depending on the freezing rates. The soluble  $K_2O$  is then removed from the consolidated samples by the water rinsing treatment, leading to the low K/Al molar ratios measured.

**Table 4.6** Molar percentages of Si, Al, K, and Si/Al and K/Al molar ratios of the freeze cast samples measured by XRF.

Sample	Si mol%	Al mol%	K mol%	Si/Al	K/Al
G23-T2-30	53.80	36.65	9.55	1.45	0.26
G23-T2-50	54.18	36.19	9.63	1.50	0.27
G23-T3-30	54.60	34.17	11.23	1.60	0.33
G23-T3-50	55.43	33.45	11.12	1.66	0.33
G23-T4-50	54.51	35.91	9.57	1.52	0.27

#### 4.5.5 Analysis of the porosity

##### 4.5.5.1 Accessible porosity through Hg intrusion porosimetry and $N_2$ adsorption/desorption analysis

The pores in the geopolymer matrix constituting the lamellae, were evaluated by Hg intrusion and  $N_2$  adsorption/desorption analysis. Geopolymer matrix pores depend on modifications in the geopolymerization degree, that is influenced by the maturation treatment.

A trimodal pore size distribution (PSD) is obtained by Hg intrusion for all the samples (Fig. 4.15), with pores in 0.01-0.1, 0.1-10 and 10-100  $\mu\text{m}$  ranges. The shape of the PSD is not largely modified either by the water content or the maturation treatment. The accessible porosity percentages are reported in Table 4.7.

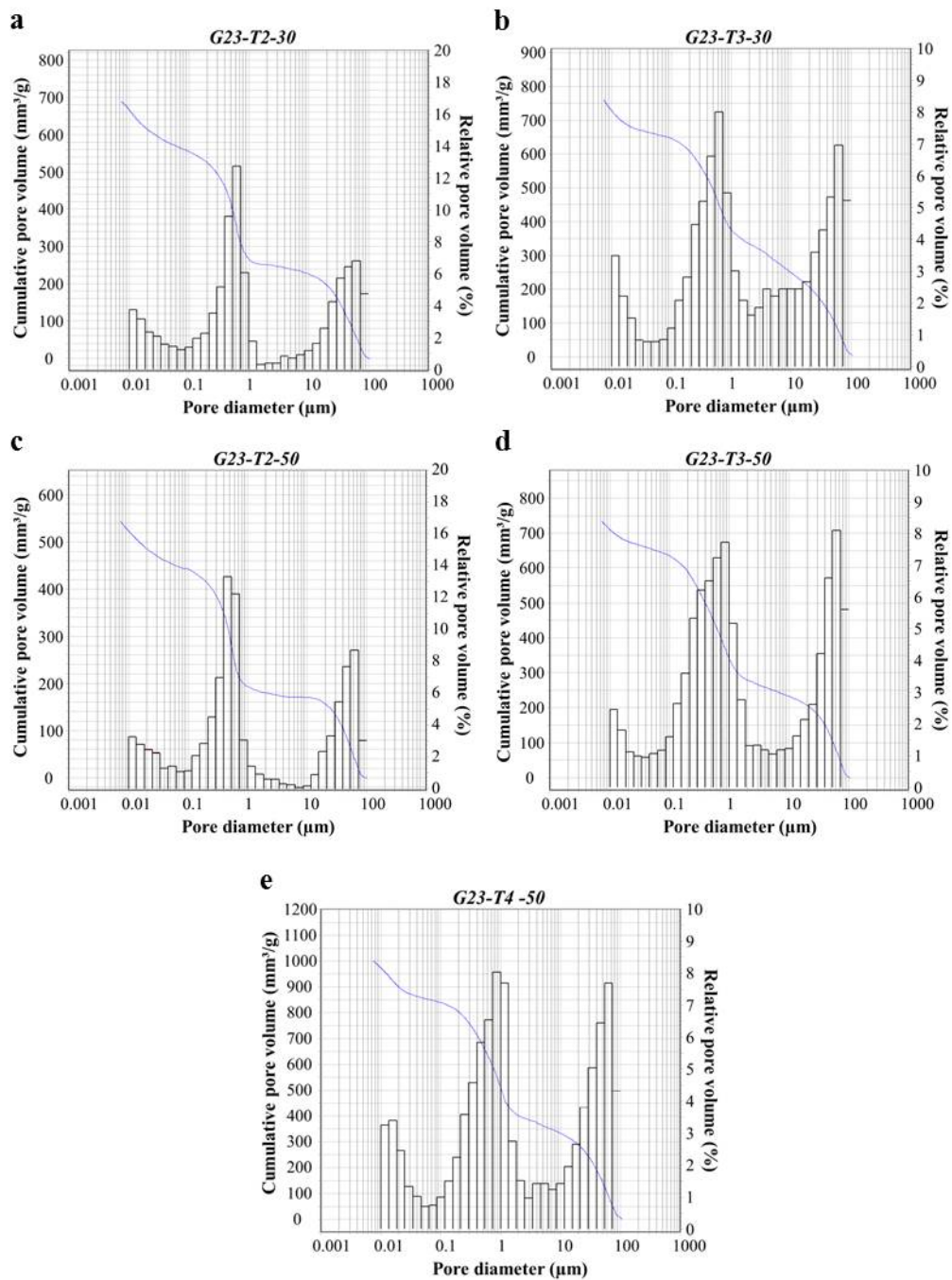


**Figure 4.15** Pore size distributions obtained by Hg intrusion porosimetry of the samples: a) G23-T2-30, b) G23-T3-30, c) G23-T2-50, d) G23-T3-50 and e) G23-T4-50.

**Table 4.7** Bulk density ( $\rho$ ), total porosity ( $X_p$ ), lamellar macroporosity of the freeze-cast samples. Accessible porosity obtained by Hg mercury intrusion and maximum frequency diameter ( $D_{maxf}$ ), specific surface area ( $S_{BET}$ ) and pore volume ( $V_p$ ) obtained by  $N_2$  adsorption/desorption analysis on freeze-cast samples.

Sample	$\rho$ ( $g \cdot cm^{-3}$ )	$X_p$ (%)	Accessible porosity (%)	Lamellar macroporosity (%)	$D_{maxf}$ (nm)	Ssa ( $m^2 \cdot g^{-1}$ )	$V_p$ ( $cm^3 \cdot g^{-1}$ )
G23-T2-30	0.9	61	54	7	9	38.1	0.144
G23-T2-50	0.7	69	42	27	7	33.4	0.123
G23-T3-30	0.9	62	60	2	6	38.6	0.121
G23-T3-50	0.7	70	54	16	5	35.8	0.112
G23-T4-50	0.8	67	60	7	10	21.0	0.098

The  $N_2$  adsorption/desorption isotherms are reported in figure 4.16a and b. The isotherms are classified as Type II according to IUPAC classification [15], characteristic of macroporous materials with no plateau at higher relative pressures, showing that increasing the relative pressure the volume adsorption continues [15]. The hysteresis loops attributed to the  $N_2$  capillary condensation into interconnected mesopores are a mixture of Types H2 and H3 [15]. Thus, the samples may be described as macroporous, with mesopores due to the aggregation of the geopolymer particles. The modifications in the shape of the hysteresis loop are related to changes in the pore size distribution.

The BJH pore size distributions, obtained from the analysis and reported in figure 4.16c and d, are monomodal in the 0.003-0.02  $\mu m$  range, with different maximum frequency diameter ( $D_{maxf}$ ) as a function of the sample (Table 4.7). Samples obtained from the same maturation treatment show a shift towards smaller pore sizes when an higher amount of water is used for the ice-templating (50 vol.%). Regarding the maturation treatment is evident that there is a decreasing of the average pore size in the following order  $T4 > T2 > T3$ . The modification of the geopolymerization degree due to the maturation step (and, consequently, the organization of the particles in the slurry) and to the freeze-casting may explain the pore size distributions within the lamellae and the values of specific surface area (Ssa) and pore volume reported in Table 4.7. The Ssa values, obtained by the BET method, result higher for the samples treated by the maturation step T3. The samples obtained from the same treatment show an increase of the BET surface area and the total pore volume when a lower water content is used (30 vol.%).

Samples obtained by the treatment T2 increase the surface area from 33.4 to 38.1  $\text{m}^2\cdot\text{g}^{-1}$  when 30 vol.% of water is used, while, in the same way, samples obtained by the treatment T3 increase the surface area from 35.8 to 38.6  $\text{m}^2\cdot\text{g}^{-1}$ .

From these results, the treatment T4 results less effective on the geopolymerization degree, having the lowest value of surface area ( $21.0 \text{ m}^2\cdot\text{g}^{-1}$ ) and total pore volume ( $0.098 \text{ cm}^3 \text{ g}^{-1}$ ) and the highest average pore size diameter (10 nm).

Lastly, it should be remarked that the data obtained by Hg intrusion and  $\text{N}_2$  gas adsorption mainly concern the geopolymer matrix mesoporosity. Hence, it may be stated that despite the macropores originated during freeze casting are largely modified, as previously observed in the sample macrostructures, the geopolymer pore network is only slightly modified by the water content and the treatment, suggesting that the formation of the particles is not largely changed during freeze-casting.

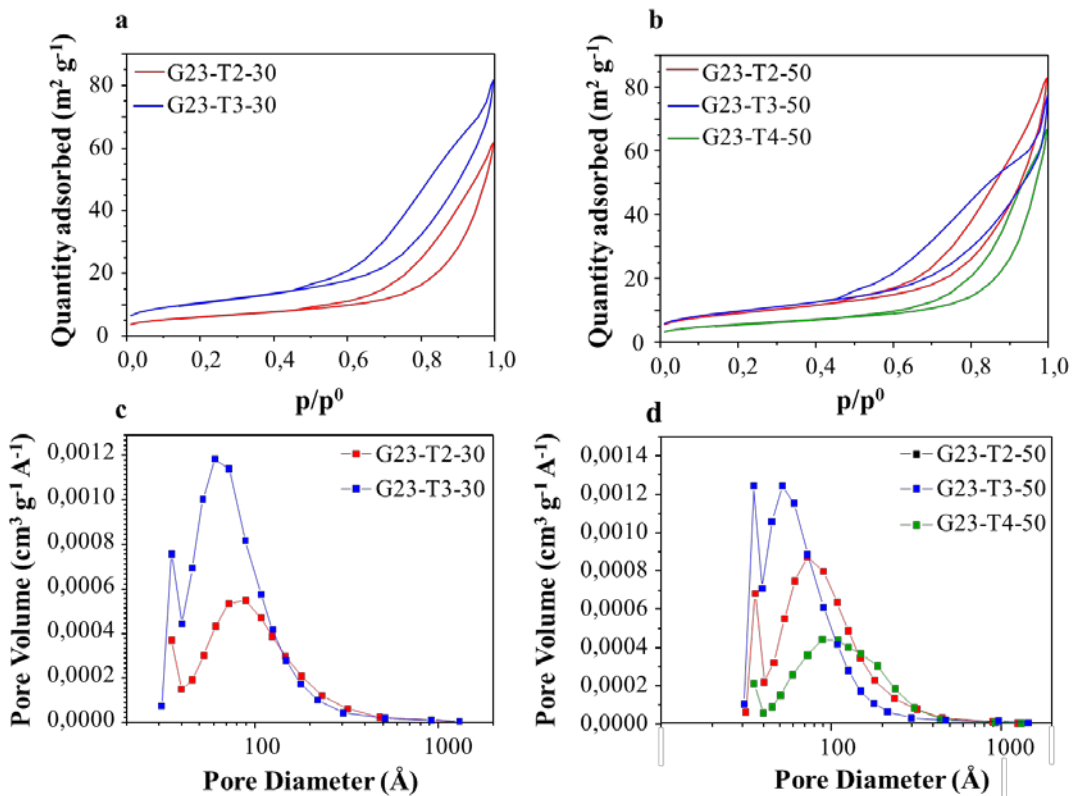


**Figure 4.16** a-b)  $\text{N}_2$  isotherms and c-d) BJH pore size distributions of some freeze-cast samples.

#### 4.5.5.2 Lamellar macroporosity

The macropores originated during freeze casting are largely modified by the water amount and the maturation step used, as highlighted in the high resolution images of the monoliths top surface (Fig. 4.10). From the values of total porosity and accessible porosity (Table 4.7) it is possible to calculate the percentages of macroporosity due to the macroscopic lamellar pores generated during the ice-templating process. As a general trend, the total porosity and the lamellar macroporosity increase with the increase of water amount, used for the ice-templating, and as the average bulk density of the monoliths decreases (Table 4.7). Fixed the added water amount (50 vol.%), the porosity is influenced by the maturation step. Since the total porosity is almost always  $\approx 70\%$ , the lamellar macroporosity follows the order  $G23-T2-50 > G23-T3-50 > G23-T4-50$ . As evidenced in the ESEM micrographs (Fig. 4.12), the treatment T2 results more effective in the lamellar pore formation.

An image analysis of the lamellar macro-porosity, developed on the horizontal top surface of the samples, was done exploiting the open source software Image J. A pore size distribution of lamellar pore length, correlated to the relative lamellar macroporosity percentage of the samples, is reported in figure 4.17. The range of pore length, pore width and lamella thickness, calculated from the analysis of at least 200 pores, are reported in Table 4.8.

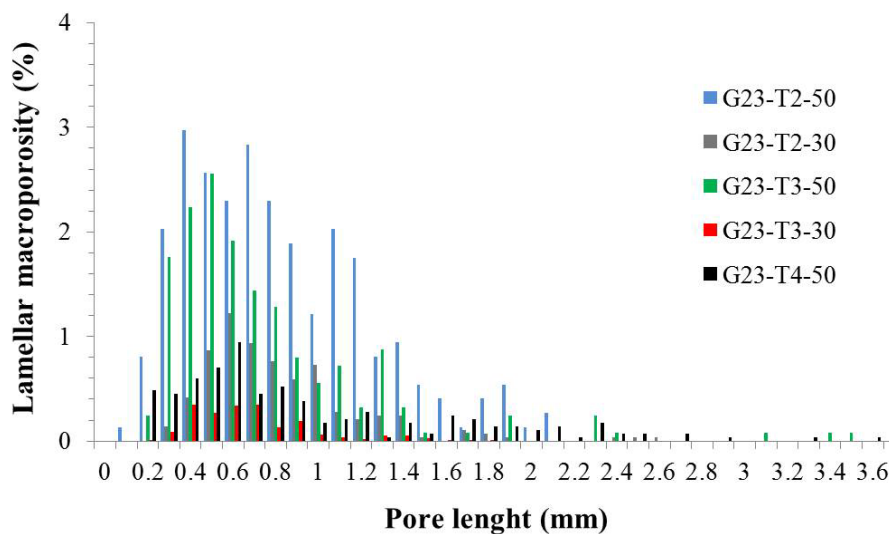


**Figure 4.17** Lamellar pore length distribution as a function of the relative lamellar macroporosity percentage calculated for each freeze-cast sample.

**Table 4.8** Pore length, pore width and lamella thickness ranges calculated by the image analysis of at least 200 pores developed on the horizontal top surface of the freeze-cast samples.

Sample	Pore length (mm)	Pore width (mm)	Lamella thickness (mm)
G23-T2-30	0.31-2.64	0.01-0.14	0.03-0.61
G23-T2-50	0.16-2.14	0.03-0.30	0.04-0.90
G23-T3-30	0.24-1.88	0.03-0.15	0.04-0.39
G23-T3-50	0.22-3.56	0.02-0.14	0.05-0.34
G23-T4-50	0.22-3.64	0.02-0.13	0.05-0.38

The pore length ranges are quite similar for all the samples, while the pore width and lamella thickness ranges are shorter for samples obtained by the treatments T3 and T4. As previously reported, an high viscosity of the starting slurries leads to the increase of the freezing rate, that generates thinner and less spaced lamellae.

The distributions (Fig. 4.17) result broader and with higher percentages of macropores in the case of the samples G23-T2-50 and G23-T3-50, because an higher amount of water favors the formation of lamellar pores.

The sample G23-T4-50 shows an intermediate behavior: lamellae result long, as in the sample G23-T2-50, in proximity of the mold, but thin and short, as in the samples G23-T3-30 and G23-T3-50, in the center. The viscosity of the slurry is probably comprised between the viscosities reached with the treatments T2 and T3 and the freezing rate developed affects the formation of the lamellae on the top surface.

#### **4.5.6 $\mu$ -Computed Tomography of the G23 ice-templated monoliths**

The evolution of the freezing in the vertical direction of the as prepared monoliths G23-T2 and G23-T3 with 30 and 50 vol.% H<sub>2</sub>O, was analyzed by the  $\mu$ -CT images as done before for the G13-50 monolith. Virtual slices of the monoliths, parallel and perpendicular to the ice growth direction, were investigated (Fig. 4.18). For the latter, cross sections in three different regions separated by 11 mm were analyzed. The structural gradient in the vertical cross section, characteristic of ice-templated samples [27], is observed in all of the prepared monoliths (Fig. 4.18). Three main zones are present also for the freeze-cast samples obtained from the slurry G23. As described in paragraph 4.4.1, a compact solid with small pores is developed in the bottom of the cylinder in contact with the cold mold (Zone 1).

The high cooling rate (super-cooled region) produces small ice crystals that engulf the geopolymer particles. Moving away from the bottom to the top, the temperature decreases and the growth behavior of the ice crystals changes to a steady-state; the crystals steadily align in the temperature gradient direction and the geopolymer particles are concentrated and assembled in lamellae (Zones 2 and 3). In the Zone 2, a mixture of rounded and lamellar pores coexists, while in Zone 3, better defined lamellar pores are developed. Thicker lamellae and larger pores, due to the decreasing of the solidification rate [28], are observed on the top of the cylinders as shown in the high resolution photos of the surface (Fig. 4.10). In the Zone 3, is evident as ice crystals do not grow only perpendicularly to the bottom of the mold, but also diagonally, due to different temperature gradients more remarkable near to the mold wall.

Beside these similarities, some differences in the length of the zones and the size and amount of the pores are identified among the different samples. The freezing dynamics, that affect the development of the porosity, depend on the amount of water and the maturation treatment, that influence the viscosity and the freezing rate. Furthermore, the addition of the water for the ice-templating, nevertheless the thoroughly mix, can lead to the de-mixing of the potassium silicate solution with some segregation problems inside the cast slurries. A water concentration gradient can be established along the mold, together with a relative temperature gradient. In general, the water concentration increases moving towards the top of the mold, where the higher dilution causes a lowering of the freezing rate with consequent formation of a more porous top surface.

The compact Zone 1 is larger in samples with low water content (30 vol.%) and with maturation treatment T3 (Fig. 4.18). The higher viscosity of the slurry hampers the rejection of the particles by the ice front. Moreover, an increase of the solid content lowers the thermodynamic solidification temperature by particle-particle interactions and the critical supercooling value for the ice formation is sooner reached [29].

The use of 30 vol.% of water associated with the treatment T3 (G23-T3-30) generates the sample with the most compact Zone 1. Horizontal slices A (Fig. 4.18) reveal that G23-T3-30 develops a random network of fine pores with not defined shape (at the resolution of the images), conversely to the other samples

that show the presence of some lamellar pores in the inner part of the cylinder where the freezing rate is slower.

In the horizontal slices B and C, pores of different width and length (representing the cross sections of the longitudinal channel-like pores) are arranged in domains. Some interconnected pores due to pore coalescence are also observed.

The use of a soft maturation treatment (T2) allows a better ordering of the ice crystals and, therefore, of the pores, mainly in the top slice and in the outer part of the cylinder, where the temperature is lower and the crystals have time to grow.

The use of the thermal treatment T3 leads to an increase of the viscosity in the starting mixture, that hampers the ordering of the lamellae in a long-range order; therefore the top surfaces show randomly distributed lamellae.

An estimation of the total porosity of each horizontal slice was obtained by the analysis of the reconstructed images (Table 4.9). It should be remarked that the obtained values differ from the total porosities previously calculated (Table 4.7) due to  $\mu$ -CT resolution.

The decrease in the water content and the use of the T3 treatment have similar effects on the porosity. The general trend is that a lower amount of added water (30 vol.%) generates lower porosity percentages in all the horizontal slices. For example, the total porosities calculated in slices A are 58 and 47 % for G23-T2-50 and G23-T3-50, decreasing to 40 and 20 % for the G23-T2-30 and G23-T3-30 (Table 4.9). Conversely, samples added with the same water amount show a decrease of the slice porosity, using the maturation treatment T3. For example, the total porosity in slices C is 65 % for sample G23-T2-50 and decreases to 51 % for sample G23-T3-50.

**Table 4.9** Estimation of the total porosity in the horizontal slices A, B and C, obtained by analysis of the reconstructed  $\mu$ -CT images.

Sample	Porosity slice A (%)	Porosity slice B (%)	Porosity slice C (%)
G23-T2-30	40	51	50
G23-T2-50	58	57	65
G23-T3-30	20	48	41
G23-T3-50	47	51	51

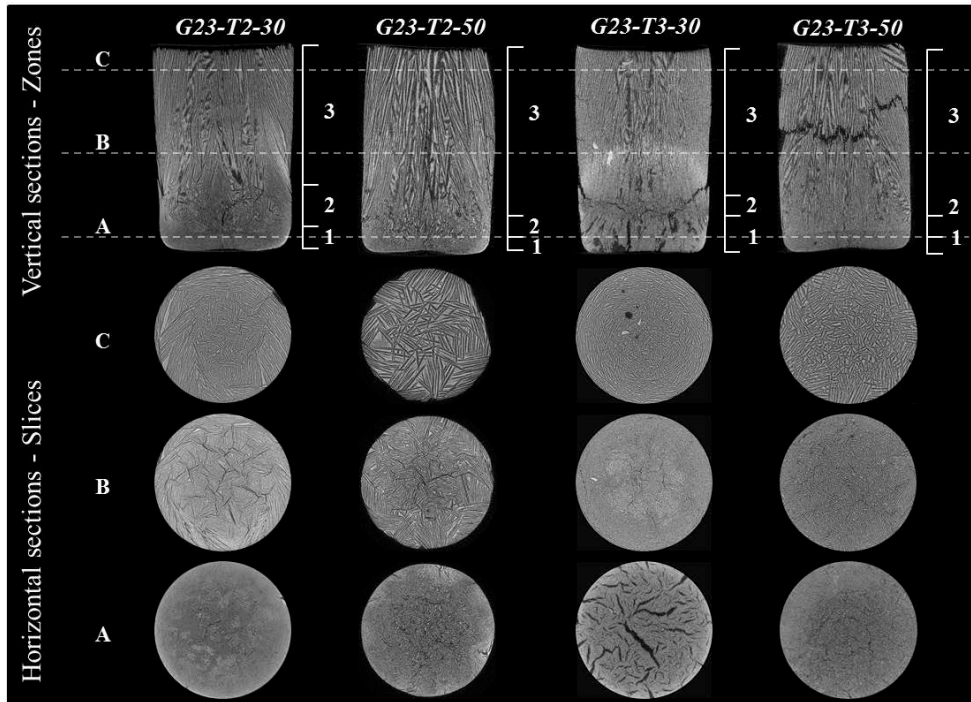


**Figure 4.18**  $\mu$ -CT slices of the ice-templated monoliths: vertical cross sections (the freezing direction is from the sample bottom (Zone 1) to the sample top (Zone 3) and horizontal cross sections (A, B, C).

#### 4.6 Scale-up on the freeze-cast G23-T2-50 sample preparation

The mixture G23-T2-50 is easy to cast and suitable for the overall ice-templating process; the monoliths obtained are structurally compact and good to handle, with a well-formed lamellar porosity developed along the cylinder, wide pores and thick lamellae on the top. Thus, this mixture was selected and used for the production of samples with increasing diameter and height and complex shapes.

In figure 4.19 the images of the samples obtained through a scale-up process are shown. The cylinder diameter is increased till 5.3 cm and the height till 7.0 cm. A freeze-cast geopolymer tile is obtained with a 15 cm side. A first compact zone of some millimeters, where the mold is in contact with the cold surface of the freeze dryer, is evident in all the samples. Then, the decrease of the freezing rate allows to the lamellae to grow unidirectionally oriented till the top of the samples. The increase of the mold height and the volume mixture cast, further decrease the freezing rate, generating long well-formed unidirectionally oriented lamellae and pores with bigger width, as evident in figure 4.19d.

In general, the mixture results suitable for the production of all samples and the differences found in the macrostructures are correlated to differences in thermal

gradients generated by the volume of the mixture used, the different height and diameter of the mold and the closeness to the walls of the silicon mold.

Complex shapes, with radial lamellar porosity, may be obtained imposing different thermal gradients inside the mold. A template of conductive metal is inserted inside the mold, as shown in figure 4.20, to stimulate the growing of the ice-crystals in a radial direction, from the internal metal template to the external silicon mold. Preliminary tests evidence as the radial lamellar porosity is obtained only in proximity of the metal template, highlighting as the thermal gradient, generated by the metal template, is not enough to stimulate a fast growth of the ice-crystals in a radial way on a long range order.

Although a further characterization has to be performed on the samples, this preliminary study highlights as the ice-templating technique is appropriate to obtain lamellar macroporous geopolymers, with different size ranges and complex shapes. The possibility to obtain this material type in different sizes and shapes opens good prospects for the use of geopolymers in different applications, such as for filtration and catalysis.

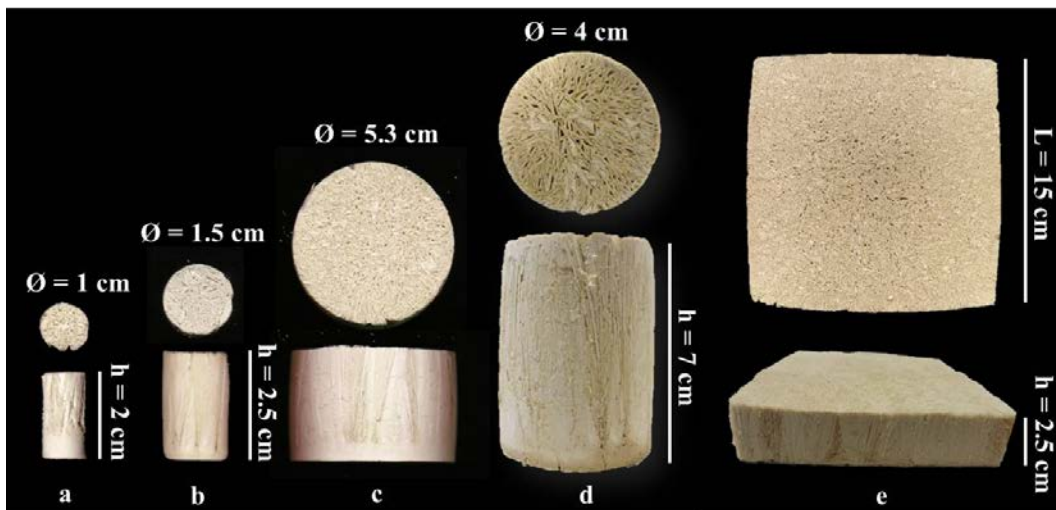


**Figure 4.19** Scale-up of sample G23-T2-50; freeze-cast samples obtained with increasing diameter and height (a, b, c, d). Freeze-cast geopolymer tile with 15 cm side (e) [30].

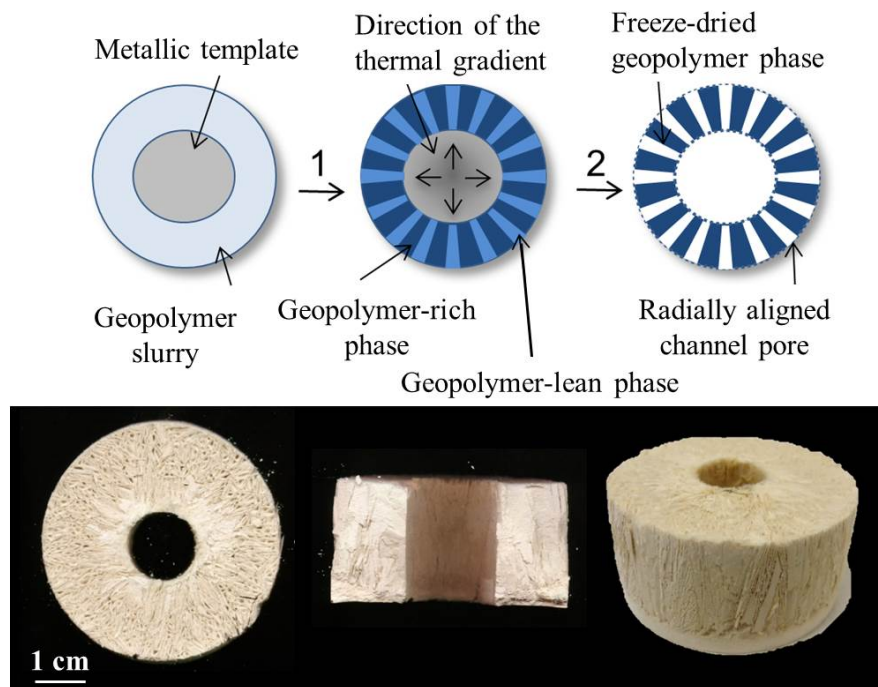


**Figure 4.20** Scheme of the production process of freeze-cast geopolymer, obtained inserting a metal template inside the mold to stimulate the formation of a radial lamellar porosity, and example of the produced sample [30].

#### 4.8 Conclusions

Unidirectional lamellar geopolymers can be synthesized by the ice-templating process, obtaining highly porous materials. Indeed, the technique was successfully applied on water-based reactive sol-gel system to produce metakaolin based geopolymers, despite the general use of the ice-templating with colloidal ceramic suspensions. The simultaneous formation of geopolymer intrinsic mesoporosity and lamellar macroporosity by unidirectional ice growth, together with a final chemical consolidation, were obtained by properly combining maturation steps of the geopolymer reactive system with additional water amounts for ice-templating. All the samples show the presence of geopolymer precipitates in their microstructures, confirming that ice-templating may be successfully combined with geopolymerization.

Several parameters result to influence the formation of the final samples as summarized in table 4.10. The dilution of the starting mixture affects the intrinsic mesoporosity of the geopolymer matrix; differences were found in the pore size

distribution when slurries G13 or G23 are used. Instead, the use of different maturation steps on slurry G23 slightly affects the development of the intrinsic mesoporosity of the geopolymer matrix. In general, the maturation treatment applied to the slurry slightly affects the formation of the pore network, suggesting that the formation of the particles does not largely change during the freeze-casting. However, the little modifications in the specific surface area, total pore volume and mean pore diameter values, obtained by N<sub>2</sub> adsorption/desorption analysis, reveal that a mild thermal treatment of the starting mixture (treatment T3) is most effective on the geopolymerization degree.

Conversely, the production of different ice-templated samples highlighted as the macrostructure is strongly affected by the height of the sample, the water amount targeted for ice-templating and the maturation step applied to the starting slurry.

Lamellar macroporosity increases by increasing the water used for the ice-templating. The morphology of the lamellar pores, the dimension, shape and development of the structure along the casting direction depend on the maturation step, that affects the viscosity of the starting slurry.

An evident correlation between the development of the macrostructure and the viscosity of the starting mixture was found. Viscous mixtures lead to the formation of randomly oriented short lamellae and small lamellar pore width, while thicker, longer and more spaced lamellae are obtained when the viscosity of the slurry decreases.

In particular, mild maturation steps at r.t. (T1 and T2) generate viscosities suitable to obtain well-formed lamellae along the casting direction of the monoliths and on the top surfaces. Samples obtained by the maturation treatment T3 show dense and short lamellae with evident cracks on the surface, while the maturation treatment T4 results the less adequate for the ice-templating process, because the difficulties encountered during the casting of the samples and the lack of properties in comparison to the other samples.

The final scale-up, of the overall process, highlighted as this technique can be adopted for the realization of big samples with an oriented lamellar macroporosity on long-range order, giving rise to materials that may be used as filters or catalytic supports.

**Table 4.10** Parameters investigated: what they affect and the effects on the final ice-templated samples.

Parameter	Affect	Effect
H <sub>2</sub> O/K <sub>2</sub> O	Geopolymerization	Higher with low dilution (H <sub>2</sub> O/K <sub>2</sub> O = 13.5) → higher Si/Al ratio and Ssa
	Mesoporosity	Pore size distribution positioned at higher values with high dilution (H <sub>2</sub> O/K <sub>2</sub> O = 23)
	Viscosity	Ice-templating process
Maturation step	Geopolymerization	Slightly affected → thermal treatment (T3) increases the formation of geopolymer precipitates → higher Ssa, Si/Al, pore volume
	Mesoporosity	
	Viscosity	Ice-templating → freezing rate → morphology of the lamellar pores High viscosity → randomly oriented short lamellae and small lamellar pore width Low viscosity → thicker, longer and more spaced lamellae
Additional H <sub>2</sub> O	Viscosity	Ice-templating → freezing rate → morphology of the lamellar pores
	Segregation	De-mixing of the slurry → ice-templating concentration gradient → thermal gradient → morphology of the lamellar pores
	Ice-templating	High water amount → high lamellar macroporosity
Mold geometry	Ice-templating	Different temperature gradient in the mold

## References

- [1] E. Landi, V. Medri, E. Papa, J. Dedecek, P. Klein, P. Benito, A. Vaccari, Alkali-bonded ceramics with hierarchical tailored porosity, *Appl. Clay Sci.* 73 (2013) 56-64.
- [2] K. Okada, T. Isobe, K. Katsumata, Y. Kameshima, A. Nakajima, K.J.D. MacKenzie, Porous ceramics mimicking nature-preparation and properties of microstructures with unidirectionally oriented pores, *Sci. Technol. Adv. Mater.* 12 (2011) 064701.
- [3] E. Papa, V. Medri, P. Benito, A. Vaccari, S. Bugani, J. Jaroszewicz, W.

- Swieszkowski, E. Landi, Synthesis of porous hierarchical geopolymer monoliths by ice-templating, *Micropor. Mesopor. Mater.* 215 (2015) 206-214.
- [4] E. Papa, V. Medri, P. Benito, A. Vaccari, S. Bugani, J. Jaroszewicz, E. Landi, Insights into the macroporosity of freeze-cast hierarchical geopolymers, *RSC Adv.* 6 (2016) 24635-24644.
- [5] W.L. Li, K. Lu, J.Y. Walz, Freeze casting of porous materials: review of critical factors in microstructure evolution, *Int. Mater. Rev.* 57 (2012) 37-60.
- [6] E. Munch, E. Saiz, A.P. Tomsia, S. Deville, Architectural control of freeze-cast ceramics through additives and templating, *J. Am. Ceram. Soc.* 92 (2009) 1534-1539.
- [7] S. Deville, E. Maire, A. Lasalle, A. Bogner, C. Gauthier, J. Leloup, C. Guizard, Influence of particle size on ice nucleation and growth during the ice-templating process, *J. Am. Ceram. Soc.* 93 (2010) 2507-2510.
- [8] S.W. Sofie, F. Dogan, Freeze casting of aqueous alumina slurries with glycerol, *J. Am. Ceram. Soc.* 84 (2001) 1459-1464.
- [9] M. Kochs, CH. Korber, B. Nunner, I. Heschel, The influence of the freezing process on vapour transport during sublimation in vacuum-freeze-drying, *Int. J. Heat. Mass Trans.* 34 (1991) 2395-2408.
- [10] S. Deville, E. Saiz, A.P. Tomsia, Ice-templated porous alumina structures, *Acta Mater.* 55 (2007) 1965-1974.
- [11] S. Deville, Freeze-Casting of Porous Ceramics: A Review of Current Achievements and Issues, *Adv. Eng. Materials* 10 (2008) 155-169.
- [12] J. Davidovits, Geopolymers Chemistry and Applications. Davidovits J. (Ed.). Institut Geopolymere, Saint-Quentin, France, 2008.
- [13] Z. Zuhua, Y. Xiao, Z. Huajun, C. Yue, Role of water in the synthesis of calcined kaolin-based geopolymer, *Appl. Clay Sci.* 43 (2009) 218-223.
- [14] K. Okada, A. Ooyama, T. Isobe, Y. Kameshima, A. Nakajima, K.J.D. MacKenzie, Water retention properties of porous geopolymers for use in cooling applications, *J. Eur. Ceram. Soc.* 29 (2009) 1917-1923.
- [15] K.S.W. Sing, D.H. Everett, R.A.W. Haul, L. Moscou, R.A. Pierotti, J. Rouquerol, T. Siemieniewska, Reporting physisorption data for gas/solid systems with special reference to the determination of surface area and porosity, *Pure Appl. Chem.* 57 (1985) 603-619.

- [16] J.D. Hunt, A. Kavner, E.A. Schauble, D. Snyder, C.E. Manning, Polymerization of aqueous silica in H<sub>2</sub>O–K<sub>2</sub>O solutions at 25–200 °C and 1 bar to 20 kbar, *Chem. Geology* 283 (2011) 161-170.
- [17] T.T. Trinh, A.P.J. Jansen, R.A. van Santen, E.J. Meijer, Role of water in silica oligomerization, *J. Phys. Chem. C* 113 (2009) 2647-2652.
- [18] A. Lasalle, C. Guizard, E. Maire, J. Adrien, S. Deville, Particle redistribution and structural defect development during ice templating, *Acta Mater.* 60 (2012) 4594-4603.
- [19] S. Bugani, M. Camaiti, L. Morselli, E. Van de Castele, K. Janssens, Investigation on porosity changes of Lecce stone due to conservation treatments by means of x-ray nano- and improved micro-computed tomography: preliminary results, *X-Ray Spectrom.* 36 (2007) 316-320.
- [20] U.G.K. Wegst, M. Schecter, A. E. Donius, P. M. Hunger, Biomaterials by freeze casting, *Philos. Trans. A* 368 (2010) 2099–2121.
- [21] V. Medri, E. Papa, J. Dedecek, P. Klein, P. Benito, A. Vaccari, E. Landi, Effect of metallic Si addition on polymerization degree of in situ foamed alkali-aluminosilicates, *Ceram. Intern.* 39 (2013) 7657-7668.
- [22] A. Favier, J. Hot, G. Habert, N. Roussel, J.B. d’Espinose de Lacaillerie, Flow properties of MK-based geopolymer pastes. A comparative study with standard Portland cement pastes, *Soft Mater.* 10 (2014) 1134–1141.
- [23] C. Guizard, J. Leloup, S. Deville, Crystal templating with mutually miscible solvents: a simple path to hierarchical porosity, *J. Am. Ceram. Soc.* 97 (2014) 2020-2023
- [24] Y. Tang, S. Qiu, C. Wu, Q. Miao, K. Zhao, Freeze cast fabrication of porous ceramics using tert-butyl alcohol-water crystals as template, *J. Eur. Ceram. Soc.* 36 (2016) 1513-1518
- [25] P. M. Hunger, A. E. Donius, U. G. K. Wegst, Structure–property-processing correlations in freeze-cast composite scaffolds, *Acta Biomater.* 9 (2013) 6338–6348.
- [26] E. Landi, D. Sciti, C. Melandri, V. Medri, Ice templating of ZrB<sub>2</sub> porous architectures, *J. Eur. Ceram. Soc.* 33 (2013) 1599-1607.
- [27] S. Deville, E. Maire, A. Lasalle, A. Bogner, C. Gauthier, J. Leloup, C. Guizard, In situ X-Ray radiography and tomography observations of the

solidification of aqueous alumina particles suspensions. Part II: steady state, *J. Am. Ceram. Soc.* 92 (2009) 2497-2503

[28] T. Waschkes, R. Oberacker, M. J. Hoffmann, Control of lamellae spacing during freeze casting of ceramics using double-side cooling as a novel processing route, *J. Am. Ceram. Soc.* 92 (2009) S79–S89.

[29] T. Waschkes, R. Oberacker, M. J. Hoffmann, Investigation of structure formation during freeze-casting from very slow to very fast solidification velocities, *Acta Materialia* 59 (2011) 5135–5145.

[30] E. Papa, V. Medri, P. Benito, A. Vaccari, E. Landi, Freeze casting of alkali bonded ceramics, oral presentation at the 14<sup>th</sup> International Conference of the European Ceramic Society, Toledo, Spain, June 2015.

## **5. Production of porous geopolymer wicks for a loop heat pipe (LHP) prototype**

### **5.1 Introduction**

#### **5.1.1 LHP description**

The loop heat pipe was for the first time developed and tested in the year 1972, as response to the increasing request of electronic systems, especially for the aerospace technology, that requires high operational reliability and robustness [1-4]. Loop heat pipes are 2-phase heat-transfer devices with capillary pumping of a working fluid. The presence of capillary structures allows to transfer the heat for distances up to several meters regardless of orientation in the gravity field, or to several tens of meters in horizontal position [5].

The heat exchanger is represented in figure 5.1, showing: a capillary pump (evaporator), a compensation chamber (reservoir), a condenser and vapor and liquid transport lines. The evaporator and the compensation chamber contain wicks, while the rest of the loop can be made in smooth tubing. The compensation chamber is the largest component of the loop and has two main functions: to accommodate excess liquid in the loop during normal operation and supply the capillary pump wick with liquid at all times, favored by the presence of a secondary wick set-up between the pump wick and the reservoir.

The wick in the evaporator, called primary wick, is made of fine pores to develop a high capillary pressure, able to circulate the fluid around the loop, while the secondary wick is made of larger pores to move the working fluid between the compensation chamber and the evaporator. The secondary wick physically connects the evaporator to the reservoir to supply the primary wick with liquid, particularly when the reservoir is below the evaporator or in microgravity conditions. Liquid and vapor lines are made of small-diameter tubing that may easily be arranged in tight spaces around the electronic devices [1].

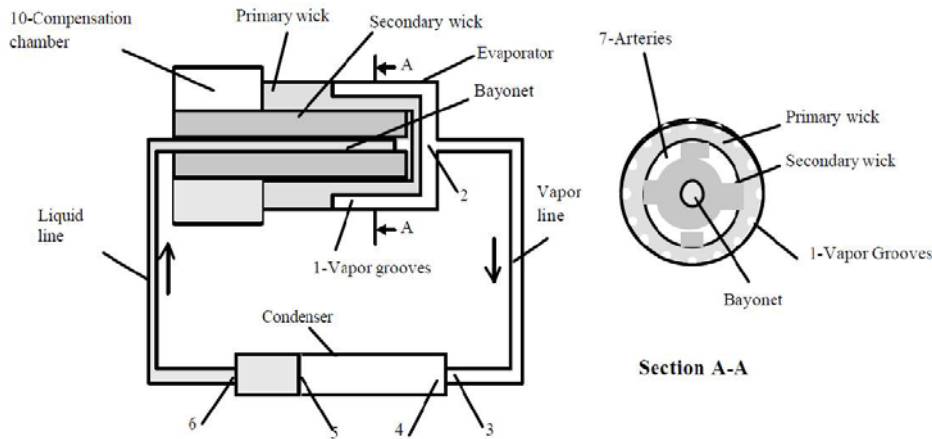


**Figure 5.1** General scheme of a LHP prototype [6].

### 5.1.2 Aim of the work

LHP wicks are generally made of plastics or metals by powder processing technique that consists in the pressing and sintering of the powders at high temperature, close to their melting point [7].

Thermoplastic polymers (ultra-high-molecular-weight polyethylene, polypropylene, high-density polyethylene, etc.) are in general used as plastic materials; beside some advantages like low level of thermal conductivity, high impact strength, low coefficient of friction and abrasion, they have some drawbacks like the formation of a non-optimized porosity with low capillarity. On the other hand, Ni and Ti are the most widely used metallic powders. The capillary structures obtained present quite small pore size and high strength, being compatible with many working fluids [7-9]. The disadvantages are the high level of thermal conductivity and the cost. The drawbacks displayed by plastic or metallic porous wicks may be overcome using low cost ceramic wicks with fine pore size, such as composite of alumina or alumina-silica oxide [7].

In this work, geopolymer porous wicks are studied as an innovative solution in order to decrease the cost and facilitate the preparation of the final LHP device. Furthermore, the thermal capacity may be increased thanks to the fine interconnected porosity, the high thermal and chemical inertia and the low thermal conductivity shown by the geopolymers.

A LHP prototype was designed with the evaporator part consisting in a metallic container with two internal geopolymer capillary structures (primary and

secondary wicks), coaxially inserted one inside the other. The geopolymer wicks have to possess different porosity in order to satisfy the functions of the device. The main issue was to produce a geopolymer primary wick with fine pores ( $\leq 1 \mu\text{m}$ ), for the development of a high capillary pressure able to circulate the fluid around the loop and a geopolymer secondary wick with larger pores ( $\geq 100 \mu\text{m}$ ), to manage the fluid flow between the compensation chamber and the evaporator. The porosity required for the primary wick results compatible with the porosity shown by metakaolin-based geopolymer resins studied in previous works [10-11]; furthermore, the porosity of the secondary wick can be obtained applying a foaming process to the same geopolymer resins [10-11]. In detail, an *in situ* inorganic foaming was induced by the addition of metallic Si powder, able to generate  $\text{H}_2$  in the alkaline geopolymer slurry, as described in paragraph 2.7.2. Several composite geopolymer mixtures are studied and characterized to obtain the desired porosity in the wicks. The process formation of the wicks is optimized and a final LHP prototype device is assembled and tested. The prototype is developed in the frame of the Italian Project PON01\_00375 “PANDION – Study of innovative functional Space-subsystems”.

## **5.2 Experimental procedure**

### **5.2.1 Production of the primary wick**

For the production of the primary wick, different composite mixtures are obtained using metakaolin, potassium di-silicate solutions with  $\text{H}_2\text{O}/\text{K}_2\text{O} = 12.0$  or  $13.5$  (see chapter 3 for compositions and preparation) and fused silica sand (Teco-Sil 150 I CE Minerals, 99.7 % purity, granulometry: 18.22 %  $> 125 \mu\text{m}$ , 61.04 %  $> 50 \mu\text{m}$ , 20.59 %  $< 50 \mu\text{m}$ ). The slurries, respectively coded G12 and G13, are produced by mixing the starting raw materials for 10 min at 100 r.p.m.

The mixtures are cast in plastic molds to verify the consolidation of the resins and to characterize the materials. The slurry are left for 24 h at r.t. and for 24 h at  $65^\circ\text{C}$  in a heater.

### **5.2.2 Production of secondary wick**

The production of the secondary wick is based on a near-net shaping technique to obtain the material with the final desired dimensions, without the necessity of mechanical refinements.

Different geopolymer slurries are produced using metakaolin and potassium disilicate solutions with  $H_2O/K_2O = 13.5$  or  $23.0$  (see chapter 3 for compositions and preparation). The slurries coded G13 and G23, respectively, are produced by mixing the metakaolin and the potassium aqueous solution for 10 min at 100 r.p.m.

Composite mixtures are obtained by the addition of fused silica sand (Teco-Sil 150 I CE Minerals) and water to improve the workability. Metallic Si powder (grade AX10, H.C. Stark, purity 99.995 %,  $D_{50} = 4.50 \mu m$ ), in different wt.% amounts, is added after the 10 min of mixing and mixed with the slurry for another min to induce the foaming of the slurry.

The slurries are cast in open plastic molds to allow the expansion of the mixture. The final complex shape of the secondary wick consists of two coaxial cylinders with external diameter of 1.3 cm, internal diameter of 0.6 cm and height of 8 cm. An appropriate plastic mold is created with the wished dimensions and the geopolymer slurry is directly cast inside the external cylinder.

Samples are cured at r.t. for 24 h, in a heater at  $65 \text{ }^\circ\text{C}$  for 24 h, then the samples, extracted from the mold, are left for other 24 h at  $65 \text{ }^\circ\text{C}$ . This curing treatment avoids a too fast evaporation of the water trapped in the pores, limiting the formation of cracks. Some samples are treated at  $800 \text{ }^\circ\text{C}$  in an oven for 1 h, to improve the mechanical resistance of the final consolidated material. The micrometric external layer of the produced pipes is removed by abrasive paper to increase the adhesion with the primary wick cast in a subsequent step.

### **5.2.3 Production of the LHP prototype**

Once selected the suitable mixtures for the production of the porous wicks, the evaporator part of the LHP prototype is assembled. The metallic evaporator is shown in figure 5.2a and the schematic configuration of the geopolymer wicks coaxially inserted inside is displayed in figure 5.2b.

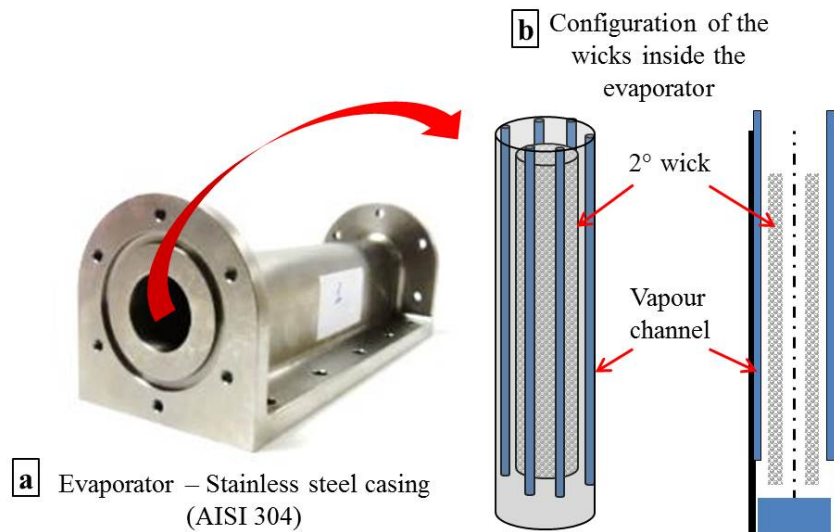


**Figure 5.2** Evaporator chamber of the LHP prototype (a). Schematic representation of the configuration of the geopolymer wicks inserted in the evaporator chamber (b).

The secondary wick, previously produced with the final dimensions and thermally treated, is inserted inside the evaporator chamber and between the templates for the production of the vapor channels (Fig. 5.2b). Six templates ( $\text{Ø}=2\text{mm}$ ) are used for the realization of the vapor channels. The mixture selected for the primary wick is directly cast in the chamber using a syringe to limit the entrapment of air bubbles in the matrix; rubber supports are produced to facilitate the casting of the mixture inside the chamber. The entire evaporator is cured for 96 h at r.t. and for further 96 h at  $40\text{ }^{\circ}\text{C}$  in a heater, to allow a gradual water evaporation.

### 5.3 Optimization of the production process of the wicks

#### 5.3.1 Primary wick

At first, the mixtures are cast in plastic molds to verify if the final samples result well consolidate and compact and to characterize the materials in view of the production of the LHP evaporator prototype.

The selection of the resin for the production of the primary wick is done taking into account that the matrix must consolidate in contact with the metallic chamber

of the evaporator, therefore, being subjected to high thermal stresses. The addition of a powder able to buffer the linear shrinkages of the geopolymer matrix results to be fundamental. Fused silica sand, with high thermal inertia ( $CTE \sim 5 \cdot 10^{-7} \text{ }^\circ\text{C}^{-1}$ ) and low thermal conductivity ( $\sim 1.3 \text{ W} \cdot \text{m}^{-1} \text{ K}^{-1}$ ), is directly used for the formulation of the primary wick, to counteract the possible occurrence of crack formation.

The porosity required for the production of the primary wick must have a pore size  $\leq 1 \mu\text{m}$  to enhance the development of a high capillary pressure able to circulate the fluid around the loop. The intrinsic mesoporosity of the geopolymer ranges between 0.01 and  $1 \mu\text{m}$ , as reported in paragraph 2.6, and it is affected by several factors among which the most important is the water content in the starting slurry. Since water acts as a pore former [12-13], mixtures with a low content of water ( $\text{H}_2\text{O}/\text{K}_2\text{O} = 13.5$  or  $12.0$ ), although sufficient to ensure a good workability and casting, have to be preferred to obtain a finer porosity and low shrinkages by drying. The use of the silicate with dilution  $\text{H}_2\text{O}/\text{K}_2\text{O} = 12.0$  results ideal to generate a fine porosity, to facilitate the consolidation process of the wick and reduce the linear shrinkage.

In Table 5.1 the composition and curing, of the final mixture selected for the realization of the primary wick, are reported.

### 5.3.2 Secondary wick

Different mixture compositions are formulated using the starting mixtures G13 or G23 and adding different quantity of  $\text{Si}^0$ , used as foaming agent, and in some cases fused silica.

An excessive expansion is found in foams obtained by the addition of high silicon amounts (0.03-0.04 wt.%). The mold geometry and the volume of the mixture, used during the casting, result to highly affect the foaming process. As reported in paragraph 2.7.2, the foam volume expansion results affected by the ratio between the surface of the foam exposed to the air and the initial volume of the mixture. This ratio define the linear expansion of the foam along the preferential z axis, that is the distance between the exposed surface before and after the expansion [14].

A  $\text{Si}^0$  amount equal to 0.03 – 0.04 wt.% results excessive for the development of homogeneous foams, cast in molds with an high length/diameter ratio; the fast

production of H<sub>2</sub> instantly blows up the slurry, that starts to come out the mold. The use of a lower amount of Si<sup>0</sup> (0.01 wt.%) limits a fast and violent production of H<sub>2</sub>, avoiding the leak of the slurry out of the mold.

Concerning the starting slurries, mixture G13 results more suitable for the process formation of the final foam. Indeed, slurry G23 contains a higher amount of water that increase the generation of an intrinsic mesoporosity in the geopolymer matrix [10] and the formation of bigger pores due to the foaming process. The more diluted G23 slurry allows H<sub>2</sub> bubbles to easily spread and inflate, leading to the production of brittle and fragile consolidated foams. Furthermore, the consolidation of these foams results prolonged in time; water removal is slow and often incomplete because of the higher length/diameter ratio of the mold.

The production of secondary wick pipes, obtained by the foaming of slurries formulated only with metakaolin and potassium silicate solution, evidences the presence of shrinkages and cracks, due to the water evaporation during the consolidation in temperature of the materials. Fused silica sand is added, in the formulation of the geopolymer foam, to counteract the dimensional shrinkage due to the thermal stability. The particle size of the powder and the specific surface area are respectively slightly larger and much lower than the metakaolin, in order to achieve an optimum workability without an excessive addition of water.

Furthermore, the use of the silica in the primary wick formulation does necessary to use silica also for the secondary wick, to have similar thermal behavior of the wicks during LHP operation.

The secondary wick, obtained using of a reduced Si<sup>0</sup> amount (0.01 wt.%) and fused silica, whose composition is reported in Table 5.1, results compact and without shrinkages and cracks. The mechanical resistance and the porosity further increase after the thermal treatment at 800 °C.

**Table 5.1** Sample code, composition and curing of the selected composite mixtures used for the production of the secondary and primary wicks.

Sample	Composition (wt.%)					Curing
	Metakaolin	K-silicate	Si	SiO <sub>2</sub>	H <sub>2</sub> O	
1° wick	36.30	H <sub>2</sub> O/K <sub>2</sub> O = 12.0 54.60	-	9.10	-	24 h r.t. + 24 h 65 °C
2° wick	34.60	H <sub>2</sub> O/K <sub>2</sub> O = 13.5 55.10	0.01	9.10	1.10	24 h r.t. + 24 h 65 °C

## 5.4 Characterization

### 5.4.1 Rheology of the starting composite slurries

The viscosities of the selected mixtures for the production of the primary and the secondary wicks, before the addition of the foaming agent, are characterized with a controlled-stress rotational rheometer (parallel plate sensor,  $\varnothing=20$  mm, gap forced to 1 mm). The logarithmic plots of the viscosity versus the shear rate of the slurries are shown in figure 5.3.

The starting geopolymer slurries exhibit a pseudo-plastic behavior with values of viscosity at  $100\text{ s}^{-1}$  equal to 0.49 and 2.72 Pa·s for the primary and secondary wicks, respectively. The viscosity is greatly dependent on the  $\text{H}_2\text{O}/\text{K}_2\text{O}$  molar ratio, equal to 13.5 for the secondary wick and to 12.0 for the primary wick [11], because of the rheological behavior controlled by hydrodynamic effects, namely the viscosity of the aqueous alkaline activator [15]. In fact, the slurry of the primary wick exhibits a viscosity one order of magnitude higher than the viscosity of the secondary wick. The lower viscosity of the secondary wick is necessary to ensure the subsequent foaming of the slurry after the addition of the blowing agent. However, both the viscosities of the starting slurries are suitable for the casting process.

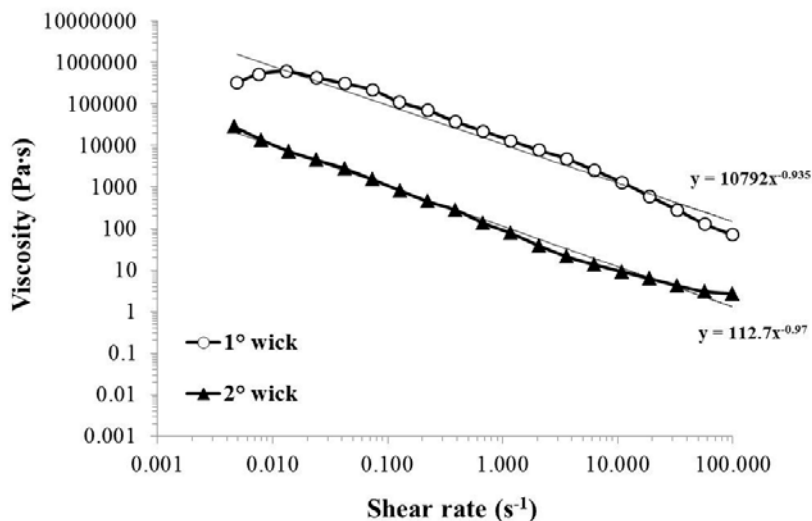


**Figure 5.3** Logarithmic plots of the viscosity versus the shear rate of the primary and the secondary wick slurries before the addition of the blowing agent. The data error is  $\pm 5\%$ .

### 5.4.2 Macro and microstructural characterization of the wicks

The secondary wick pipe produced (Fig. 5.4a, b) presents a smooth and compact surface due to the superficial tension solid/liquid generated during the consolidation. The micrometric layer is removed by abrasive paper to increase the adhesion with the mixture cast for the production of the primary wick (Fig. 5.4b). The macroporosity generated by the foaming process, visible in the cross section in figure 5.4a, appears quite homogenous and formed by rounded macropores. Conversely, the primary wick, obtained by the casting in plastic cylindrical mould, results compact with some big pores due to air bubbles entrapped in the matrix during the casting (Fig. 5.4c). The real density ( $\rho_0$ ) of the wicks results  $\approx 2.3 \text{ g}\cdot\text{cm}^{-3}$  for both the wicks, while the bulk density ( $\rho$ ) is different and lower for the foamed structure of the secondary wick (Table 5.2). The secondary wick, subjected to the foaming process, develops a bulk density equal to  $1.06 \text{ g}\cdot\text{cm}^{-3}$ , while the denser primary wick show a value of  $1.37 \text{ g}\cdot\text{cm}^{-3}$ . As a consequence, the total porosity ( $X_p$ ) is higher for the foamed secondary wick (Table 5.2).

**Table 5.2** Real density ( $\rho_0$ ), bulk density ( $\rho$ ), total porosity percent ( $X_p$ ) and specific surface area ( $S_{sa}$ ) of the produced wicks.

Sample	$\rho_0$ ( $\text{g}\cdot\text{cm}^{-3}$ )	$\rho$ ( $\text{g}\cdot\text{cm}^{-3}$ )	$X_p$ (%)	$S_{sa}$ ( $\text{m}^2\cdot\text{g}^{-1}$ )
1° wick	2.28	1.37	40	74.60
2° wick	2.35	1.06	55	54.88

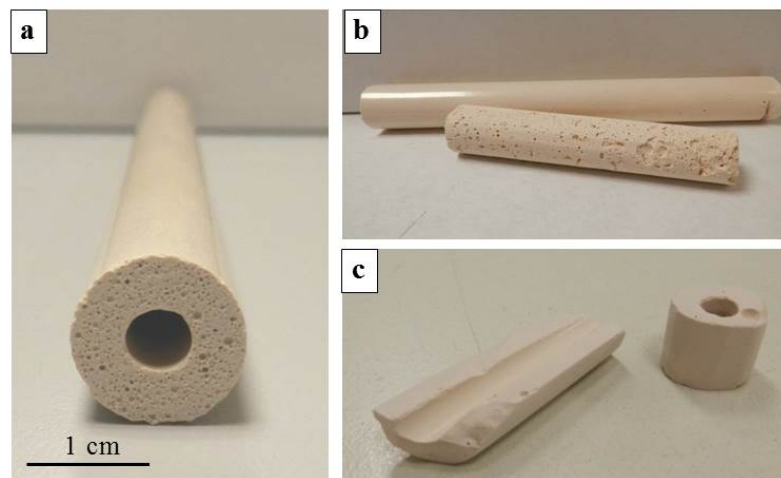


**Figure 5.4** Secondary wick pipes before (a) and after (b) the removal of superficial layer. Primary wick obtained in plastic cylindrical mold (c).

The SEM micrographs of the wick microstructures are reported in figure 5.5. The microstructure of the matrices is observed to assess the presence of the porosity required for the operational functions of the device. In the SEM micrographs, the presence of the characteristic geopolymer microstructure, formed by precipitates arising from the geopolymerization reaction, is evident for both the wicks (Fig. 5.5b, d).

The secondary wick macroporosity, in the required dimensional range ( $\geq 100 \mu\text{m}$ ), is obtained by the foaming method adopted and well visible in figure 5.5c. The low density of the starting slurry, as observed in the rheological analysis, allows an easy expansion of the  $\text{H}_2$  bubbles within the slurry, with consequent formation of big pores, further increased by the thermal treatment at  $800 \text{ }^\circ\text{C}$ . At this temperature, the beginning of the sintering by the viscous flow (discussed below), leads to the formation of bigger pores by coalescence of the smallest pores present in the geopolymer matrix (Fig. 5.5d).

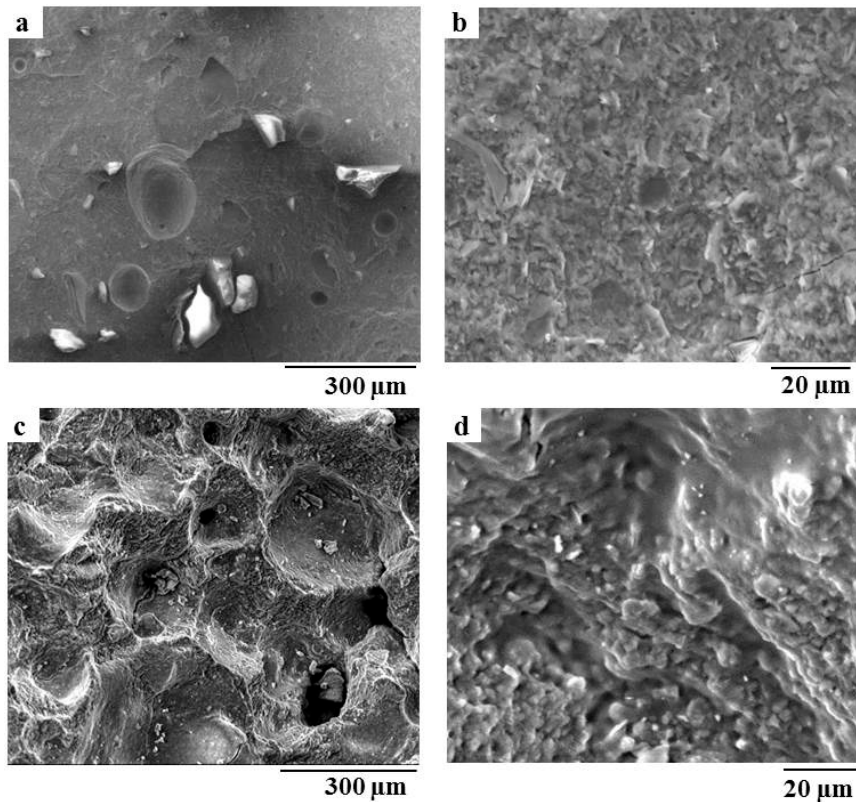


**Figure 5.5** SEM micrographs of the primary (a, b) and the secondary wicks (c, d).

Concerning the primary wick, the resin develops a compact structure with smaller pores, unlike to the microstructure of the secondary wick (Fig. 5.5a, b). Porosity is formed by the characteristic mesopores of the geopolymer resin and the micrometric pores generated by the water, that acts as a pore former agent [12]. Some macropores are visible in the microstructure of the matrix (Fig. 5.5a), arising from the air bubbles trapped during the slurry casting.

The microstructures of the wicks show the presence of silica particles recognizable by the irregular and angular shape (Fig. 5.5a, c). Fused silica is reactive in the geopolymerization but, because of the coarse particles, it reacts mainly on the surface and the core part of the grains may remain unreacted.

#### **5.4.3 Analysis of the porosity of the wicks**

The porosity of the wicks is investigated in the range 0.058-100  $\mu\text{m}$  by Hg intrusion porosimetry. The pore size distributions obtained are displayed in figure 5.6.

This analysis mostly account for the intrinsic porosity of the geopolymer matrix and in part the smallest macropores, due to the foaming process.

The primary wick distribution (Fig. 5.6a) is monomodal and concentrated in the range 0.01-0.1 $\mu\text{m}$ , specific for the intrinsic mesoporosity of the geopolymer matrix. The pore size results in compliance with the porosity range required for the production of the primary wick, with an average pore diameter equal to 0.02  $\mu\text{m}$ .

The distribution obtained for the secondary wick is broader (Fig. 5.6b). The presence of the intrinsic geopolymer porosity in the range 0.01-0.1 $\mu\text{m}$  is evident, but the foaming process together with the thermal treatment, as well the higher water amount in the starting mixture, lead to the formation of bigger pores with diameter in the range 0.1-100  $\mu\text{m}$ .

Geopolymers with high Si/Al ratio develop smaller pores [16], therefore the use of fused silica increases the Si-content and enhances the formation of pores with small dimensions, evident in both the distributions.

The accessible porosity and total pore volume result equal to 48 % and 388  $\text{mm}^3\text{g}^{-1}$  for the secondary wick and to 38 % and 272  $\text{mm}^3\text{g}^{-1}$  for the primary wick, confirming that the secondary wick presents a more porous matrix.

The presence of a finer porosity determines an higher value of specific surface area, equal to  $75 \text{ m}^2 \cdot \text{g}^{-1}$  for the primary and  $55 \text{ m}^2 \cdot \text{g}^{-1}$  for the secondary wicks (Table 5.2). The lower value of surface area, shown by the secondary wick, is also due to the partial sintering of the geopolymer particles occurring at  $800 \text{ }^\circ\text{C}$ .

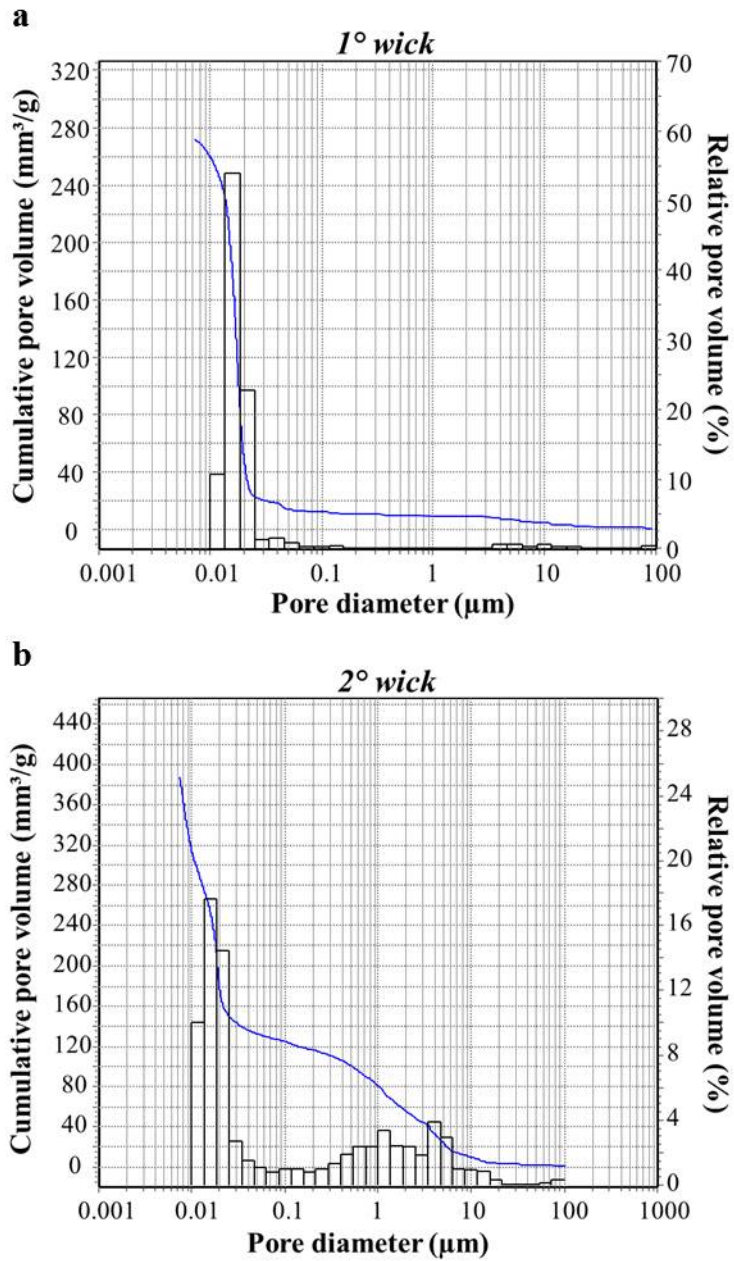


**Figure 5.6** Pore size distributions obtained by Hg intrusion analysis of the primary (a) and the secondary wicks (b).

#### 5.4.4 Thermal behavior of the wicks

The thermal behavior of the geopolymer wicks is investigated by dilatometric analysis up to 1200 °C in static air (heating rate 10 °C·min<sup>-1</sup>).

The dilatometric curves of the primary and the secondary wicks, before and after the thermal treatment at 800 °C, are shown in figure 5.7. The materials exhibit patterns analogous to those reported in literature [17]. The thermal profile may be divided in four temperature ranges, as a function of the phenomena occurring :

- I – 25-150 °C: evaporation of the residual water
- II – 150-350 °C: desorption of water trapped in the pores
- III – 350-850 °C: dehydroxilation of the group T-OH (T=Si, Al)
- IV –  $\geq$  850 °C: sintering by viscous flow and fusion of the sample

The curve of the primary wick follows the trend reported in literature [17], while the secondary wick reports some differences. The differences are probably due to an incomplete geopolymerization reaction; it has been shown in previous works [11], that a balance between the geopolymerization and the redox reaction of the metallic silicon is necessary to achieve a complete geopolymerization. The thermal profile of the secondary wick foam differs from the literature one, in the ranges II and III, since a slowdown in the shrinking is observed, followed by an expansion. This behavior is due to the superimposing of many thermal phenomena, as dilatation of unreacted metakaolin, desorption of water trapped into the pores and glass transition of unreacted alkali silicate [18-19].

In the primary wick there is no evidence of inflection linked to the glass transition of the potassium silicate. In this case the geopolymerization is not affected by the silicon redox reaction and the curing applied to the matrix results to be suited to favor a complete reaction.

In the IV range, liquid phase sintering occurs for both the wicks. Sintering by a viscous flow mechanism [20] of glassy particles produces simultaneous shrinkage and neck growth, due to the nature of material transport. In the case of metakaolin and K-based geopolymers, shrinkages, due to liquid formation, occur at 850 °C. For the wicks, the sintering is considerable at temperature over 900 °C due to the presence of fused silica, that is thermally stable.

Concerning the curves of the secondary wicks, the trends are similar although one wick is treated at 800 °C before the analysis. The secondary wick not treated shows a slightly higher shrinkage in the first range, due to the evaporation of the water, and an higher shrinkage by the viscous flow over 900 °C. Therefore, the treatment at 800 °C is useful to limit the shrinkage in temperature. However, the wicks show a thermal resistance much higher than that required for the operation of the LHP, that must manage a working fluid heated at maximum 70 °C.

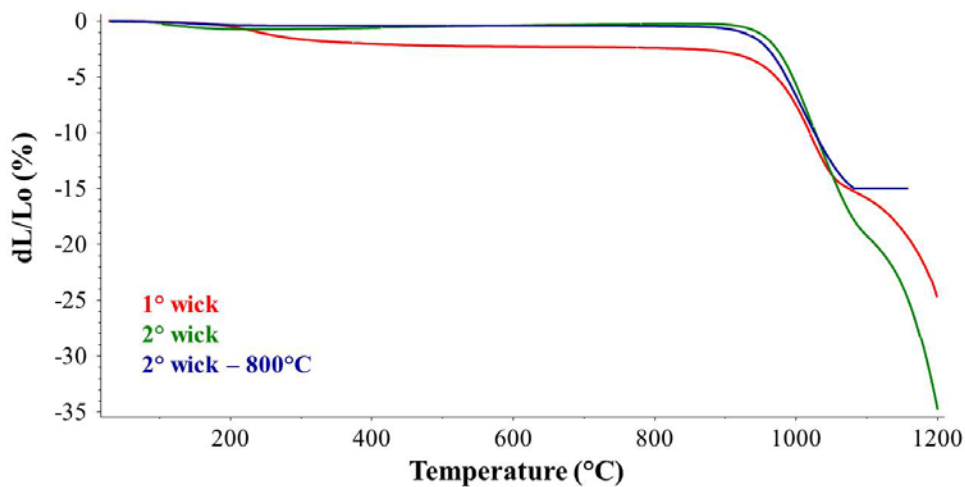


**Figure 5.7** Dilatometric analyses of the primary and the secondary wick, before and after the thermal treatment at 800 °C.

### 5.5 LHP prototype

The characterization of the composite materials, used for the production of the wicks, evidenced that the porosity requirements for the functional operations of the LHP have been achieved.

In the prototype assembly, special attention has to be done on the adhesion between the secondary wick, already produced and consolidated, and the primary wick directly cast inside the evaporator chamber, as well on the adhesion between the primary wick and the metallic chamber of the evaporator. Indeed, it is possible to encounter shrinkages due to thermal stresses arising from the curing and the adhesion of the geopolymer on the metallic curved surfaces. The direct cast of the primary wick inside the container allows to improve the interface adhesions and, consequently, the heat transfer.

The curing treatment, applied on the fully-assembled evaporator chamber, is set to enhance the consolidation of the primary wick cast in the chamber and warrant a gradual water removal, to avoid the formation of cracks in the geopolymer matrix. The curing, for 96 h at r.t. and 96 h at 40°C, develops a well consolidate primary wick, with a good adhesion between the interfaces metal-primary wick (Fig. 5.8) and primary-secondary wicks (Fig. 5.9).

The high resolution photos of figure 5.9 show the good adhesion between the two geopolymer wicks and the different porosity generated by the selected mixtures. The removal of the superficial layer of the secondary wick ensures the good adhesion between the geopolymer wicks.

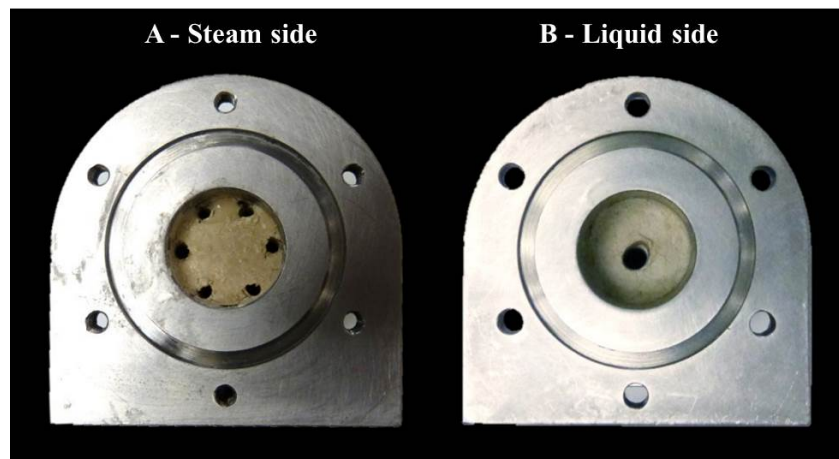


**Figure 5.8** Vapor side (a) and liquid side (b) of the evaporator chamber obtained by consolidation of the primary wick.

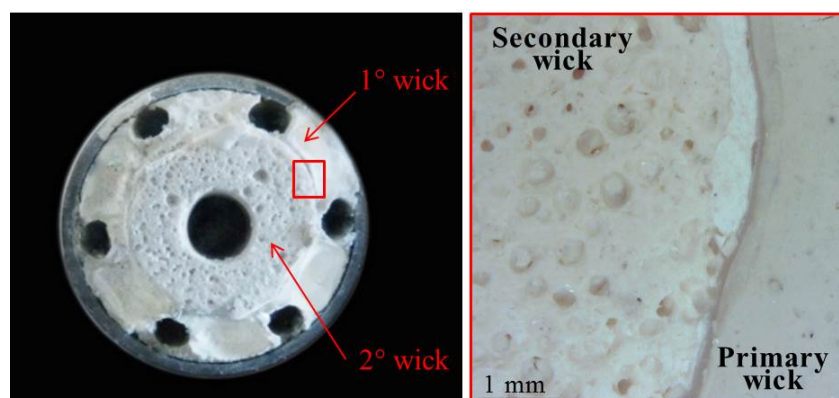


**Figure 5.9** Cross section of the evaporator and details of the interface between the primary and the secondary wicks.

Once assembled the LHP prototype, the heat exchange properties of the evaporator were tested at SAB Aerospace S.r.l. laboratories. The produced evaporator prototype is assembled in a LHP breadboard, as shown in figure 5.10, and acetone is used as working fluid. A silicon skin heater, placed at the bottom of the LHP evaporator, supplies the heat load and the condenser is in thermal contact with a thermostatic bath to simulate the heat sink during operative conditions. LHP performances are tested in the range  $-35\text{ }^{\circ}\text{C}$  -  $+70\text{ }^{\circ}\text{C}$  (50W power input) and LHP temperatures are measured in several device locations to perform a functional test. The experimental results show good thermal management performances: the startup phase is quicker and the evaporator wall temperature lower, if compared to the traditional wick-LHP at steady state conditions. This preliminary results reveal that the use of geopolimer mixtures to produce internal evaporator wicks is a promising improving technology to produce LHP apparatus for space applications.

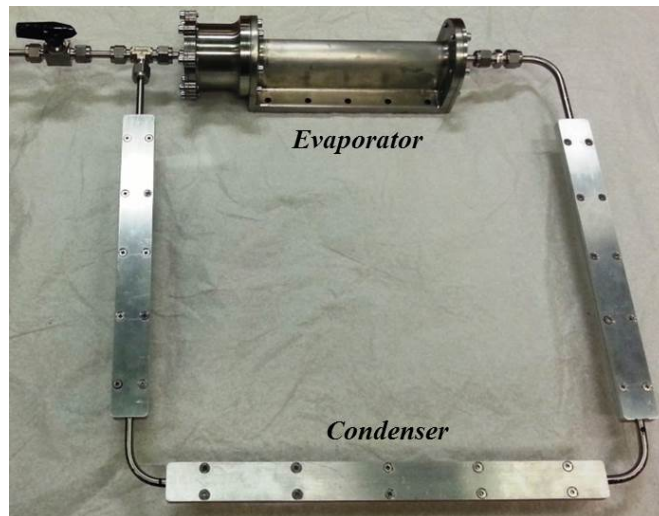


**Figure 5.10** LHP breadboard used in the thermal exchange tests.

## 5.6 Conclusions

The study is focused on the prototyping of the evaporator part of a loop heat pipe (LHP), where the conventional metallic or plastic wicks are replaced by innovative concentric geopolimer wicks. The fine porosity of the primary wick (pores  $\leq 1\text{ }\mu\text{m}$ ), for the development of an high capillary pressure able to circulate the fluid around the loop, is achieved through the casting of a geopolimer resin.

The more porous secondary wick, for the movement of the working fluid between the compensation chamber and the evaporator, is obtained through the production of a foamed geopolymer pipe. The study on the mixtures composition and on the optimization of the process formation of the wicks, reveal that geopolymers with the required porosity may be designed and tailored to satisfy the final purposes of the wicks.

Moreover, the use of geopolymer materials combined with the production process at low temperature and with simple techniques of near net shaping and casting *in situ*, allow to lower the production costs of the wicks in the LHP evaporator.

The good thermal exchange performances, obtained in preliminary tests, reveal as the use of geopolymer mixtures to produce the wicks is a promising technology for the production of LHP. However, further experimental tests are required to better design the porosity in a sharp dimensional range, able to endow the device with improved properties suitable for space applications.

## References

- [1] S. Launay, V. Sartre, J. Bonjour, Parametric analysis of loop heat pipe operation: a literature review, *Int. J. Therm. Sci.* 46 (2007) 621–636.
- [2] A.A. Orlov, K.A. Goncharov, E.Y. Kotliarov, T.A. Tyklina, S.N. Ustinov, The loop heat pipe experiment on board the GRANAT spacecraft, in: 27<sup>th</sup> ICES, Noordwijk (NL), 20–22 May 1997, 13 pp.
- [3] J. Baumann, S. Rawal, Viability of loop heat pipes for space solar power applications, in: 35<sup>th</sup> AIAA Thermophysics Conference (AIAA-2001-3078), Anaheim CA (USA), 11–14 June 2001, 10 pp.
- [4] T.T. Hoang, J. Ku, Advanced loop heat pipes for spacecraft thermal control, in: 8<sup>th</sup> AIAA/ASME Joint Thermophysics and Heat Transfer Conference (AIAA-2002-3094), St. Louis Missouri MO (USA), 24–26 June 2002, 8 pp.
- [5] Yu.F. Maydanik, Loop heat pipes, *Appl. Therm. Eng.* 25 (2005) 635–657.
- [6] J. Ku, Operating characteristics of loop heat pipes, SAE Technical Paper 1999-01-2007 (1999), doi:10.4271/1999-01-2007.

- [7] L. Vasiliev, Advanced loop heat pipe evaporator with ceramic nanostructured composite of alumina, alumina-silica oxide as a wick structure, SAE Technical Paper 2007-01-3192 (2007), doi:10.4271/2007-01-3192.
- [8] Means of manufacturing sintered porous materials from nickel powder, USSR Inventor Certificate 703976 (1979).
- [9] Means of manufacturing sintered porous materials from titanium powder, USSR Inventor Certificate 1034273 (1983).
- [10] E. Landi, V. Medri, E. Papa, J. Dedeczek, P. Klein, P. Benito, A. Vaccari, Alkali-bonded ceramics with hierarchical tailored porosity, *Appl. Clay Sci.* 73 (2013) 56-64.
- [11] V. Medri, E. Papa, J. Dedeczek, H. Jirglova, P. Benito, A. Vaccari, E. Landi, Effect of metallic Si addition on polymerization degree of *in situ* foamed alkali-aluminosilicates, *Ceram. Internat.* 39 (2013) 7657-7668
- [12] Z. Zuhua, Y. Xiao, Z. Huajun, C. Yue, Role of water in the synthesis of calcined kaolin-based geopolymer, *Appl. Clay Sci.* 43 (2009) 218-223.
- [13] K. Okada, A. Ooyama, T. Isobe, Y. Kameshima, A. Nakajima, K.J.D. MacKenzie, Water retention properties of porous geopolymers for use in cooling applications, *J. Eur. Ceram. Soc.* 29 (2009) 1917-1923
- [14] E. Kamseu, E. Landi, Capitolo 9: Geopolimeri e materiali porosi, in Geopolimeri: polimeri inorganici chimicamente attivati, C. Leonelli, M. Romagnoli, Lulu.com (2011) 222-251.
- [15] A. Favier, J. Hot, G. Habert, N. Roussel, J.B. d'Espinose de Lacaillerie, *Soft Mater.* 10 (2014) 1134–1141.
- [16] P. Duxson, J.L. Provis, G.C. Lukey, S.W. Mallicoat, W.M. Kriven, J.S.J. van Deventer, Understanding the relationship between geopolymer composition, microstructure and mechanical properties, *Colloid. Surface. A* 269 (2005) 47-58.
- [17] J.L. Bell, P.E. Driemeyer, W.M. Kriven, Formation of ceramics from metakaolin-based geopolymers. Part II: K-based geopolymer, *J. Am. Ceram. Soc.* 92 (2009) 607–15.
- [18] W. Mi-tang, C. Jin-shu, Viscosity and thermal expansion of rare earth containing soda-limesilicate glass, *J. Alloys Compd.* 504 (2010) 273-276.
- [19] H.F. Shermer, Thermal expansion of binary alkali silicate glasses, *J. Res. Natl. Bur. Stand.* 52 (1956) 97-101.

[20] W. D. Kingery, M. Berg, Study of the initial stages of sintering solids by viscous flow, evaporation-condensation, and self-diffusion, *J. Appl. Phys.* 26 (1955) 1205-1212.

## **6. Addition of fillers to generate a macroporosity**

The use of fillers in the geopolymer compositions is useful to give specific properties and to increase the porosity of the material when adequate fillers are used. For example, expanded aggregates allow the production of porous and lightweight composite geopolymers, as well as the use of reactive filler able to generate gas, causing the foaming of the geopolymer slurry.

In the first part of this chapter (section 6.1), an inert filler (expanded vermiculite) is used for the production of geopolymer composite insulating panels. The research activity was carried out in the frame of the Project “MATEC — New materials and new technologies for internal combustion co-generator prototype”, funded by the Italian Ministry of Economic Development.

The second part of the chapter (section 6.2), is based on a preliminary research activity, developed during a 3-months stage at the “Laboratoire Science des Procédés Céramiques et de Traitements de Surface UMR-CNRS 7315” of the University of Limoges (France), focused on the use of a reactive filler, silica fume, for the production of composite foams designed for a range of possible thermo-acoustic insulating and fire-proofing applications.

### **6.1 Addition of inert filler: lightweight geopolymer-vermiculite composites.**

#### **6.1.1 Introduction**

The use of expanded fillers is one of the method that may be adopted to increase the geopolymer porosity, creating lightweight materials. Geopolymer-based composites, with expanded vermiculite as lightweight aggregates, were produced and characterized to obtain fireproof precast panels with thermal insulating properties [1]. The completely inorganic nature of the materials renders the composite totally non-combustible. Both geopolymer binder and expanded vermiculite do not contain water in their framework, preventing the degradation at high temperature due to the conversion of the structural water in steam [2].

Vermiculite is a mineral of the the hydromicas group, a complex hydrated aluminum and magnesium silicate, that may expand to 8–20 times its original thickness (exfoliation), by heating above 300 °C. Expanded vermiculite was selected as filler because of the particular structure formed by thin plates separated by air gaps that confers heat insulating, due to the low thermal conductivity value of air. Furthermore, the high thermal stability, owing to its ability to relax temperature stress during heating, renders vermiculite a suitable filler for high temperature applications [3-4].

The low density of the expanded aggregates results ideal for the production of lightweight panels, where the filler may be bound by a geopolymer matrix that presents good thermal and fire-resistance properties. The intrinsic mesoporosity of the geopolymer binder may be combined with the macroporosity introduced by the presence of vermiculite. Different compositions of the geopolymer binders (metakaolin or alumina-based) and three sizes of expanded vermiculite were tested to assess how the density, solidity, thermal and mechanical behavior may be modified within the composite materials.

## **6.1.2 Experimental procedure**

### **6.1.2.1 Production of the composites**

The starting raw materials are selected in order to have reproducible and homogenous mixtures, able to produce geopolymer binders easy to be investigated, with good thermal and mechanical performances. Powders with high specific surface area are selected to favour the hydrolysis and enhance the geopolymerization process [5]. Starting mixtures are prepared using a commercial metakaolin (see chapter 3), coded as Mk, or a commercial  $\alpha$ -Alumina (CT 3000 SG, Almatiss, coded as Al) used both as starting powder and refractory filler stable at high temperature. Expanded vermiculite with three sizes (type 2, 3, 4 – Pull Rhenen) is used as lightweight filler. The characteristics of the starting raw materials are reported in Table 6.1.

A potassium based activating solution is selected to maximize the polycondensation during the geopolymerization. As alkali solutions are tested a commercial potassium poly-silicate solution, coded as Ksilcom, and a potassium

di-silicate solution with  $H_2O/K_2O = 23.0$ , coded as Ksil23 (see chapter 3 for compositions and procedures).

**Table 6.1** Characteristics of the starting raw materials: metakaolin Mk, alumina Al and vermiculite (type 2, 3, 4).

Material	D <sub>50</sub> ( $\mu\text{m}$ )	Density ( $\text{g}\cdot\text{cm}^{-3}$ )	Ssa ( $\text{m}^2\cdot\text{g}^{-1}$ )	Crystalline phase
Metakaolin Mk	1.7	2.20	19.0	Quartz Muscovite (traces)
Alumina Al	0.5	3.99	7.8	Corundom Bauxite (traces)
Vermiculite Type 2	3.0	$0.095 \pm 20\%$	-	Micas/phlogopite
Type 3	5.0	$0.090 \pm 20\%$		Hydrated vermiculite
Type 4	10.0	$0.085 \pm 20\%$		(in type 3 and 4)

The metakaolin or alumina-based composites are produced mixing the starting powder with the potassium silicate solution for about 10 min. Expanded vermiculite and water (if required) are subsequently added and thoroughly mixed until uniform mixtures are obtained. The resulting slurries are cast in rubber molds with different dimensions and pressed to obtain smooth and planar surfaces.

A customized curing method is set up for each mixture in order to achieve a gradual water removal avoiding excessive shrinkages, planar deformations and crack formation. In detail, materials prepared with metakaolin are cured for 24 h at room temperature (r.t.) in closed molds, then for 24 h at 80 °C in closed molds and finally for 48 h in open molds at 80°C. Materials prepared with alumina powder are cured for 72 h at r.t. in closed molds, then for 48 h at 80 °C in closed molds and finally 24 h at 80 °C in open molds.

A schematic representation of the production process of the composite materials is reported in figure 6.1.

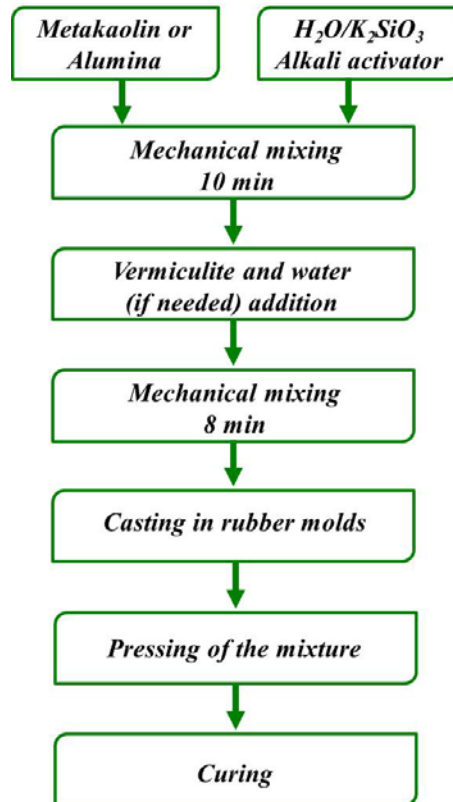


**Figure 6.1** Scheme of the production process for the vermiculite-based geopolymer composites.

### 6.1.2.2 Scale-up of the production process

The preparation of the composite materials is initially tested on small scale in order to identify the best mixtures suitable for the production of the final panels, as schematically illustrated in figure 6.2. Cylindrical samples with 4 cm diameter and 2.5 cm height are produced to verify the solidity and the morphology of the consolidated materials. The compositions of the mixtures are set-up by a trial and error approach: several tests are made to identify the best ratio between the starting raw powder, the alkaline solution and the filler. Increasingly quantities of vermiculite are added to starting geopolymer resins to identify maximum volume of filler that the binders may incorporate. When necessary, the mixtures are optimized to improve the mixing and the casting by water addition. The quantity of potassium silicate is selected to promote a complete geopolymerization, minimizing the amount of free unreacted potassium silicate.

From a first macroscopic screening, the mixtures that generate solid and compact samples are selected to test the forming process of tiles with dimension 10cm x

10cm x 2cm, in view of the production of the final panels. The workability and reproducibility of the samples are assessed using a single batch of each composition to produce at least five tiles.

The macro- and microstructure as well as the thermal and mechanical properties of the composite materials are investigated to select the best three mixtures suitable for the preparation of the final panels, which must have good heat-resistant and mechanical properties.

The final compositions selected for the realization of the panels are reported in Table 6.2; four panels, with dimensions 55cm x 47cm x 3cm, are produced for each composition.

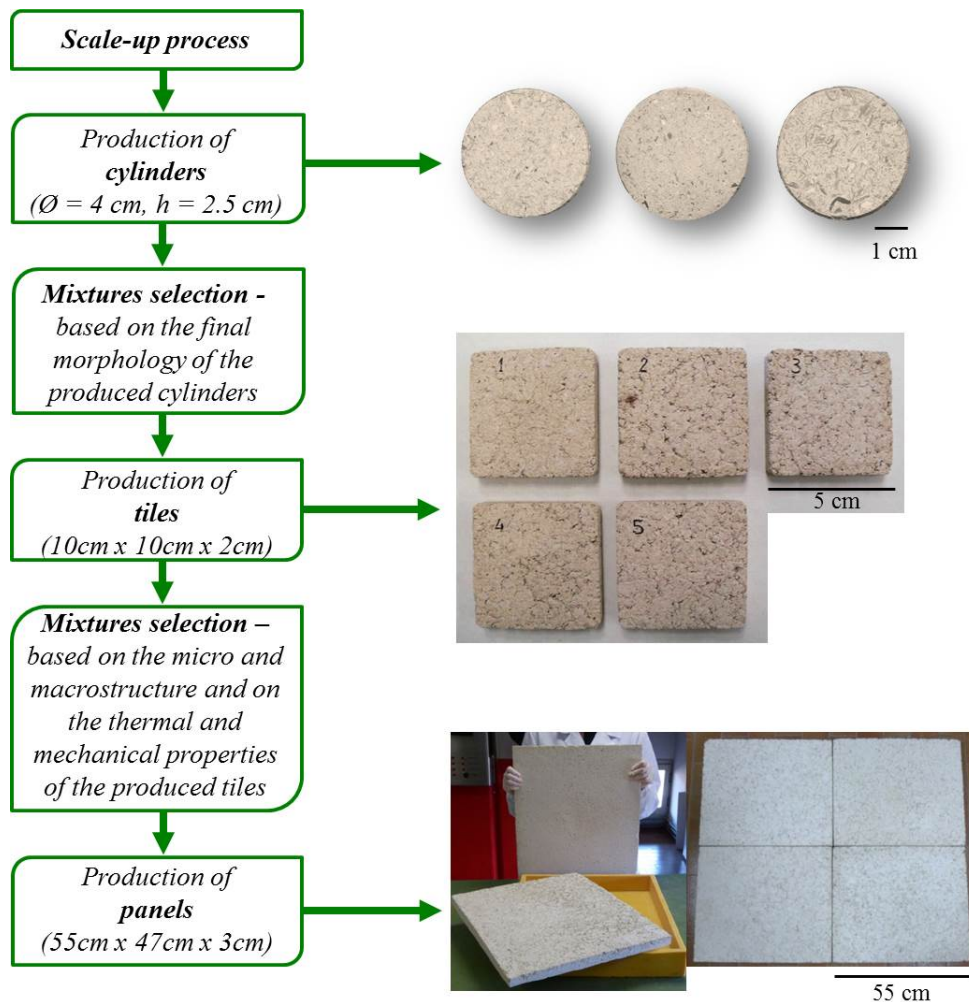


**Figure 6.2** Scale-up of the production process.

**Table 6.2** Compositions of the selected mixtures used for the production of panels.

Sample	Raw powder (wt.%)	K-silicate (Ksilcom) (wt.%)	H <sub>2</sub> O (wt.%)	Vermiculite (Type – wt.%)
V2-Mk	Mk – 24	47	9	Type 2 – 20
V4-Mk	Mk – 26	53	-	Type 4 -21
V4-Al	Al – 26	53	-	Type 4 -21

### 6.1.3 Characterization of the composite panels

#### 6.1.3.1 Macro and microstructural characterization

Each panel produced show good handling characteristic: the moderate size and weight result suitable for mounting and demounting operations, with a final shrinkage lower than 2 %. The average weight of the panels, reported in Table 6.3, is about 6 kg for each composition. Sample V4–Al, prepared from alumina and vermiculite type 4 presents the highest weight standard deviation, probably due to the lower reactivity of alumina raw powder [6], in comparison to metakaolin, and the higher density.

The average geometric densities range between 0.72 and 0.84 g·cm<sup>-3</sup> (Table 6.3). The differences between the values mainly depend on the type of vermiculite used. Panels V2–Mk possess higher density, respect to V4–Mk and V4–Al panels, because of the higher density of vermiculite type 2 (95 kg·m<sup>-3</sup> versus 85 kg·m<sup>-3</sup> of type 4) and of the smaller mean grain size (3 mm instead of 10 mm in type 4) that increase the particle packing. In figure 6.3, the high resolution images show the macrostructure of the machined cross sections of the panels. Composite V2–Mk (Fig. 6.3a), has a more homogeneous distribution of the aggregates containing the smaller-size vermiculite, that can be easily distributed in the mixture. Conversely, the expanded vermiculite type 4 appears, within the composites V4–Mk (Fig. 6.3b) and V4–Al (Fig. 6.3c), as elongated and compressed aggregates with high aspect ratio, in part piled and aligned perpendicularly to the casting direction. Although the shrinkage after consolidation is very low (2 %), the loss of the water absorbed between the plates of the vermiculite during the preparation of the slurry, causes a partial compression, conferring the anisotropic macrostructure observed for panels V4–Mk and V4–Al (Fig. 6.3b,c).

**Table 6.3** Average weight, bulk density ( $\rho$ ) and total porosity ( $X_p$ ) of the produced panels. Maximum percentage of absorbed water (WS) reached after water saturation and mass loss ( $\Delta\text{wt.}\%$ ) after drying.

Sample	Average weight (kg)	$\rho$ ( $\text{g cm}^{-3}$ )	$X_p$ (%)	WS (wt.%)	$\Delta\text{wt.}\%$
V2-Mk	6.23±0.02	0.84±25	61	49	-11
V4-Mk	6.07±0.05	0.72±25	73	48	-10
V4-Al	6.06±0.20	0.74±25	65	54	-10

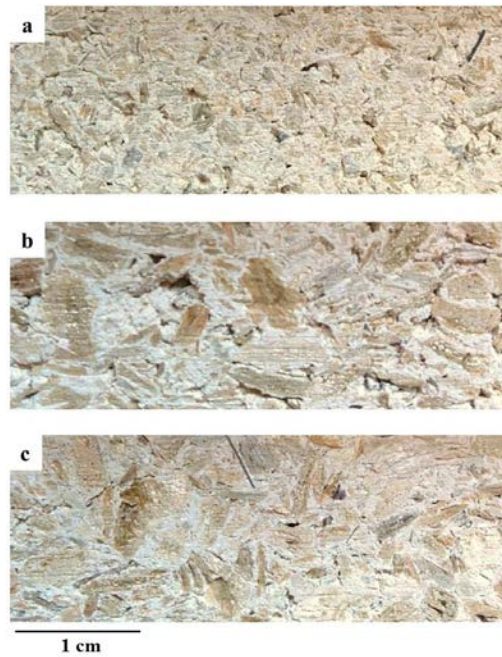


**Figure 6.3** High resolution photos of machined cross sections parallel to the casting direction of the samples: a) V2-Mk, b) V4-Mk and c) V4-Al [1].

The microstructural characterization, performed by SEM on the fracture surfaces, show the presence of geopolymer precipitates both in metakaolin-based (Fig. 6.4a, c, and d) and alumina-based (Fig. 4.9b and e) composites, confirming that the raw materials undergo a geopolymerization process. The precipitates belonging to alumina-based binders are coarser (about 100 nm, Fig. 6.4b) than the metakaolin-based ones (70–60 nm, Fig. 6.4a).  $\alpha\text{-Al}_2\text{O}_3$  is less reactive in the geopolymerization process [6] and only the alumina particles surface and/or hydrated species may react.

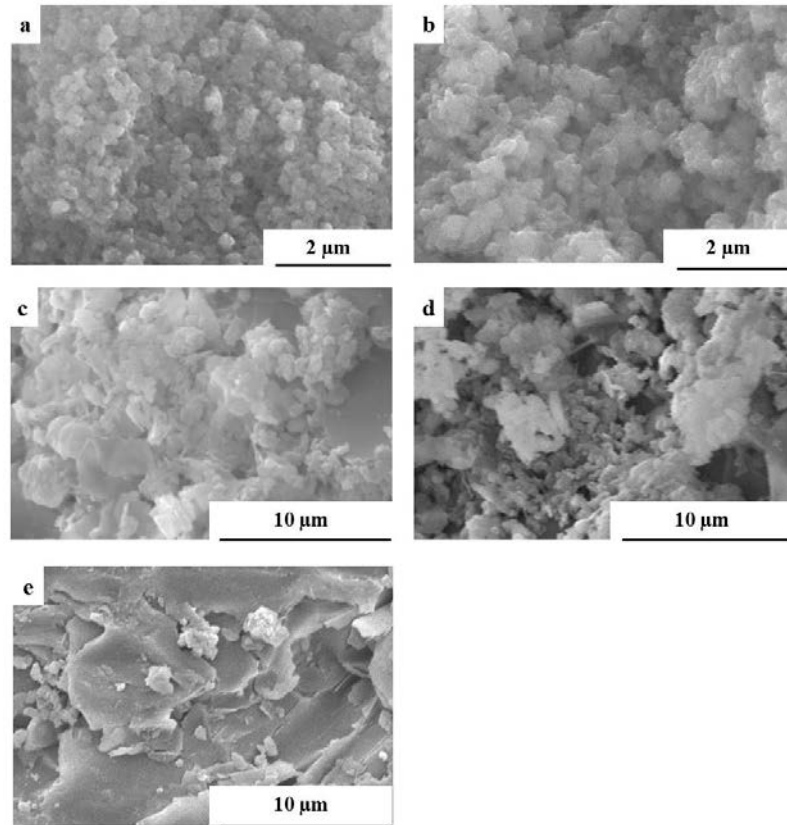


**Figure 6.4** SEM micrographs of a) metakaolin based and b) alumina based binders and fracture surfaces of the samples: c) V2-Mk, d) V4-Mk and e) V4-Al.

### 6.1.3.2 Stability in water

The stability in water of the expanded vermiculite–geopolymer panels was tested, after immersion in deionized water for 11 days, by measuring absorbed water and the weight loss after drying (Table 6.3).

All samples remain undamaged after the soaking in water. Maximum percentage of absorbed water (WS) is about 50 % and the weight loss is about 10 % for all the samples tested, showing that the different compositions used do not significantly affect the values. The high WS is due to the mesoporosity of the geopolymer binder [7-9] and the expanded structure of the vermiculite, that is able to absorb water between its plates [10]. The weight loss is mainly due to the dissolution of soluble phases [7], such as unreacted potassium silicate or alkali carbonates, and material loss (vermiculite layers breakage).

### 6.1.3.3 Porosity

Total open porosity in the range 0.0058–100  $\mu\text{m}$  was determined by Hg intrusion porosimetry. The pore size distributions are displayed in figure 6.5 and the total porosity, modal and median pore diameter are reported in Table 6.4. The results account mostly for the intrinsic porosity of the geopolymer matrix in the range 0.0058–1  $\mu\text{m}$  [11].

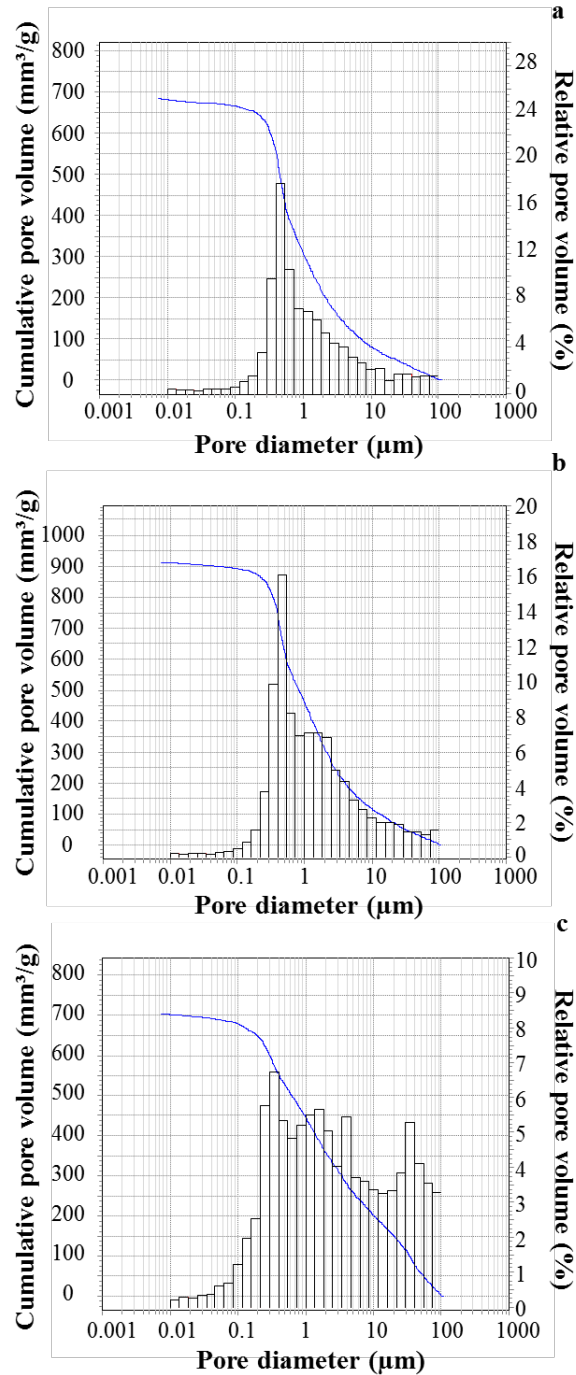


**Figure 6.5** Pore size distributions by Hg intrusion porosimetry of the samples: a) V2-Mk, b) V4-Mk, and c) V4-Al [1].

Metakaolin-based materials, V2-Mk and V4-Mk, present similar pore size distributions with about 50 % of accessible volume in both cases, due to pore size  $\leq 1 \mu\text{m}$ , with maximum frequency size peak located at  $\approx 0.46$  and  $0.41 \mu\text{m}$  (modal pore diameter), respectively. The use of the coarser vermiculite type 4 confers to sample V4-Mk the higher total pore volume. Sample V4-Al shows a continuous pore size distribution in the range  $0.2\text{--}100 \mu\text{m}$ , different from the other ones. Three different pores size ranges,  $< 1 \mu\text{m}$ ,  $1\text{--}10 \mu\text{m}$  and  $10\text{--}100 \mu\text{m}$ , contribute similarly to the total pore volume and beside the main frequency size peak, detected at  $\approx 0.30 \mu\text{m}$ , other peaks of frequency are evident. This wide range of pore sizes detected and the presence of big pores is due to the different microstructure of the alumina-based geopolymer binder, in which alumina particle cores remain as unreacted filler, packing within the vermiculite aggregates. The sample V4-Al shows the presence of big pores of size close to the upper limit of detection of the Hg porosimeter, explaining the measured low geometric density combined with a low pore volume.

**Table 6.4** Modal and median pore diameter and total pore volume obtained by Hg intrusion analysis.

Sample	Modal pore diameter ( $\mu\text{m}$ )	Median pore diameter ( $\mu\text{m}$ )	Total pore volume ( $\text{mm}^3 \text{g}^{-1}$ )
V2-Mk	0.46	0.82	684
V4-Mk	0.41	1.03	912
V4-Al	0.30	2.10	701

### 6.1.3.4 Thermal properties

#### 6.1.3.4.1 Phase modification as a function of the temperature

Panels were thermally treated at 600, 800, 1000 and 1200 °C in an electrical furnace in static air to assess phase modification as a function of the temperature. The mineralogical composition of the panels were evaluated by X-ray diffraction (XRD) before and after the thermal treatments (Fig. 6.6). To optimize the analysis conditions, fragments of all samples are selected and milled to obtain powders representative of the materials. The concept is to maintain the real character of the whole material starting from the panels (with an extremely randomized structure

and texture in which coexist large vermiculite platelets and fine geopolymer matrix) down to its average matrix/inclusions volume ratio.

In the XRD pattern of the not heat-treated V2-Mk (Fig. 6.6a), the presence of vermiculite is evident and results completely dehydrated and reduced to a micaceous structure ( $\sim 10 \text{ \AA}$ ). Quartz is probably presents as impurity of the metakaolin and/or vermiculite. Up to  $1000 \text{ }^\circ\text{C}$ , two micaceous phases, phlogopite and chlorite-vermiculite-smectite type, without interlayer or coordinated water are detected. At  $1000 \text{ }^\circ\text{C}$  the presence of enstatite is evident, while leucite just appears. Enstatite, leucite and quartz are the main phases in the sample treated at  $1200 \text{ }^\circ\text{C}$ .

V4-Mk shows the same phase evolution of V2-Mk, even if displays a lower degree of crystallinity. Vermiculite type 4, despite the industrial heat treatment of exfoliation, still exhibits an hydrated mineral phase showing a baseline reflection at  $14 \text{ \AA}$ . The reticular portions that have partially lost the water molecules [12] are present as reflections at  $11 \text{ \AA}$  and  $12 \text{ \AA}$ , although the presence of dehydrated vermiculite at  $10 \text{ \AA}$  is predominant. In V4-Al pattern (Fig. 6.6c) there is a constant presence of alumina revealed up to  $1200 \text{ }^\circ\text{C}$  without changes, while quartz impurity seems to disappear after the treatment at  $1000 \text{ }^\circ\text{C}$ . Vermiculite type 4 is completely reduced to a phyllosilicatic mica structure-type, due to an almost total dehydration by treatment at  $600 \text{ }^\circ\text{C}$ . Mica is still presents at  $1000 \text{ }^\circ\text{C}$ , but new mullite, leucite and a magnesium silicate-type  $\text{Mg}_2\text{SiO}_4/\text{MgSiO}_3$  phases are present at  $1200 \text{ }^\circ\text{C}$ .

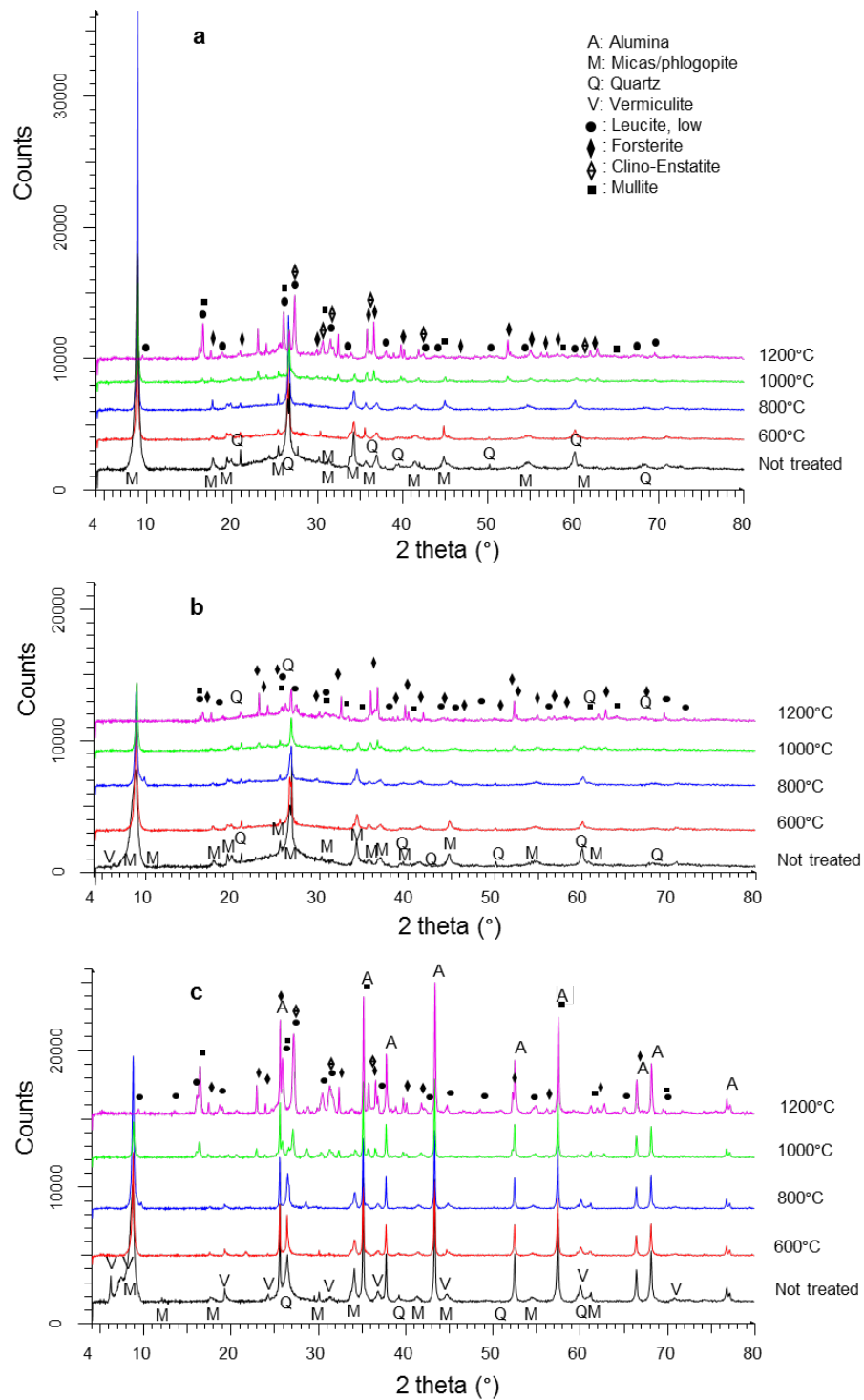


**Figure 6.6** X-Ray diffraction patterns of the panel: a) V2-Mk, b) V4-Mk and c) V4-Al, before and after the thermal treatments at 600, 800, 1000 and 1200 °C [1].

#### 6.1.3.4.2 Dilatometric analysis

Dilatometric characterization was performed up to 1200 °C in static air (heating rate 10 °C/min). Due to the dimensional constraints of the dilatometer specimen, that may do the results not representative of the composite materials, shrinkage and weight loss were also measured on the tiles with dimensions 10cm x 10cm x 2cm after thermal treatment at 1200 °C.

The weight loss and the shrinkage of the composite tiles are reported in Table 6.5. All the composites show a weight loss of about 9 % in agreement with the values obtained from the dilatometer specimens. Metakaolin-based composites present higher final shrinkages because in the alumina-based composites, alumina acts as refractory filler [13]. The presence of elongated aggregates aligned perpendicularly to the casting direction is responsible for the anisotropic shrinkages, higher in the thickness than in the side of the panels.

**Table 6.5** Weight loss ( $\Delta W\%$ ) and shrinkages of 10cm x 10cm x 2cm composite tiles after heating at 1200 °C; CTE values in the range 300-800 °C obtained after 1<sup>st</sup> and 2<sup>nd</sup> run in the dilatometric analysis.

Sample	$\Delta W\%$	Shrinkage $\Delta L/L_0$ %		CTE (300-800°C) $10^{-6} \cdot K^{-1}$	
		Side	Thickness	1 <sup>st</sup> run	2 <sup>nd</sup> run
V2-Mk	-9.0	-14.0	-1.0	17.8	10.6
V4-Mk	-9.0	-15.0	-8.0	12.3	9.7
V4-Al	-9.0	-2.0	-0.1	17.2	15.6

The dilatometric curves (1<sup>st</sup> and 2<sup>nd</sup> runs) and the CTE curves (referred to an initial temperature of 30 °C) of the composite materials and a geopolymer matrix used as a reference, are displayed in figure 6.7a and b, respectively. Composites show similar trends with a first zone of slight expansion up to 100 °C, followed by a contraction zone up to about 250 °C mainly due to the evaporation of the entrapped water. A new expansion occurs from  $\approx$  250 °C due to the expansion of vermiculite. All the samples reveal a thermal resistance up to 800 °C, after which the sintering due to viscous flow starts [14]. The dilatometric curves of the first run account for the relative amount of the geopolymer matrix and vermiculite particles (the volumetric percentage of vermiculite in the composite panel can be

estimated as 65 vol.% and 70 vol.%, respectively for V2-Mk and V4-Mk in the metakaolin-based composites.

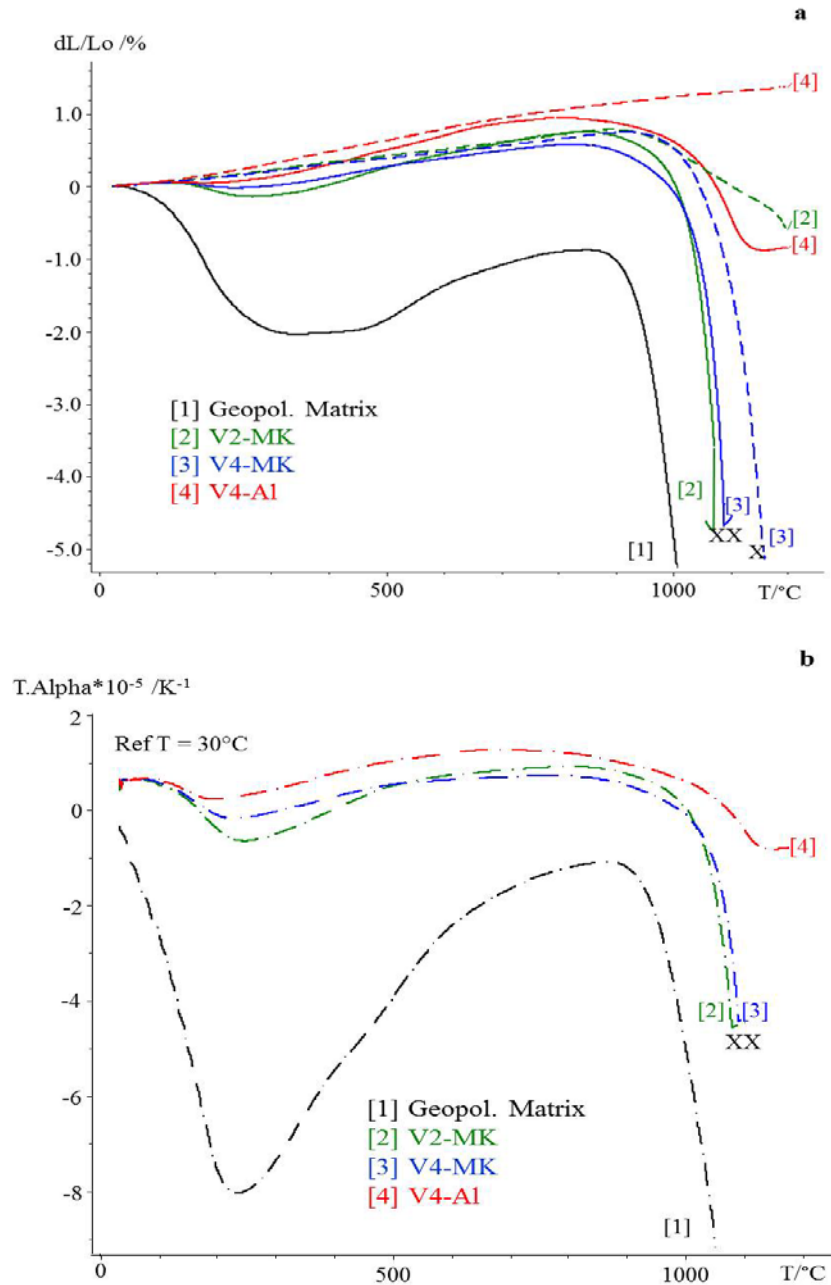


**Figure 6.7** Dilatometric analyses of the 1<sup>st</sup> and 2<sup>nd</sup> runs (dotted lines) on the samples V2-Mk, V4-Mk and V4-Al and geopolymers Mk matrix (a) and curves of the CTE values in the range (30-T °C) related to the 1<sup>st</sup> dilatometric run (b). The symbol X on the curves indicates that the shrinkage exceeds the detection range of the dilatometer [1].

In the curve of the geopolymer matrix the initial contraction is more pronounced, even if starting from about 300 °C it is possible to detect an expansion trend, while metakaolin-based composites show the dilatation of vermiculite along the whole curve. From the dilatometric analyses it is possible to observe that the composites present a very low linear dimensional change (< 1 %) up to 1000 °C for the presence of a thermal expansion mismatch between the contracting geopolymer matrix and the expanding vermiculite. The presence of vermiculite in the composites results in an improvement of the thermal stability; composites show the same shrinkage of the geopolymer matrix, but at higher temperature (for example metakaolin-based composite show a shrinkage of 4 % at around 1100 °C, i.e., 100 °C higher than in the geopolymer matrix).

Alumina-based composite shows a further increase of the dimensional stability at high temperature, with a 1 % of shrinkage at 60 °C higher temperature than metakaolin-based ones. The shrinkage of metakaolin-based composites exceeds the detection range of the dilatometer, but the curve trends are in agreement with the shrinkages values measured for the composites tiles after heating at 1200 °C and reported in Table 6.5. From the dilatometric analysis and the shrinkage values by heating at 1200 °C the metakaolin-based composites register higher shrinkages than alumina based one. The experimental values of CTE, in the range 300–800 °C, calculated from the dilatometric analysis of the composites, are reported in Table 6.5. The CTE are lower than the value detected for the metakaolin based matrix ( $22 \cdot 10^{-6} \text{ } ^\circ\text{C}^{-1}$ ), in agreement with the behavior of the dilatometric curves (Fig. 6.7a). The high temperature stability of the composites, demonstrated by the small dimensional changes reported in the curves and the CTE values, reflects in a lower risk of failure of the building elements since, as a general rule, lower thermal strain results in lower thermal stress [15].

In figure 6.7a, a second run up to 1200 °C highlighted by the dotted lines, shows the disappearance of the contraction zone due to the evaporation of water entrapped in the geopolymer binder and the presence of a continued expansion starting from 150 °C. The CTE values registered in the range 300–800 °C are about  $\sim 10 \cdot 10^{-6} \text{ } ^\circ\text{C}^{-1}$  for the samples V2–Mk and V4–Mk, and  $\sim 15 \cdot 10^{-6} \text{ } ^\circ\text{C}^{-1}$  for the samples V4–Al, being affected by the different compositions and phase transformation occurring during the thermal treatments. The viscous flow of the

metakaolin-based composites starts at higher temperature than in the first run for the presence of the crystalline phases formed during the first heating up. In sample V4–Al the expansion, during the second run, continues till the end of the measurement at 1200 °C (Fig. 6.7a); the higher thermal resistance of  $\alpha$ -Al<sub>2</sub>O<sub>3</sub> reduces the shrinkage and keeps the volume stable at high temperature [13].

#### **6.1.3.4.3 Thermal conductivity**

The thermal conductivity was measured with a heat flowmeter according to ASTM E1530 and UNI EN 12664 standards [16-17] and as reported in paragraph 3.2.19. The values of thermal conductivity and thermal resistance of the samples are reported in Table 6.6. A statistical analysis model [18] is used to determine the uncertainty associated with the conductivity measurements. The correlation between the density and the thermal conductivity of the samples is reported in figure 6.8. This experimental correlation allows to evaluate the performance of different samples and permits the comparison between different mixtures in terms of porosity dimension and distribution, that affect the thermal conductivity.

The use of vermiculite type 4 results in more dispersed density values compared to the samples prepared with vermiculite type 2. Sample V2–Mk has slightly higher thermal conductivity than V4–Mk. This is a typical phenomenon in building materials that show a wide spread of possible results at the same density level due to the porosity distribution and morphology [19].

The thermal conductivity of metakaolin-based geopolymers usually lies in the range 0.40–0.80 W·m<sup>-1</sup>·K<sup>-1</sup> [20], while values below 0.20 W·m<sup>-1</sup>·K<sup>-1</sup> are observed increasing the total porosity [21].

Metakaolin-based composites registered a thermal conductivity of 0.18–0.19 W·m<sup>-1</sup>·K<sup>-1</sup> (V2–Mk, V4–Mk). Since the thermal conductivity of pure alumina (corundum,  $\alpha$ -Al<sub>2</sub>O<sub>3</sub>) is about 33 W·m<sup>-1</sup>·K<sup>-1</sup> [22], the alumina-based sample (V4–Al) shows a higher conductivity value, 0.26 W·m<sup>-1</sup>·K<sup>-1</sup>.

**Table 6.6** Average thermal resistance and thermal conductivity of the panels.

Sample	Thermal resistance ( $\text{m}^2 \cdot \text{K} \cdot \text{W}^{-1}$ )	Thermal conductivity 10°C ( $\text{W} \cdot \text{m}^{-1} \cdot \text{K}^{-1}$ )
V2-Mk	2.643E-2	$0.189 \pm 0.003$
V4-Mk	3.360E-2	$0.178 \pm 0.003$
V4-Al	1.975E-2	$0.256 \pm 0.004$

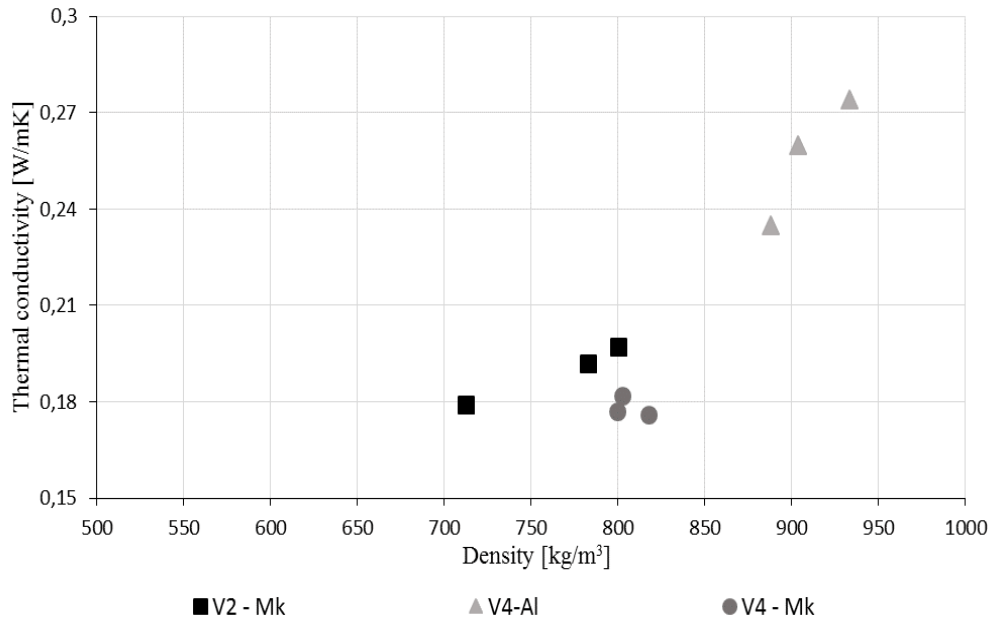


**Figure 6.8** Correlation between thermal conductivity and density for panels V2-Mk, V4-Mk and V4-Al [1].

### 6.1.3.5 Mechanical properties

#### 6.1.3.5.1 Flexural strength

A preliminary evaluation of flexural strength was performed on 10cm x 2cm x 2cm prisms, using a three-point jig and a cross-head speed of  $3 \text{ mm} \cdot \text{min}^{-1}$ . At least 5 prisms for each composite material were tested and the average values of flexural strength are reported in Table 6.7. The values of average flexural strength obtained for samples V2-Mk and V4-Al are similar and in the range of  $\approx 2.4$  MPa. Otherwise, sample V4-Mk possesses a lower value of 1.2 MPa. The mechanical properties of brittle materials are affected by the porosity amount and morphology [23-24]. It is known from the literature that the presence of expanded vermiculite aggregates, in lightweight concrete materials, increases the thermal insulation properties, but decreases the mechanical properties [25]. The higher

flexural strength of V2–Mk in comparison to V4–Mk and V4–Al may be attributed to the lower porosity and to a more homogenous structure. The expanded vermiculite aggregates may be considered as critical defects because they poorly stand the load [25] in comparison to the geopolymer binder. The presence of aggregates with smaller dimension, as in the case of vermiculite type 2, is useful to minimize the detrimental stress localization at the interface between matrix and aggregates. As a general trend, the presence of vermiculite helps to reduce the brittle behavior of the material under fracture, being able to dissipate the fracture energy as shown in figure 6.9a. These preliminary tests show that the values are analogous to those of other lightweight building materials with comparable densities, such as cellular concrete (< 1 MPa) or plaster board (~ 5 MPa).

**Table 6.7** Average flexural resistance ( $\sigma_f \pm \Delta\sigma$ ) and compressive strength ( $\sigma_c \pm \Delta\sigma$ ) for some composite samples.

Sample	Flexural strength $\sigma_f \pm \Delta\sigma$ (MPa)	Compressive strength $\sigma_c \pm \Delta\sigma$ (MPa)	
		//	⊥
V2-Mk	$2.4 \pm 0.3$	$2.0 \pm 0.2$	$3.1 \pm 0.3$
V4-Mk	$1.2 \pm 0.3$	$1.0 \pm 0.1$	$1.7 \pm 0.4$
V4-Al	$2.3 \pm 0.7$	$1.2 \pm 0.6$	$2.6 \pm 0.4$

### 6.1.3.5.2 Compressive strength

Preliminary compressive strength tests were performed on five cubic specimens (20 mm side) for each composition. The load was applied both perpendicular and parallel to the casting direction, using a cross-head speed of  $2 \text{ mm} \cdot \text{min}^{-1}$ .

The curves registered from the analysis, for the test parallel and perpendicular to the casting direction, are reported in figure 6.9b and 6.9c, respectively. The average values of compressive strength are reported in Table 6.7. The higher compressive strength values are registered for the sample V2–Mk in both directions, because of the lower porosity, previously investigated, and the size and aspect ratio of expanded vermiculite type 2, that generates a more homogenous structure. However, the anisotropic structure of the expanded vermiculite–geopolymer composites affects the properties and consequently the compressive

strength, measured parallel to the casting direction, shows lower values. In details, the decrease in parallel compressive strength is 35.5 %, 41.2 % and 53.8 % in V2-Mk, V4-Mk and V4-Al, respectively. The rupture of the sample, when the load is applied in the parallel direction, does not occur in catastrophic way (Fig. 6.9b), because it progressively involves the bridges among the thin plates and voids of the expanded vermiculite, that are mainly aligned perpendicularly to the load direction. Samples with vermiculite type 4 (V4-Mk and V4-Al) show a toughening effect, because the load remains constant after the failure, due to the dissipation of deformation energy. The values of compressive strength, registered with the load perpendicular to the casting direction, are higher, because the aggregates (as well as plates and voids) are parallel to the applied load and a lower void area is present under the loading surface. This is a consequence of the size effect on strength in brittle materials: the smaller is the volume under stress the higher is its fracture stress [23-24].

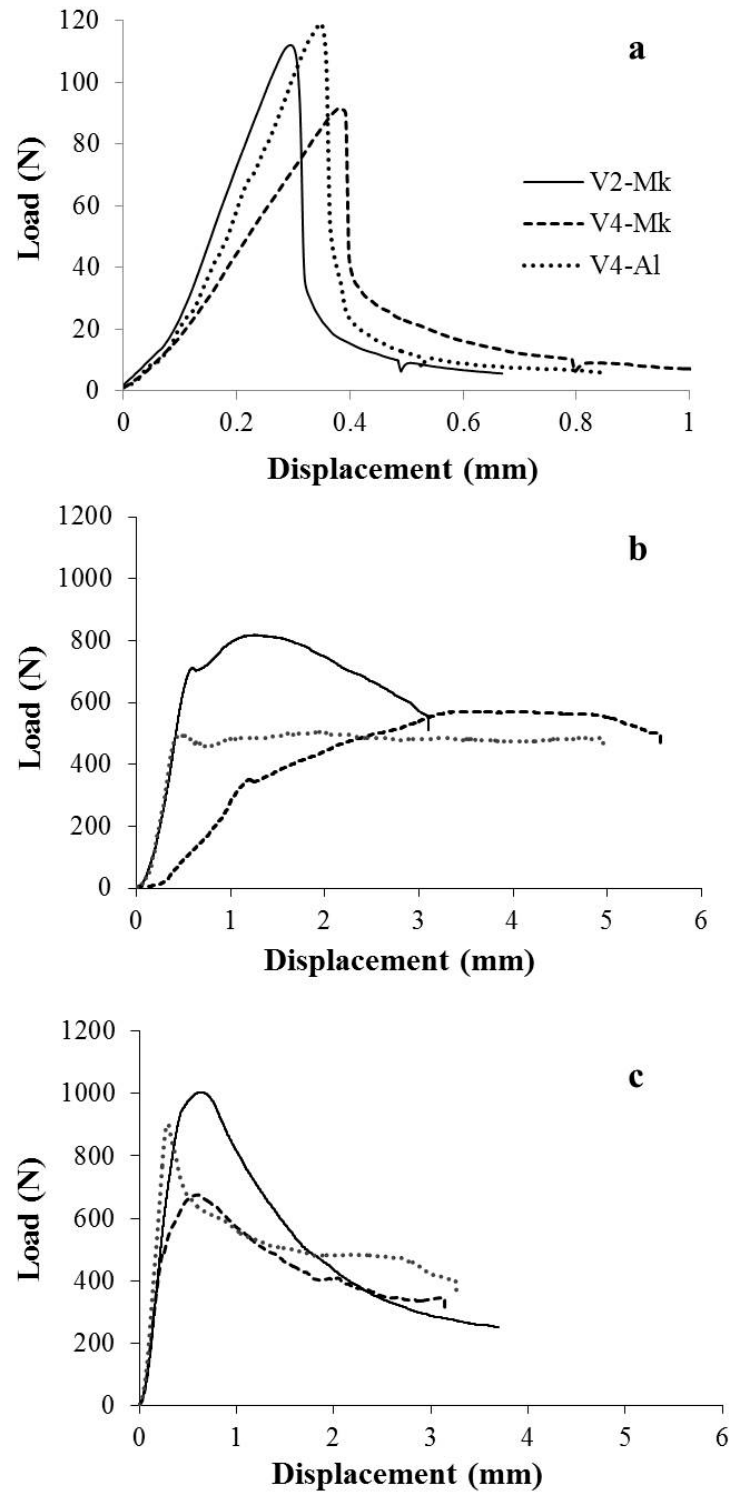


**Figure 6.9** Flexural analysis (a) and compressive strength parallel (b) and perpendicular (c) to the casting direction on the composite samples V2-Mk, V4-Mk and V4-Al [1].

## 6.2 Addition of reactive filler: silica-fume based foams

### 6.2.1 Introduction

The thermal resistance of the geopolymer materials [26] combined with the possibility to obtain lightweight structures exploiting the use of reactive fillers, have driven the research toward a preliminary production of composite foams designed for a range of thermo-acoustic insulating and fire-proofing applications. Many studies have been made on cellular or lightweight concrete materials [3, 27–32] in order to satisfy the sustainable development policies in buildings and constructions [33-35] and reduce the weight of the structure and the heat transfer, preserving operational energy [36]. The use of by-products and waste materials, combined with the choice of fast, simple and low temperature production processes to obtain the final insulating materials, are the main topics on which studies are focused on. Indeed, the research is addressed in finding low cost and “greener” way to produce this kind of materials.

Geopolymers are good candidate for this purpose, because they may be synthesized at low temperature and from a variety of starting aluminosilicate powders, that includes also waste materials as metallurgical slags and fly ashes [37]. In detail, in this work, geopolymer foams are produced using silica fume both as starting silicate powder and pore forming agent. Silica fume is a by-product derived from electric arc furnaces used in the manufacture of ferrosilicon or silicon metal. The fume which has a high content of very fine spherical particles, generally containing more than 90 % of SiO<sub>2</sub> mostly amorphous, is collected by filtering the gases escaping from the furnaces [38].

The impurities of free Si<sup>0</sup>, contained in silica fume, in the geopolymer alkali reaction medium give rise to the reaction reported in paragraph 2.7.2, with evolution of hydrogen and consequent foaming of the geopolymer slurry.

The aim of this work was to produce lightweight, low-cost material for insulating applications. Several starting compositions were tested to investigate how the use of different raw materials may affect the development of the porous structure in the foams. Geopolymer foams were synthesized using different mixtures of silica fume and metakaolin; in addition, the foaming of binders containing only silica fume have been studied. Potassium or sodium aqueous silicate solutions were

used as alkaline activators for all the foams. The best foams, selected on a trial and error approach, were widely characterized in terms of foam formation, macro and microstructure, porosity and thermal conductivity.

## **6.2.2 Experimental procedure**

### **6.2.2.1 Foam preparation**

The foams are produced by mixing magnetically and manually an alkaline solution with silica fume (Fds-foams) or with a mixture of silica fume and metakaolin powders (Mk-foams). The reaction medium is prepared dissolving NaOH (97.0 % purity) or KOH (85.7 % purity) pellets in commercial sodium (Si/Na = 1.71, 64.2 wt.% H<sub>2</sub>O) or potassium (Si/K = 1.75, 79.3 wt.% H<sub>2</sub>O) silicate by magnetic stirring, at 400 r.p.m., in Teflon molds.

The starting raw powders are silica fume (Ferropem Company, D<sub>50</sub> = 0.15 μm, Ssa = 30 m<sup>2</sup> g<sup>-1</sup>) and four metakaolins (M1000 (M1), M1200 (M2) provided by AGS Minéraux and Argicem blanc (M3) and rose (M4) supplied by Argicem).

The mixtures produced are cast in plastic molds with 5 cm diameter and several curing are applied to investigate the foaming process. The cast mixtures are left for 24 h in a heater at 70 °C to favor the H<sub>2</sub> formation, the foam expansion and the consolidation. In order to change the expansion and the consolidation rate the mold is closed in different ways as reported below.

- 24 h at 70 °C – open mold
- 24 h at 70 °C – cap mold with 5 holes
- 24 h at 70 °C – cap mold with 1 hole
- 24 h at 70 °C – half closed cap mold
- 24 h at 70 °C – open mold + 24h r.t. – closed mold

The schematic procedure adopted to obtain the final foams is reported in figure 6.10.

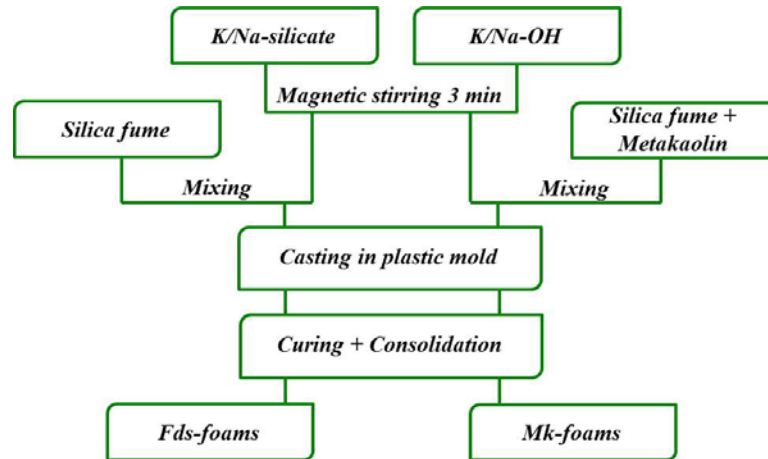


**Figure 6.10** Schematic process for the formation of silica-fume based foams.

### 6.2.2.2 Selection of the best foams

Twenty-nine different mixture compositions are formulated making little changes in the composition percentages of the starting raw materials. Each formulated mixture is subjected to more than one curing in order to assess the different expansion of the foam. Indeed, the foam volume expansion depends on the ratio between the surface of the foam exposed to air and the initial volume of the mixture [39].

The selection of the best foams is set on a macroscopic observation of the foamed structures obtained. The final process parameters are set to produce foams with slightly rounded top surfaces. Tight pore walls have to be formed to avoid the structural collapse under high  $H_2$  pressure and promote foaming expansion [40].

During the production of the foams many problems are encountered. The foaming process is affected by several parameters as the viscosity of the starting slurry, the reactivity of the starting raw materials, the consolidation and foaming rate generated by the closing way of the mold. All these parameters must be balanced in order to obtain a final compact and well foamed structure, with a quite homogeneous pore size distribution.

Stratified structures are observed when a non-homogeneous mixing of the starting slurry is obtained (Fig. 6.11a, b), while dense and poorly expanded structures are formed with highly viscous starting slurry (Fig. 6.11e). The increase of the viscosity is due to the high water demand of the metakaolin powder, thus, the silicate solution amount is often increased, during the formulation of the mixture composition, in order to improve the workability and the foaming of the slurry.

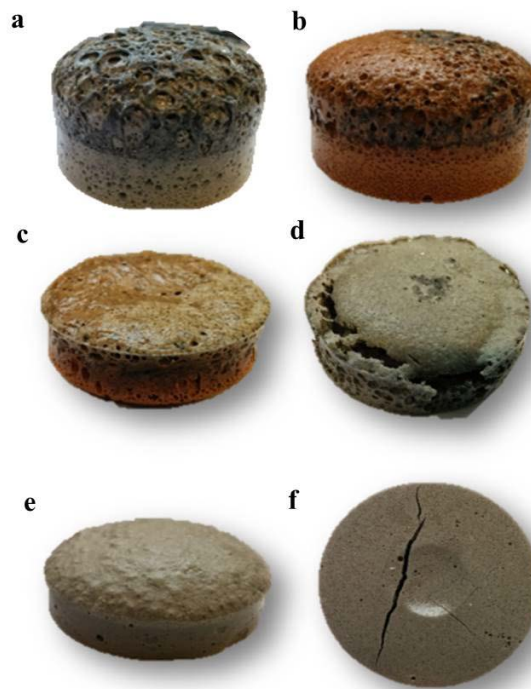


**Figure 6.11** Examples of not well foamed structures and encountered problems: stratified structures (a, b), foam with shrinkages (c) and cracks (d), dense and not foamed structure (e), foam broken in a half after three days (f).

The drying of the foams is another important parameter to take into account; a controlled evaporation of the water out of the pores is essential to prevent the formation and the propagation of cracks also over time. Some foams immediately show shrinkages and cracks due to a fast and not controlled evaporation of the water as a function of the curing adopted (Fig. 6.11c, d); other samples are well foamed and compact after the curing, but broken in a half after some days. This is probably due to a prolonged water evaporation, after the removal of the foam from the heater, that generates tensions and cracks in the sample, ending with the cracking of the foam after 2-3 days (Fig. 6.11f). To overcome this problem, some foams are extracted from the heater and left at r.t. in a closed mold to complete the consolidation by a slow evaporation of the water.

After several attempts, four foams, that shown a well expanded structure with a quite homogeneous distribution of the porosity, are selected to be characterized. The selected foams, the composition wt.%, the solid/liquid ratio and the curing adopted for the consolidation are reported in Table 6.8. After consolidation the foams are machined to obtain geometrical samples suitable for following

characterizations: the core section is selected due to its homogeneity, since the top consolidates faster, forming a thick and dense layer due to the surface tension and the temperature gradients during drying.

**Table 6.8** Sample code, composition (wt.%), solid/liquid ratio and curing of the selected foams.

Sample code	Composition (wt.%)				Solid/liquid ratio	Curing
	Metakaolin	Silica fume	M-Silicate	M-OH		
M4-Na	20.3	18.1	51.3	10.3	1.7	24 h at 70 °C – open mold + 24 h r.t. – closed mold
M1-K	20.3	18.1	51.3	10.3	1.5	24 h at 70 °C – open mold + 24 h r.t. – closed mold
Fds-Na	-	39.0	50.7	10.3	1.8	24 h at 70 °C – open mold
Fds-K	-	34.8	56.0	9.2	1.5	24 h at 70 °C – open mold

### 6.2.3 Characterization of the selected foams

#### 6.2.3.1 Infrared spectroscopy (FTIR-ATR)

FTIR-ATR spectroscopy is useful to investigate the foam formation as a function of time. The acquisition of the spectra is begun with the deposition of a drop of the reacting mixture on a diamond. Spectra are acquired every 10 min, for a total of 69 spectra, as reported as significant example in figure 6.12 for the sample Fds-K; to remove the atmospheric CO<sub>2</sub> contribution the spectra are corrected and normalized. In figure 6.13 the first and the last spectrum, acquired in continuous for all the foams, are reported.

The foam formation process is based on geopolymerization and contemporary foaming [41]. The first step is the dissolution of the starting raw powders by the alkaline solution. The species deriving from the hydrolysis then polymerize to form a solid network. The hydroxyl ions (OH<sup>-</sup>) supplied by the alkali activator increase the hydration rate by promoting the dissolution of aluminate and silicate present in the starting raw powders [42].

The band around 3300 cm<sup>-1</sup> is attributed to the stretching of the O-H water bound ( $\nu$  OH) and the band around 1650 cm<sup>-1</sup> to the water bending ( $\delta$  OH) [43]. The absorbance in these zones decreases as a function of the time for all the samples because of drying and consolidation of the materials, that lead to water

elimination. The K-based foams show a more evident decrease of the peak intensity, comparing the first and last spectra, due to the higher water content in the starting mixture (Table 6.8).

The constituents of all samples are essentially tetrahedral  $\text{SiO}_4$  and  $\text{AlO}_4$  with different structural order. The vibrations of the bonds, corresponding to the several phases present in the materials, can overlap, with formation of wide and imprecisely bands, also caused by the amorphous nature of the materials, resulting in a difficult interpretation of the results [44].

The band around  $1110\text{ cm}^{-1}$ , relative to the stretching of the Si-O-Si bond ( $\nu$  Si-O-Si), can be mainly attributed to the silica fume, since it is present in all the spectra of the foams. It is possible to observe that as a function of reaction time the intensity of this peak decreases, becoming a smoother shoulder in the final spectra, in agreement to the dissolution of the starting silica fume.

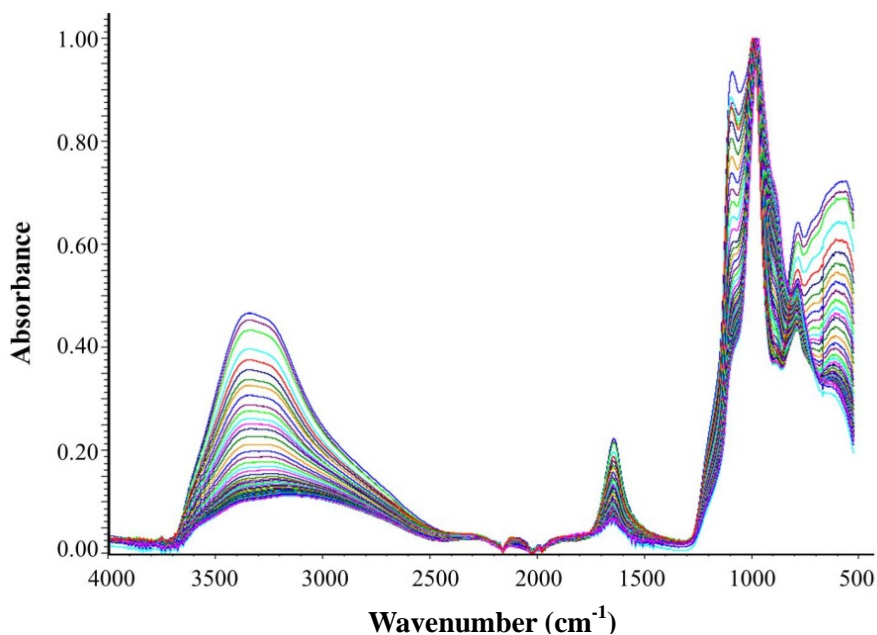


**Figure 6.12** Example of the 69 ATR-FTIR spectra acquired in continuos, every 10 minutes, for sample Fds-K.

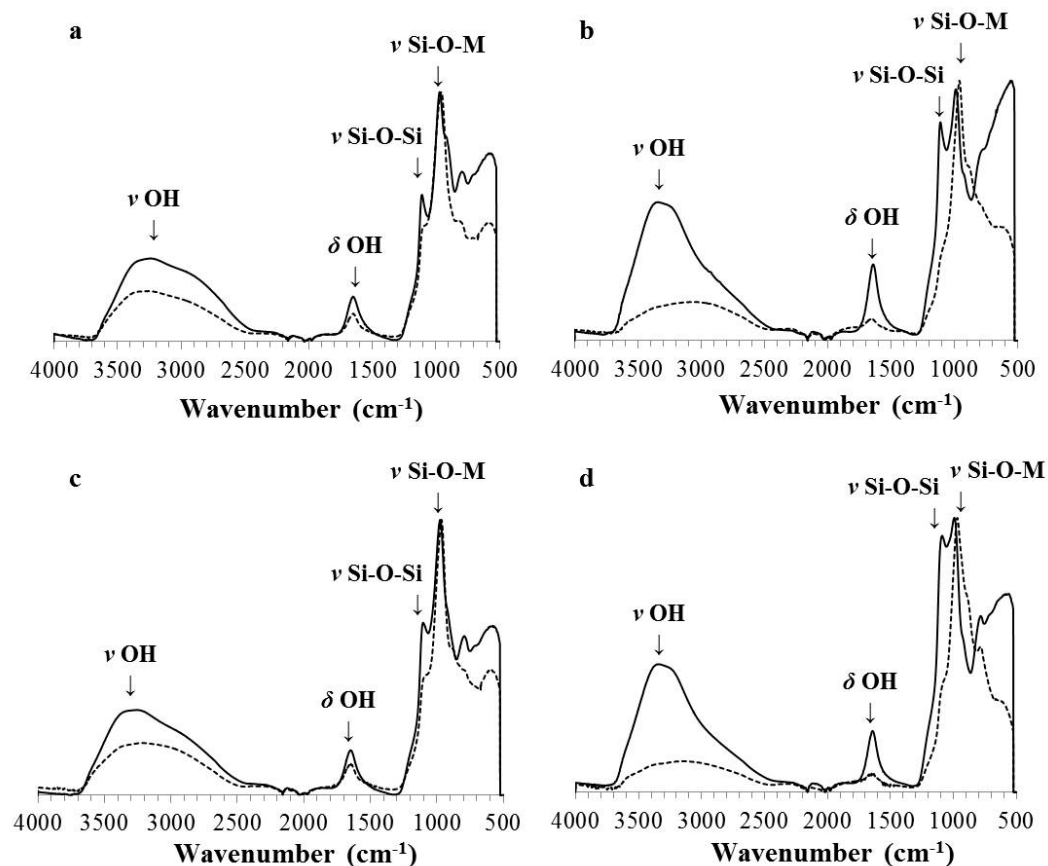


**Figure 6.13** FTIR spectra of the foams: a) M4-Na, b) M1-K, c) Fds-Na, d) Fds-K at the initial stage (dark line) and at the final stage (dotted line).

Between 1000 and 900  $\text{cm}^{-1}$  the Si-O-M bands (M= Si, Al, Na or K) are present [45]. For all the samples there is a modification of the band during the formation of the material, instead the position depends on the length and bending of the Si-O-M bond, thus justifying the shifts among the different samples.

The wavenumber evolution of the Si-O-M band, in function of time, is reported in figure 6.14 for all the foams. The displacement of the band, enclosed in the range 990-960  $\text{cm}^{-1}$ , is more or less noticeable in function of the sample. The initial band position may be explained by the presence of different amount of non-bridging oxygens, which results in different extent of depolymerization between the alkali solutions [46]. Na-based samples show the band initially positioned at lower wavenumber values, as evidence of an higher depolymerization of the alkali solution and of the presence of small and more reactive species.

The shift is more pronounced when potassium silicate is used as reactive medium;

Fds-K and M1-K present a shift of 24  $\text{cm}^{-1}$  and 28  $\text{cm}^{-1}$ , respectively, in comparison to lower shifts of 11  $\text{cm}^{-1}$  and 12  $\text{cm}^{-1}$  for Fds-Na and M4-Na. These pronounced shifts suggest a significant rearrangement of the Si-O-M bonds, due to the presence of more species in solution (Si-OH, Al-OH,  $\text{K}^+$ ) [47]. The higher shift of M1-K, in comparison with M4-Na, could be explained by a combination of Si-O-M bonds from dissolved species and the impurities present in the metakaolin composition, as evidenced in previous works [46-47]. The lower shift of M4-Na is due to the presence of reactive siliceous species, released from the depolymerized Na solution and ready to react; indeed monomeric silicate exchange faster with aluminosilicate species than with any other silicate anions [48].

The more depolymerized Na-solution determines the lower shift for Fds-Na, if compared with Fds-K; the reactivity of the alkaline solution is controlled by the amount of uncondensed species known to be more reactive than any other species [49]. In Na-based slurries fewer bonds require hydrolysis before the species can be released, determining a lowering of the shift.

Furthermore, the substitution of a  $\text{Si}^{4+}$  for a  $\text{Al}^{3+}$  involves the reduction of the T-O-T angle, and therefore the shift of the band to lower frequency, due to the smaller bonding force and for the longer Al-O bond compared to Si-O bond [44]. This fact may explain as the Mk-based foams show the final band positioned at lower values if compared with the Fds-foams, where only Si-O-Si bonds are present for the absence of Al ions.

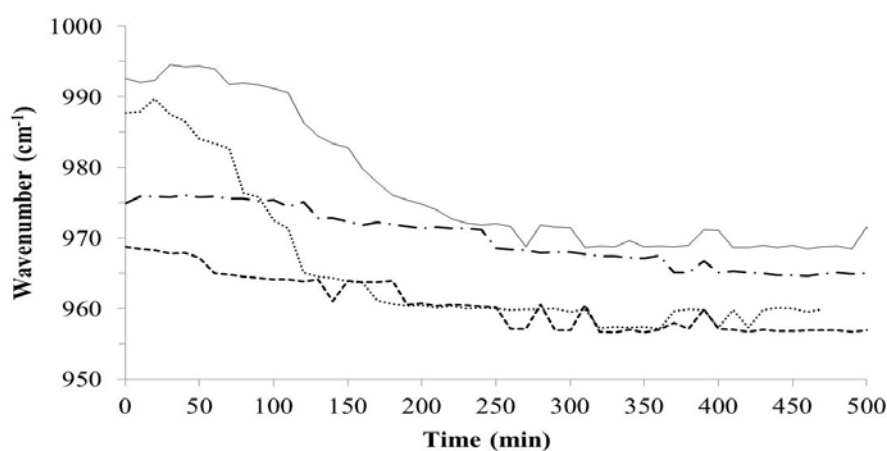


**Figure 6.14** Shift of the Si-O-M band, from IR spectra, versus time for M4-Na (-----), M1-K (.....), Fds-Na (- · -) and Fds-K (—) foams.

### 6.2.3.2 Macro- and microstructures of the foams

The curing of the samples at 70 °C favors the development of the H<sub>2</sub> bubbles, the increase of the viscosity and the consolidation of the foams. The balancing of these mechanisms allows to trap H<sub>2</sub> bubbles inside the structures and to create the porous foams [40, 50].

The real density ( $\rho_0$ ), the bulk density ( $\rho$ ), the total porosity ( $X_p$ ) and the volume expansion of the foams are reported in Table 6.9. The real densities varied in the range 2.2-2.4 g cm<sup>-3</sup>. K-based foams have higher  $\rho_0$  since the atomic mass of potassium is higher than that of sodium. All the foams present a low bulk density in the range 0.36 – 0.59 g cm<sup>-3</sup> and an high porosity from 75 to 85 %; an increase of the porosity percent is correlated to a decrease of the bulk density values, while no clear correlation is found to the volume expansion.

Images of the expanded structures and of the core sections of the foams are reported in figure 6.14a-d. All the samples show a macrostructure with roughly irregular spherical ultra-macropores deriving from the foaming process. The degree of reactivity of the starting powders, the viscosity and the homogeneity of the slurry affect the morphology of the pores (shape, diameter) and their distribution (regularity) [51].

Mk-foams show rounded pores (Fig. 6.15a, b), while pores with a more irregular shape and glossy surface are observed in Fds-foams (Fig. 6.15c-d). In particular, Fds-Na foams present domains of prolate pores spread in different directions (Fig. 6.15c). The foam expansion occurs mainly in the axial direction of the open cylindrical mould, due to gas escaping from the open top; the examination of the cross section, parallel to the axial direction, allows to determine whether expansion or structure collapse take place [40]. Instead, the pores morphology in the core section, parallel to the radial direction, accounts for the constrain of the cylindrical mold during the foaming process; the presence of randomly oriented pores with different shape indicates the inhomogeneity of the Fds-Na starting mixture, giving rise to a gradient of viscosity inside the foaming slurry.

**Table 6.9** Real density ( $\rho_0$ ), bulk density ( $\rho$ ), total porosity ( $X_p$ ) and volume expansion of the investigated foams.

Sample	$\rho_0$ ( $\text{g}\cdot\text{cm}^{-3}$ )	$\rho$ ( $\text{g}\cdot\text{cm}^{-3}$ )	$X_p$ (%)	Expansion (vol.%)
M4-Na	2.29	0.47	79	$248 \pm 21$
M1-K	2.38	0.59	75	$153 \pm 13$
Fds-Na	2.18	0.44	80	$197 \pm 25$
Fds-K	2.37	0.36	85	$220 \pm 7$



**Figure 6.15** Expanded structure and core section of the selected foams: a) M4-Na, b) M1-K, c) Fds-Na, and d) Fds-K.

The microstructures of the foams are shown in the SEM micrographs reported in figure 6.16. Mk-foams (Fig. 6.16a-b) show pore surfaces with precipitates due to geopolymerization (alumino-silicate hydrolysis and polycondensation reactions) [50] that occurs during the foam formation. Fds-foams (Fig. 6.16c-d) present smooth and glossy pore surfaces deriving from the alkali activation of the silica fume. Comparing the four microstructures, Fds-foams develop pores with a reduced inter-pore partitions. In Mk-foam slurries, the fine particles of silica fume adjust their positions to occupy the empty spaces between metakaolin particles and, due to the increasing number of contact points between solid particles, the cohesiveness of the slurry greatly improves [52] forming thicker pore walls and hampering the evolution of  $\text{H}_2$  bubbles. On the contrary, the presence only of silica fume, with low bulk density, allows the formation of thin pore walls and

high porosity. As a consequence, the total porosity is higher in Fds-foams than in Mk-foams.

Concerning Mk-foams, M1-K foams (Fig. 6.16b) develop big pores with large interpores partition formed by smaller pores. The higher reactivity of the potassium activating solution [53] speeds up the geopolymerization and the consolidation of the M1-K samples, stopping the foaming process and resulting in a broader pore size distribution (as discussed below) and in a lower foam expansion compared to M4-Na (Fig. 6.16a, Table 6.9).

Regarding Fds-foams, in Fds-K the microstructure is more homogenous than in Fds-Na, because of the lower solid/liquid ratio in the starting mixture (Table 6.8). Silica fume is highly reactive because of the small particles and the high specific surface area, but this leads to a high water demand poorly satisfied by the sodium activating solution. A gradient of viscosity is formed in the Fds-Na slurry, generating a less homogeneous microstructure.

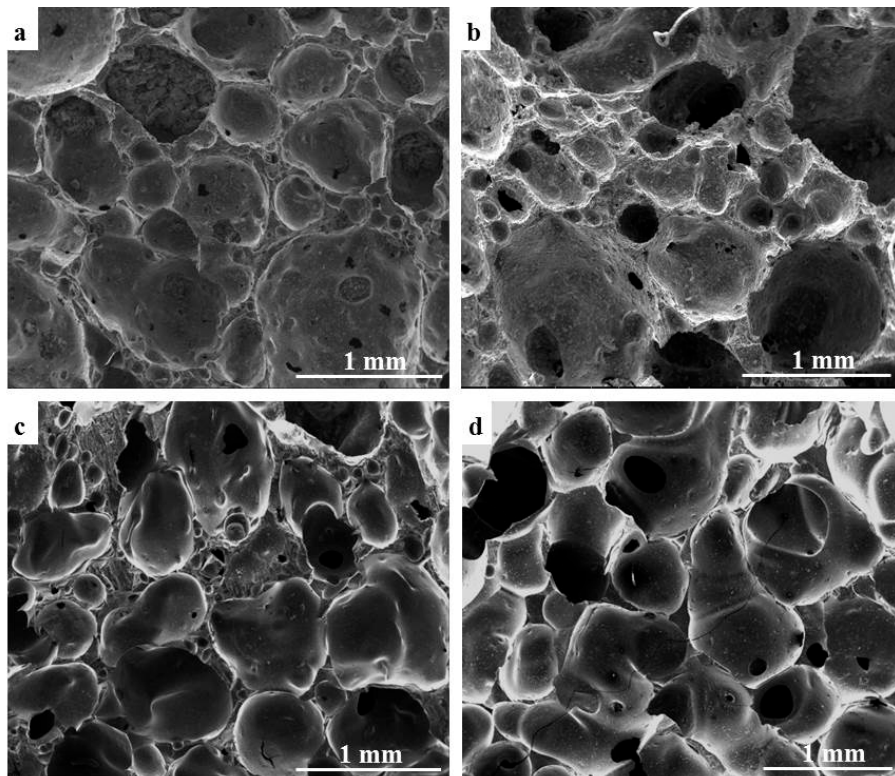


**Figure 6.16** SEM micrographs of the foams: a) M4-Na b) M1-K c) Fds-Na, and d) Fds-K.

### 6.2.3.3 Analysis of the porosity

#### 6.2.3.3.1 Pore size distribution (0.0058-100 $\mu\text{m}$ range) obtained by Hg intrusion porosimetry

The pore size distribution in the range 0.0058-100  $\mu\text{m}$  was investigated by Hg intrusion porosimetry (MIP) and displayed in figure 6.17. Accessible porosity, maximum frequency diameter ( $D_{\text{maxf}}$ ) and total pore volume are reported in Table 6.10. The results mainly account for the accessible small pores deriving from the alkali activation and polycondensation reaction of the material and for the ultra-macropores induced by the foaming process, that are difficult to quantify by image analysis. Wide and scattered pore size distributions are detected for all samples, with the exception of the almost monomodal pore size distribution of M4-Na, having the most frequent size peak located at 18  $\mu\text{m}$  (Fig. 6.17a). M1-K foams present the broadest pore size distribution, since the reaction synthesis is sped up and a fast consolidation occurs. Among the pore size distribution the maximum frequency peak is located at 34  $\mu\text{m}$ . Fds-foams show a maximum frequency diameter located at 14  $\mu\text{m}$  for Fds-Na and at 86  $\mu\text{m}$  for Fds-K.

**Table 6.10** Accessible porosity, maximum frequency diameter ( $D_{\text{maxf}}$ ) and total pore volume calculated from Hg intrusion porosimetry.

Sample	Accessible porosity (%)	$D_{\text{maxf}}$ ( $\mu\text{m}$ )	Total pore volume ( $\text{mm}^3\cdot\text{g}^{-1}$ )
M4-Na	62	18	729
M1-K	50	34	493
Fds-Na	59	14	706
Fds-K	50	86	495

The higher alkalinity of K-based silicate solution favors the redox reaction of silicon, resulting in the formation of bigger pores in foams M1-K and Fds-K.

M4-Na and Fds-Na have similar accessible porosity (about 60 %) in agreement with the similar pore total volume fraction (about 80 %). As well, K-based foams have similar accessible porosity ( $\approx 50$  %), but with a discrepancy in the pore total volume fraction (85 % in Fds-K and 75 % in M1-K).

In general, Na-based foams show an higher total pore volume intruded that

confirm the higher values of accessible porosity registered and the formation of pores with maximum frequency located at lower diameter values.

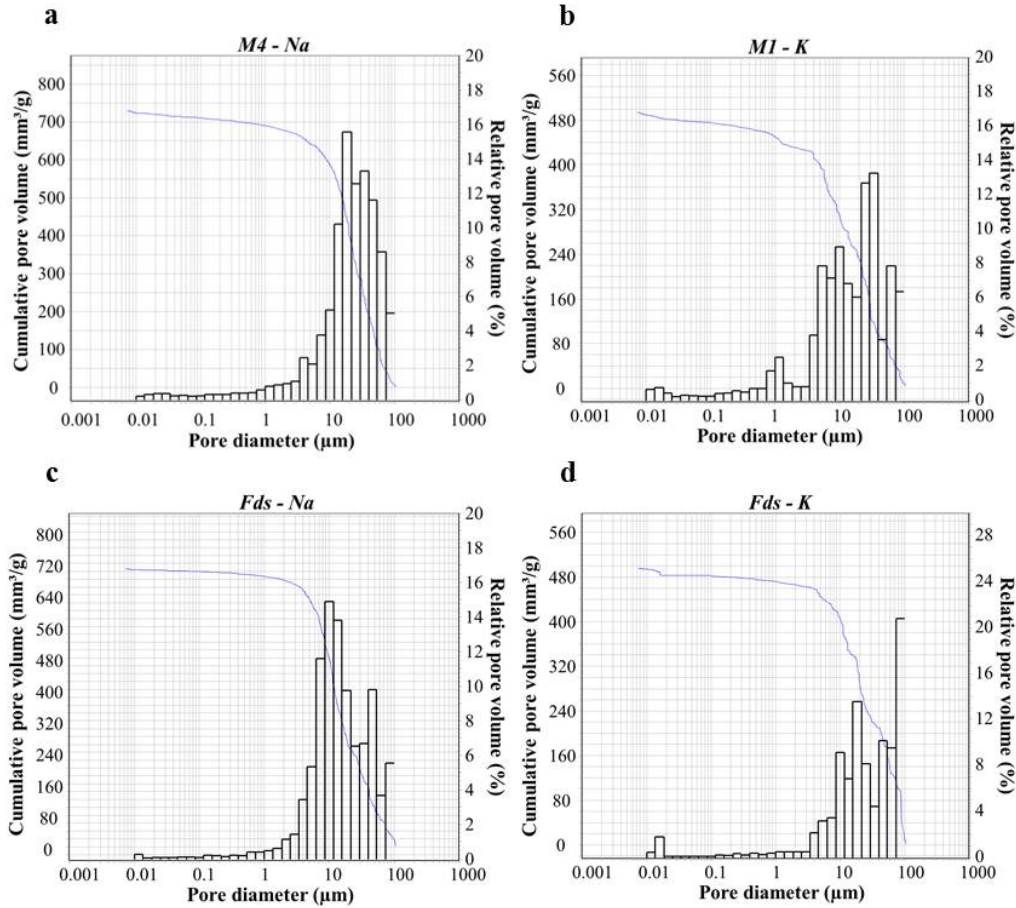


**Figure 6.17** Pore size distributions, obtained by Hg intrusion porosimetry (MIP), of the foams: a) M4-Na, b) M1-K, c) Fds-Na, and d) Fds-K.

### 6.2.3.3.2 Ultra-macropores size distribution (100-3100 $\mu\text{m}$ range) obtained by image analysis

The ultra-macropores size distributions in the range 100-3100  $\mu\text{m}$  (Fig. 6.18) were obtained by image analysis of high resolution photos of the foam core sections. The higher frequency of the pores is concentrated in the range 100-1500  $\mu\text{m}$ , but some random big pores, with dimensions up to 3100  $\mu\text{m}$ , may be found.

The distributions have similar trends, with the exception of sample M1-K (Fig. 6.18b). Foam M1-K displays an irregular distribution, also found in MIP analysis (Fig. 6.18b) attributable to the low viscosity of the slurry, that favors the evolution and coalescence of  $\text{H}_2$ -bubbles, but also to the fast consolidation of the mixture

that hampers the foaming process. An estimation of the ultra-macroporosity, with pores bigger than 100  $\mu\text{m}$ , may be done subtracting the accessible porosity detected by MIP to the total porosity ( $X_p$ ). Na-based foams have similar ultra-macroporosity around 20 % while Fds-K and M1-K present an ultra-macroporosity of 35 and 25 %, respectively.

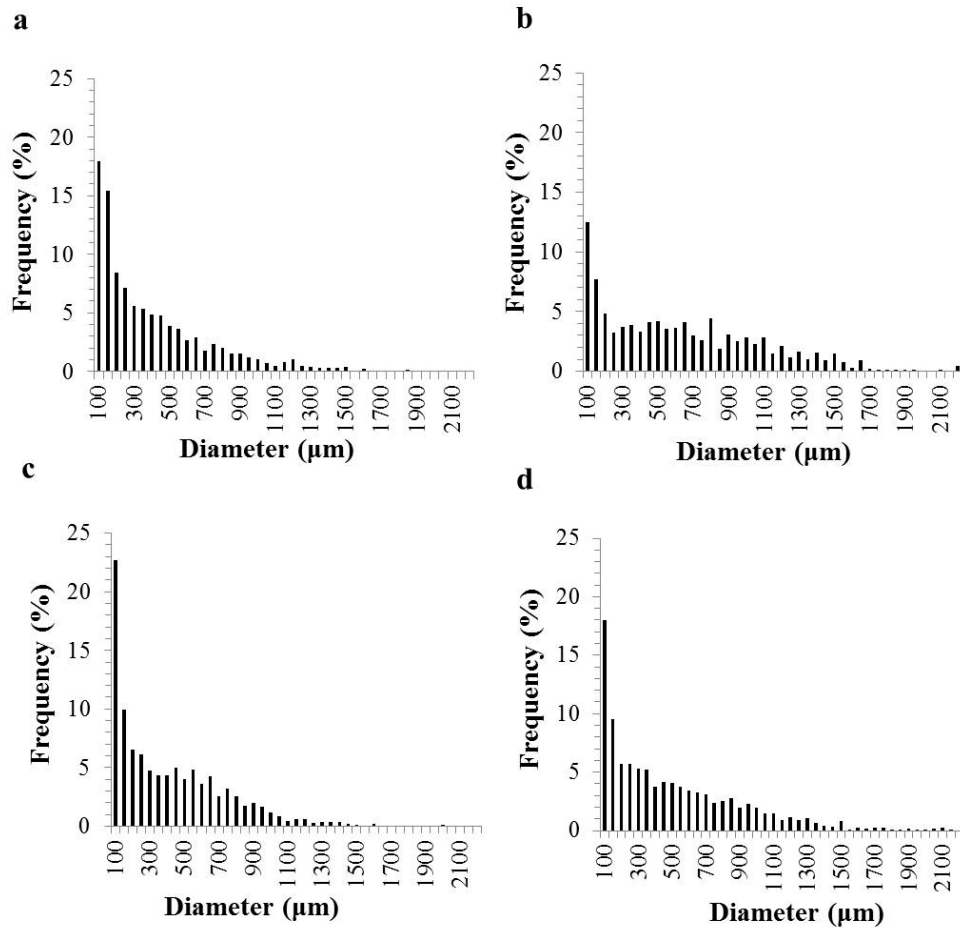


**Figure 6.18** Pore size distributions obtained by image analysis of the foams: M4-Na (a), M1-K (b), Fds-Na (c), and Fds-K (d).

Three main pores size ranges may be identified in the ultra-macropore size distributions: pores in the range 100-300  $\mu\text{m}$ , 300-700  $\mu\text{m}$  and pores bigger than 700  $\mu\text{m}$ ; the percentages of these selected intervals as a function of the estimated percentages of ultra-macroporosity are shown in figure 6.19.

K-based foams develop slightly bigger pores. Since K-based mixtures have lower solid/liquid ratio (Table 6.8), a higher amount of water decreases the initial viscosity of the slurries and  $\text{H}_2$  may easily evolve through the mixture, forming

big bubbles. Moreover, the higher alkalinity of the potassium activating solution favors the silicon reaction, namely  $H_2$  production [54]. For this reason, the lower solid/liquid ratio and the lower viscosity of K-based foams enable pores coalescence resulting in the higher percentage of pores over  $700\ \mu\text{m}$  ( $\approx 10\%$ ) (Fig. 6.19b, d).

Since Na-based foams present an higher starting viscosity of the mixtures, due to the higher solid/liquid ratio, the internal bubble pressure is not enough to generate big pores and the percentage of pores over  $700\ \mu\text{m}$  decreases to  $\approx 3\text{-}4\%$  (Fig. 6.19a, c).

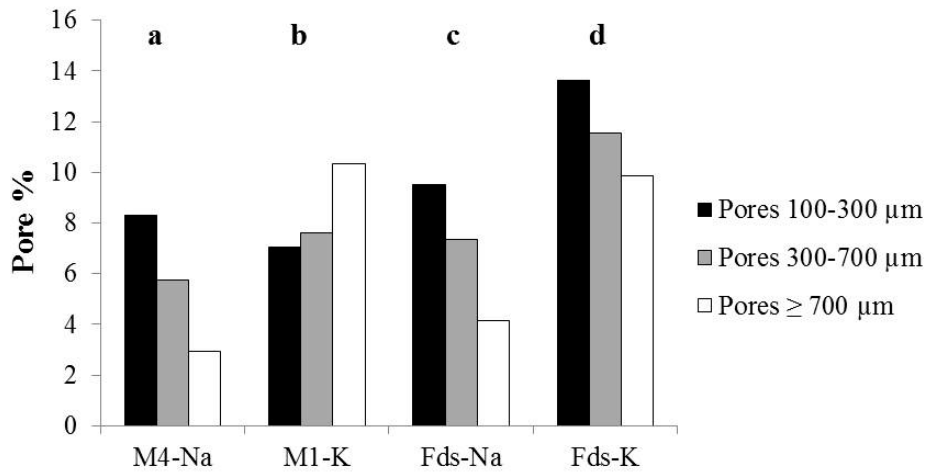


**Figure 6.19** Foams pore percentages in the range  $100\text{-}300\ \mu\text{m}$ ,  $300\text{-}700\ \mu\text{m}$  and  $\geq 700\ \mu\text{m}$  as a function of the total ultra-macroporosity percent of the foams: a) M4-Na, b) M1-K, c) Fds-Na, and d) Fds-K.

#### 6.2.3.4 Thermal conductivity

The average thermal conductivity values obtained for the foams are reported in Table 6.11. Foams Fds-K show the lowest thermal conductivity value of  $0.12\ \text{W m}^{-1}\ \text{K}^{-1}$ , while M1-K display the highest one ( $0.173\ \text{W m}^{-1}\ \text{K}^{-1}$ ). Na-based foams register the same thermal conductivity value ( $0.169\ \text{W m}^{-1}\ \text{K}^{-1}$ ).

Thermal conductivity values may be correlated to the total porosity percent achieved after the foaming process; in fact, the thermal conductivity decreases with the increase of the porosity percent (Table 6.11).

Foams Fds-K show the lowest thermal conductivity due to the highest porosity

(85 %) and the homogeneity of the porous microstructure. An increase of the porosity leads to an improvement of the lightweight of the matrix, decreasing the interpores space and the volume of skeleton that may accumulate heat [24]. As the development of a good porosity is associated to the viscosity of the starting mixture, the thermal conductivity is affected by the reactivity and workability of the starting slurry. Therefore, the low thermal conductivity of the Fds-K foams depends on the higher reactivity of the starting mixture, such as observed in the FTIR-ATR analysis, and on the good balancing of the reactions that occur during the foaming process.

The same thermal conductivity values registered for Na-based foams ( $0.169 \text{ W m}^{-1} \text{ K}^{-1}$ ) account of all similarities observed in the pore size distributions. Indeed, Na-based foams show almost the same values of pore total volume fraction, accessible porosity registered by MIP (Table 6.10) and the same trends in the pore size distributions registered by MIP (Fig. 6.17) and image analysis (Fig. 6.18).

The irregular pore size distribution, the lowest expansion and pore total volume fraction, found for the foams M1-K, affect the thermal conductivity of the material, that displays the highest value.

Nevertheless, the values obtained classify the foams as potential good insulator materials, being lower or comparable with other insulating materials, as, for example, cellular concrete ( $0.16\text{-}0.33 \text{ W m}^{-1} \text{ K}^{-1}$ ) [52].

**Table 6.11** Bulk density ( $\rho$ ), total porosity ( $X_p$ ) and thermal conductivity of the selected foams.

Sample	$\rho$ ( $\text{g}\cdot\text{cm}^{-3}$ )	$X_p$ (%)	Thermal conductivity ( $\text{W}\cdot\text{m}^{-1}\text{K}^{-1}$ )
M4-Na	0.47	79	0.169
M1-K	0.59	75	0.173
Fds-Na	0.44	80	0.169
Fds-K	0.36	85	0.120

### 6.3 Conclusions

The work carried out do possible to identify suitable mixtures for the production of composite geopolymers. The use of a geopolymer binders allows to exploit the chemical consolidation at low temperature avoiding the use of high temperatures during the production process.

The introduction of lightweight aggregates improves the heat-insulating properties of the starting matrices and decreases the overall density of the composites, showing properties comparable with other lightweight or cellular materials. The selected composite mixtures result suitable for a scale-up process to produce big panels, being easily cast in mold with big dimension, due to the good workability. The combination of thermal and mechanical properties, obtained from the various analyses, suggests that these composite materials may be used for the production of pre-cast high-temperature insulating panels, suitable to be mechanically anchored to a load-bearing structure. However, a detailed feasibility analysis should be done to find the most suitable industrial process, time and cost-effective, in respect of the final product and intended use.

The use of silica fume as reactive filler shows as highly porous geopolymer foams may be produced thanks to the presence of free metal silicon that in alkaline environment generates  $H_2$  gas. The increase of the viscosity during the consolidation of the foams permits to entrap the  $H_2$  bubbles inside the structures creating the final porous structures. The reactivity of the starting mixture and the linked homogeneity greatly affect the development of the final porous structures and the related insulating properties of the materials.

The low bulk densities and the good thermal conductivity values do the produced composite materials really promising as insulating materials. Further characterizations, as mechanical tests, need to be performed to better asses the properties of the foams for application, for example, in building and construction sectors. Furthermore, the foaming process must be improved to apply the materials on big scale for the production of samples with different shape and geometry.

## References

- [1] V. Medri, E. Papa, M. Mazzocchi, L. Laghi, M. Morganti, J. Francisconi, E. Landi, Production and characterization of lightweight vermiculite/geopolymer-based panels, *Mater. Des.* 85 (2015) 266–274.
- [2] F.S. Rostasy, Changes of pure structure of cement mortars due to temperatures, *Cement Concrete Res.* 10 (1980) 157–164.
- [3] S.M.A. El-Gamal, F.S. Hashem, M.S. Amin, Thermal resistance of hardened cement pastes containing vermiculite and expanded vermiculite, *J. Therm. Anal. Calorim.* 109 (2012) 217–226.
- [4] S.A. Suvorov, V.V. Skurikhin, Vermiculite — a promising material for high temperature heat insulators, *Refract. Ind. Ceram.* 44 (2003) 186–193.
- [5] H. Rahier, J. F. Denayer, B. Van Mele, Low-temperature synthesized aluminosilicate glasses. Part IV Modulated DSC study on the effect of particle size of metakaolinite on the production of inorganic polymer glasses, *J. Mater. Sci.* 38 (2003) 3131–3136.
- [6] N.F.Nagem, M.A.S. Costa, V.G. Silva, A.B. Henriques, A.A. Mansur, A.E. Peres, H.S. Mansur, Alumina superfines based geopolymers: developments and characterization. In: *Characterization of Minerals, Metals, and Materials 2015*, J.S. Carpenter, C. Bai, J.P. Escobedo-Diaz, J.-Y. Hwang, S. Ikhmayies, B. Li, J. Li, S. Neves Monteiro, Z. Peng, M. Zhang (Eds.), Wiley - TMS (2015) 325–335.
- [7] E. Papa, V. Medri, E. Landi, B. Ballarin, F. Miccio, Production and characterization of geopolymers based on mixed compositions of metakaolin and coal ashes, *Mater. Des.* 56 (2014) 409–415.
- [8] K. Okada, A. Ooyama, T. Isobe, Y. Kameshima, A. Nakajima, K.J.D. MacKenzie, Water retention properties of porous geopolymers for use in cooling applications, *J. Eur. Ceram. Soc.* 29 (2009) 917–923.
- [9] V. Medri, E. Landi, Recycling of porcelain stoneware scraps in alkali bonded ceramic composites, *Ceram. Int.* 40 (2014) 307–315.
- [10] K. Okada, S. Matsui, T. Isobe, Y. Kameshima, A. Nakajima, Water-retention properties of porous ceramics prepared from mixtures of allophane and vermiculite for materials to counteract heat island effects, *Ceram. Int.* 34 (2008) 345–350.
- [11] E. Landi, V. Medri, E. Papa, J. Dedecek, P. Klein, P. Benito, A. Vaccari,

Alkali-bonded ceramics with hierarchical tailored porosity, *Appl. Clay Sci.* 73 (2013) 56–64.

[12] C. Marcos, Y.C. Arango, I. Rodriguez, X-ray diffraction studies of the thermal behavior of commercial vermiculites, *Appl. Clay Sci.* 42 (2009) 368–378.

[13] T.S. Lin, D.C. Jia, P.G. He, M.R. Wang, Thermo-mechanical and microstructural characterization of geopolymers with  $\alpha$ -Al<sub>2</sub>O<sub>3</sub> particle filler, *Int. J. Thermophys.* 30 (2009) 1568–1577.

[14] J.L. Bell, P.E. Driemeyer, W.M. Kriven, Formation of Ceramics from Metakaolin-Based Geopolymers. Part II: K Based Geopolymer, *J. Am. Ceram. Soc.* 92 (2009) 607–15.

[15] L. Zuda, R. Cerny, Measurement of linear thermal expansion coefficient of alkaliactivated aluminosilicate composites up to 1000 °C, *Cement Concrete Comp.* 31 (2009) 263–267.

[16] ASTM, E1530-11, Standard Test Method for Evaluating the Resistance to Thermal Transmission of Materials by the Guarded Heat Flow Meter Technique, ASTM International, West Conshohocken PA (USA), 2011.

[17] UNI EN 12664, Thermal Performance of Building Materials and Products — Determination of Thermal Resistance by Means of Guarded Hot Plate and Heat Flow Meter Methods — Products of Low and Medium Thermal Resistance, UNI Ente Nazionale Italiano di Unificazione, Milano,(I), 2012.

[18] L. Laghi, F. Pennechi, G. Raitieri, Uncertainty analysis of thermal conductivity measurements in materials for energy-efficient buildings, *Int. J. Metrol. Quality Eng.* 2 (2011) 141–151.

[19] M. Labanti, L. Laghi, Design thermal values determination of building elements according to EN 1745. Part I: description and critical analysis of the proposed methodology, *L'Industria Laterizi* 118 (2009) 258 -272.

[20] P. Duxson, G.C. Lukey, J.S.J. van Deventer, Thermal conductivity of metakaolin geopolymers used as a first approximation for determining gel interconnectivity, *Ind. Eng. Chem. Res.* 45 (2006) 7781–7788.

[21] E. Kamseu, B. Nait-Ali, M.C. Bignozzi, C. Leonelli, S. Rossignol, D.S. Smith, Bulk composition and microstructure dependence of effective thermal conductivity of porous inorganic polymer cements, *J. Eur. Ceram. Soc.* 32 (2012) 1593–1603.

- [22] E. Gregorová, W. Pabst, Z. Sofer, O. Jankovský, J. Matějček, Porous alumina and zirconia ceramics with tailored thermal conductivity, *JPCS* 395 (2012) 012022.
- [23] J.B. Wachtman, W.R. Cannon, M.J. Matthewson, Mechanical Properties of Ceramics, 2nd ed. Wiley, Hoboken NJ (USA), 2009.
- [24] R.W. Rice, Evaluation and extension of physical property-porosity models based on minimum solid area, *J. Mater. Sci.* 31 (1996) 102–118.
- [25] F. Koksál, O. Gencil, M. Kaya, Combined effect of silica fume and expanded vermiculite on properties of lightweight mortars at ambient and elevated temperatures, *Constr. Build. Mater.* 88 (2015) 175–187.
- [26] V.F.F. Barbosa, K.J.D. MacKenzie, Thermal behaviour of inorganic geopolymers and composites derived from sodium polysialate, *Mater. Res. Bull.* 38(2) (2003) 319–331.
- [27] K. Ramamurthy, E.K. Kunhanandan Nambiar, G. Indu Siva Ranjani, A classification of studies on properties of foam concrete, *Cement Concrete. Comp.* 31 (2009) 388–396.
- [28] M.A. Othuman, Y.C. Wang, Elevated-temperature thermal properties of lightweight foamed concrete, *Constr. Build. Mater.* 25 (2011) 705–716.
- [29] M.A.O. Mydin, Y.C. Wang, Mechanical properties of foamed concrete exposed to high temperatures, *Constr. Build. Mater.* 26 (2012) 638–654.
- [30] Z. Zhang, J.L. Provis, A. Reid, H. Wang, Geopolymer foamconcrete: an emerging material for sustainable construction, *Constr. Build. Mater.* 56 (2014) 113–127.
- [31] V. Vaou, D. Panias, Thermal insulating foamy geopolymers from perlite, *Miner. Eng* 23 (2010) 1146–1151.
- [32] G. Bumanis, D. Bajare, A. Korjakins, Mechanical and thermal properties of lightweight concrete made from expanded glass, *JSACE* 2 (2013) 26–32.
- [33] M.C. Bignozzi, Sustainable cements for green buildings construction, *Procedia Eng.* 21 (2011) 915–921.
- [34] K.A. Komnitsas, Potential of geopolymer technology towards green buildings and sustainable cities, *Procedia Eng.* 21 (2011) 1023–1032.
- [35] J.W. Phair, Green chemistry for sustainable cement production and use, *Green Chem.* 8 (2006) 763–780

- [36] S. Pullen, Energy used in the construction and operation of houses, *Archi. Sci. Rev.* 43(2000) 87–94.
- [37] J.S.J. van Deventer, J.L. Provis, P. Duxson, D.G. Brice, Chemical Research and Climate Change as Drivers in the Commercial Adoption of Alkali Activated Materials, *Waste Biomass Valor.* 1 (2010) 145–155
- [38] V.M. Malhotra, Silica fume a pozzolan of new interest for use in some concretes, *Concrete and Construction* May 1982
- [39] E. Kamseu, E. Landi, Geopolimeri e materiali porosi, in Geopolimeri: polimeri inorganici chimicamente attivati, C. Leonelli, M. Romagnoli, Lulu.com (2011) 222-251.
- [40] V. Medri, A. Ruffini, The influence of process parameters on in situ inorganic foaming of alkali-bonded SiC based foams, *Ceram. Int.* 38 (2012) 3351–3359.
- [41] E. Prud'homme, P. Michaud, E. Joussein, C. Peyratout, A. Smith, S. Rossignol, In situ inorganic foams prepared from various clays at low temperature, *Appl. Clay Sci.* 51 (2011) 15–22.
- [42] H. Xu, J. S. J. Van Deventer, The geopolymerization of alumino-silicate minerals, *J. Miner. Proc.* 59 (2000) 247.
- [43] E. Prud'homme, P. Michaud, E. Joussein, J.M. Clacens, S. Rossignol, Role of alkaline cations and water content on geomaterial foams: monitoring during formation, *J. Non-Cryst. Solids* 357 (2011) 1270–1278.
- [44] A. Fernández-Jiménez, A. Palomo, Mid-infrared spectroscopic studies of alkali-activated fly ash structure, *Micropor. Mesopor. Mat.* 86 (2005) 207-214.
- [45] J. Davidovits, Geopolymer Chemistry and Applications. Institut Géopolymère, Saint-Quentin (F), (2008).
- [46] A. Gharzouni, E. Joussein, B. Samet, S. Baklouti, S. Pronier, I. Sobrados, J. Sanz, S. Rossignol, The effect of an activation solution with siliceous species on the chemical reactivity and mechanical properties of geopolymers, *J. Sol-Gel Sci. Technol.* 73 (2015) 250-259.
- [47] A. Gharzouni, E. Joussein, B. Samet, S. Baklouti, S. Rossignol, Effect of the reactivity of alkaline solution and metakaolin on geopolymer formation, *J. Non-Cryst. Solids* 410 (2015) 127-134.
- [48] M.R. North, T.W. Swaddle, Kinetics of silicate exchange in alkaline aluminosilicate solutions, *Inorg. Cem.* 39 (2000) 2661-2665.

- [49] K.B. Langille, D. Nguyen, J.O. Bernt, D.E. Veinot, M.K. Murthy, Mechanism of dehydration and intumescence of soluble silicates. Part II: Effect of the cation, *J. Mater. Sci.* 26 (1991) 704-710.
- [50] E. Prud'homme, P. Michaud, E. Joussein, C. Peyratout, A. Smith, S. Arrii-Clacens, J.M. Clacens, S. Rossignol, Silica fume as porogent agent in geomaterials at low temperature, *J. Eur. Ceram. Soc.* 30 (2010) 1641–1648.
- [51] E. Kamseu, Z. N. M. NGoulore, B. Nait Ali, S. Zekeng, U. C. Melo, S. Rossignol, C. Leonelli, Cumulative pore volume, pore size distribution and phases percolation in porous inorganic polymer composites: Relation microstructure and effective thermal conductivity, *Ener. Build.* 88 (2015) 45-56.
- [52] R. Siddique, M. I. Khan, *Supplementary Cementing Materials*, Springer-Verlag Berlin Heidelberg (D), (2011) , 67-119.
- [53] S. Delair, E. Prud'homme, C. Peyratout, A. Smith, P. Michaud, L. Eloy, E. Joussein, S. Rossignol, Durability of inorganic foam in solution: the role of alkali elements in the geopolymer network, *Corros. Sci.* 59 (2012) 213-221.
- [54] V. Medri, E. Papa, E. Landi, Behaviour of alkali bonded silicon carbide foams in modified synthetic body fluid, *Mater. Lett.* 106 (2013) 377–380.

## 7. Conclusions

Geopolymers are a versatile type of synthetic porous inorganic material with a broad range of potential applications. The porosity of the geopolymers may be thought as a secondary functional phase, that has to be designed and exploited for optimizing the performance of the material. Therefore, the main theme of this Thesis was to provide preparation techniques to generate geopolymers with hierarchical porosity, characterized by different dimension, shape and distribution of the pores.

The control of the porosity is the most important factor to endow materials with brand-new and useful properties, able to functionalize the materials. Therefore, the research activity was addressed to the exploitation of the skeletal mesoporosity of the geopolymers combined with the macroporosity induced by different methods, to create pore-interconnected 3-dimensional structures, in which mesopores are directly linked with macropores.

The production process in aqueous medium allowed to tailor the porosity in a wide dimensional range. Porosity under 1  $\mu\text{m}$  was highly affected by the water content in the starting mixture, since water acts as pore former during the polycondensation stage. Porosity from 1 to 100  $\mu\text{m}$  was in part affected by the water and in part by the applied production process. The porosity over 100  $\mu\text{m}$ , especially the shape, dimension and distribution of the pores, were extremely affected by the method to produce the ultra-macroporous geopolymers.

Geopolymer slurries resulted suitable for the application of process techniques commonly applied in the production of porous ceramics, such as ice-templating and direct foaming techniques, as well as for the addition of fillers easily bound by the matrices. The formulation of the geopolymer starting compositions and the process optimization of the different techniques allowed to obtain promising materials, useful in different fields depending on the achieved properties. All the materials produced in the course of this research were deeply investigated to evaluate the final properties, many of which arising from the generated intrinsic or induced porosity.

The following conclusions can be drawn from each research activity reported in the chapters of the Thesis. There were also several issues arising from the studies

which need further investigation, therefore, some recommendations for future work are also proposed.

In chapter 4 unidirectional lamellar geopolymers were synthesized by ice-templating, obtaining highly porous materials. The technique was successfully applied for the first time to a geopolymer water-based reactive sol-gel system. The process optimization allowed the simultaneous formation of the geopolymer intrinsic mesoporosity and a lamellar macroporosity by unidirectional ice growth. The characterization of the samples evidenced as the ice-templating may be combined with the geopolymerization synthesis, that is triggered by a maturation step before the addition of the water required for the ice-templating process. It was found that the macrostructure (lamellar pores morphology) was strongly affected by several process parameters: the mould geometry, the amount of water targeted for ice-templating and the viscosity of the starting slurry, affected by the maturation treatment applied. In general, the lamellar macroporosity increased by increasing the water amount used for the ice-templating; viscous mixtures led to the formation of randomly oriented short lamellae and small lamellar pore width, while thicker, longer and more spaced lamellae were obtained when the viscosity of the slurry decreased. Monoliths with a total porosity of  $\approx 70\%$ , density of  $\approx 0.8 \text{ g}\cdot\text{cm}^{-3}$  and pores comprised in a wide dimensional range between 5 nm and 3 mm were obtained.

The final scale-up of the overall process highlighted that this technique can be adopted for the realization of big samples, with different geometries and an oriented lamellar macroporosity on long-range order, giving rise to promising materials usable in catalysis and filtration fields.

However, recommendations for a future work include a deeper study of the starting geopolymer slurries, especially to efficiently tune the viscosity and generate pore distributions characterized by different lamellar pore length and width. Preliminary studies revealed the possibility to obtain samples with large dimensions, although the reproducibility of the samples and the lamellar macroporosity must be assessed, as well as mechanical tests have to be performed.

In chapter 5 the porosity of geopolymers was designed to produce a prototype of a

loop heat pipe (LHP) evaporator. Conventional metallic or plastic wicks were substituted by innovative geopolymer wicks in a concentric configuration. In the outer part of the wicks configuration, a submicrometric porosity, required to exert a high capillary pressure for the fluid recirculation around the loop, was achieved using a geopolymer resin with fused silica added. A more porous wick, essential to operate the working fluid, was obtained using the direct foaming of the geopolymer matrix through the use of  $\text{Si}^0$  as blowing agent. The assembly of the final prototype was obtained by means of a combination of near net shaping and *in situ* casting techniques, with consequent lowering of the production costs of the evaporator part. The preliminary tests evidenced good thermal exchange performances, highlighting that geopolymers may be a promising technology for heat pipes. However, the overall production process of the geopolymer wicks needed to be improved to obtain porosities in a more restricted dimensional range, able to endow the device with improved properties. Starting compositions of the resins may be formulated by the addition of different thermally stable fillers, able to change the Si/Al molar ratio that affected the development of the intrinsic and fine porosity of the material. Furthermore, the production process must be improved to avoid the entrapment of air bubbles during the casting, causing the generation of randomly distributed big pores.

Chapter 6 reports the use of different fillers to achieve materials characterized by high porosity, reduced density and good thermal-insulating properties.

The density of the materials was decreased by the addition of exfoliated vermiculite or silica fume, to generate lightweight geopolymer foams, thanks to the presence of free  $\text{Si}^0$  impurities, that in the alkaline medium generated  $\text{H}_2$ , with consequent blowing of the slurry.

Suitable mixtures for the production of the composite materials were formulated; the use of the vermiculite improved the heat-insulating properties of the starting geopolymer matrices, that resulted comparable with other lightweight or cellular materials. Big panels with dimension  $55 \times 47 \times 3 \text{ cm}^3$  were produced after a scale up approach. The panels showed a low bulk density of  $\approx 0.8 \text{ g}\cdot\text{cm}^{-3}$ , a total porosity of  $\approx 66 \text{ vol.}\%$ , thermal resistance up to  $800 \text{ }^\circ\text{C}$  and good mechanical properties. The combination of the good thermal and mechanical properties,

suggested that the panels may be used as pre-cast high-temperature insulating panels, suitable to be mechanically anchored to load-bearing structures.

The composite foams showed lower density,  $\approx 0.5 \text{ g}\cdot\text{cm}^{-3}$ , and a higher total porosity of  $\approx 80 \%$ , with pore dimensions comprised from  $0.01 \text{ }\mu\text{m}$  to  $3100 \text{ }\mu\text{m}$ . Both the composite materials showed good thermal conductivity values, equal to  $\approx 0.2 \text{ W m}^{-1} \text{ K}^{-1}$ , confirming a possible utilization in the heat-insulating field. However, further characterization and process optimization are required. Detailed feasibility analysis has to be performed to find the most suitable industrial processes, time and cost-effective, as a function of the final product and intended use.